A STUDY ON THE ADSORPTION PROPERTIES OF MULTIWALLED CARBON NANOTUBES AND THEIR RELATIONSHIP TO APPLICATIONS AS VOLATILE ORGANIC COMPOUNDS SENSORS

NURUL ROZULLYAH BTE ZULKEPELY

THESIS SUBMITTED IN FULFILMENT OF THE REQUIREMENTS FOR THE DEGREE OF DOCTOR OF PHILOSOPHY

DEPARMENT OF PHYSICS
FACULTY OF SCIENCE
UNIVERSITY OF MALAYA
KUALA LUMPUR

2018

UNIVERSITY OF MALAYA
ORIGINAL LITERARY WORK DECLARATION

Name of Candidate: **Nurul Rozullyah Binti Zulkepely**

Matric No: **SHC120068**

Name of Degree: **Doctor of Philosophy**

Title of Project Paper/Research Report/Dissertation/Thesis ("this Work"):

A STUDY ON THE ADSORPTION PROPERTIES OF MULTIWALLED CARBON NANOTUBES AND THEIR RELATIONSHIP TO APPLICATIONS AS VOLATILE ORGANIC COMPOUNDS SENSORS.

Field of Study: **Experimental Physics**

I do solemnly and sincerely declare that:

(1) I am the sole author/writer of this Work;
(2) This Work is original;
(3) Any use of any work in which copyright exists was done by way of fair dealing and for permitted purposes and any excerpt or extract from, or reference to or reproduction of any copyright work has been disclosed expressly and sufficiently and the title of the Work and its authorship have been acknowledged in this Work;
(4) I do not have any actual knowledge nor do I ought reasonably to know that the making of this work constitutes an infringement of any copyright work;
(5) I hereby assign all and every rights in the copyright to this Work to the University of Malaya ("UM"), who henceforth shall be owner of the copyright in this Work and that any reproduction or use in any form or by any means whatsoever is prohibited without the written consent of UM having been first had and obtained;
(6) I am fully aware that if in the course of making this Work I have infringed any copyright whether intentionally or otherwise, I may be subject to legal action or any other action as may be determined by UM.

Candidate's Signature Date:

Subscribed and solemnly declared before,

Witness's Signature Date:

Name:

Designation:

A STUDY ON THE ADSORPTION PROPERTIES OF MULTIWALLED CARBON NANOTUBES AND THEIR RELATIONSHIP TO APPLICATIONS AS VOLATILE ORGANIC COMPOUNDS SENSORS

ABSTRACT

In this thesis, a study on the diameter effect of the adsorption properties of Rhodamine 6G on multiwalled carbon nanotubes is presented. Multiwalled carbon nanotubes with diameters between 8 to 50 nm were used. Rhodamine 6G adsorption properties were measured based on the time variation of concentration reduction and were fitted to the Langmuir, Freundlich and Temkin adsorption models. The values of maximum adsorption capacity obtained from Langmuir isotherm equation at 300 K were 222 mg/g for ~8 nm and 49.3 mg/g for ~50 nm MWCNTs. Based on the Freundlich model, the constant for adsorption capacity for Rhodamine 6G were 146.59 mg/g and 19.70 mg/g for MWCNTs for diameter ~8 and ~50 nm, respectively. The difference indicated strong interaction of the dye molecules with the smaller diameter MWCNTs. Also, based on all the models, it can be concluded the smallest diameter was the better adsorbent compared to the large diameter MWCNTs for the adsorption of R6G since it was related with the high specific surface area. Kinetic analysis of the time variation of the R6G concentration towards different amounts of MWCNTs were modeled to the pseudo first and the second order equations and shown that the adsorption kinetic was more accurately represented by a pseudo second-order model with regression value of pseudo second-order > first-order model. For vapor sensor, pure MWCNTs (diameters = ~8, 20-30 and ~50 nm) together with ZnO decorated with MWCNTs (diameter = ~50 nm) was used as sensor fabricated on printing paper for ethanol and toluene vapor sensing. The resistance of the MWCNTs samples on printing paper were 2.06, 0.49 and 0.30 kΩ for MWCNTs for diameters ~8, 20-30 and ~50 nm respectively. The sensing response measured by exposing the samples to toluene vapor at concentrations of between 425 and 4253 ppm yielded sensitivities of 12.73×10^{-5}, 7.69×10^{-5} and 2.65×10^{-5} ppm^{-1} while for ethanol vapor at concentrations of between 780 and 7804 ppm were 9.88×10^{-5}, 4.39×10^{-5}, and 2.88×10^{-5} ppm^{-1} for MWCNTs for diameters ~8, 20-30 and ~50 nm respectively. High sensitivity for low diameters can be due to higher effective specific surface area afforded higher conductivity by the MWCNTs with smaller diameter.

Keywords: Adsorption, Carbon Nanotubes, Rhodamine 6G, Volatile Organic Compounds Sensors.

KAJIAN MENGENAI SIFAT PENYERAPAN NANOTIUB KARBON MULTIDINDING DAN HUBUNGAN MEREKA UNTUK KEGUNAAN SEBAGAI SENSOR KOMPONEN ORGANIK MERUAP

ABSTRAK

Dalam tesis ini, kajian mengenai kesan diameter terhadap ciri-ciri penyerapan rodamina 6G pada nanotiub karbon multidinding dilaporkan. Nanotiub karbon multidinding dengan diameter antara 8-50 nm digunakan. Ciri-ciri penyerapan rodamina 6G diukur berdasarkan variasi masa terhadap pengurangan kepekatan dan telah disuaikan pada Langmuir, Freundlich dan Temkin model penyerapan. Nilai kapasiti penyerapan maksimum yang diperoleh dari Langmuir persamaan isoterma pada 300 K adalah 222 mg/g untuk ~8 nm dan 49.3 mg/g untuk ~50 MWCNTs nm. Dari model Freundlich, pemalar untuk kapasiti penyerapan adalah dalam kadar 146.59 mg/g dan 19.70 mg/g bagi ~8 nm dan ~50 nm, masing-masing. Nilai pemalar yang tinggi untuk haba penyerapan daripada ~8 nm berbanding dengan ~50 nm menunjukkan interaksi kuat antara MWCNTs dengan diameter kecil berbanding diameter besar terhadap rodamina 6G. Dari semua model, dapat disimpulkan diameter yang paling kecil adalah penyerap lebih baik berbanding diameter besar untuk penyerapan rodamina 6G kerana ia berkaitan dengan luas permukaan tertentu yang tinggi. Analisis kinetic terhadap variasi masa dan kepekatan rodamina 6G bagi jumlah MWCNTs yang berbeza dimodelkan kepada persamaan pseudo pertama dan peringkat kedua dan menunjukkan bahawa kinetik penyerapan diwakili lebih tepat oleh model pseudo kedua dengan regresi pseudo peringkat kedua > model peringkat pertama. Untuk sensor wap, MWCNTs tulen (diameter = ~8, 20-30 dan ~50 nm) juga dengan MWCNTs (diameter = ~50 nm) bertatahkan dengan ZnO akan digunakan sebagai sensor dihasilkan di atas kertas percetakan untuk etanol dan toluene wap pengesan. Rintangan daripada MWCNTs sampel di atas kertas percetakan adalah 2.06, 0.49 dan 0.30 kΩ untuk MWCNTs bagi diameter ~8, 20-30 dan ~50 nm masing-masing. Tindak balas pengesan diukur dengan mendedahkan sampel kepada wap toluena pada kepekatan antara 425 dan 4253 ppm menghasilkan sensitiviti 12.73×10^{-5}, 7.69×10^{-5} and 2.65×10^{-5} ppm^{-1} manakala bagi wap etanol pada kepekatan antara 780 dan 7804 ppm adalah 9.88×10^{-5}, 4.39×10^{-5}, dan 2.88×10^{-5} ppm^{-1} untuk MWCNTs bagi diameter ~8, 20-30 dan ~50 nm masing-masing. Kepekaan yang tinggi bagi diameter rendah boleh disebabkan oleh keberkesanan luas permukaan tertentu yang lebih tinggi yang memberikan kekonduksian tinggi oleh MWCNTs dengan diameter lebih kecil.

Kata kunci: Penyerapan, Karbon Nanotiub, Rodamina 6G, Sensor Komponen Organik Meruap.

ACKNOWLEDGEMENTS

I express gratitude and appreciation to Prof. Dr. Roslan Md. Nor and Dr. Azzuliani Supangat for their invaluable supervision.

I gratefully acknowledge the funding received towards my PhD from the Ministry of Higher Education under MyBrain15 program and University Malaya for Postgraduate Research Fund (PPP).

Special thanks to my friends and lab mates for their encouragement. Thank you for your love, moral support and encouragement throughout this work to my big family which are Ayah (Zulkepely Saleh), Mak (Robiah Embot), Abah (Sariman Shariff), Mak (Jamilah), Along (Zaffarodyn), Alang (Najua), Adik (Wahida), Kak Nan, Abang Bob, Kak Huda, Abang Nazri, Izzat and Fatin.

Last but not least, thank you to my beloved husband, Muhammad Ehsan Bin Sariman and my son, Nazrin Muizzuddin Bin Muhammad Ehsan for their understanding, love and moral support.

TABLE OF CONTENTS

LIST OF FIGURES

LIST OF TABLES

LIST OF ABBREVIATIONS

BET	:	Brunauer-Emmett-Teller
CVD	:	Chemical vapor deposition
CNTs	:	Carbon nanotubes
DTA	:	Derivative thermal analysis
EDX	:	Energy dispersive x-ray
FESEM	:	Field emission scanning electron microscopy
HRTEM	:	High resolution transmission electron microscopy
MWCNTs	:	Multiwalled carbon nanotubes
NPs	:	Nanoparticles
R6G	:	Rhodamine 6G
SDS	:	Sodium dodecyl sulphate
SMU	:	Source measuring unit
TGA	:	Thermogravimetric Analysis
VOC	:	Volatile organic compounds
XRD	:	X-ray diffraction

LIST OF APENDICES

CHAPTER 1: INTRODUCTION

1.1 Overview

Adsorption is a surface process that occurs at the interface of two phases where microscopic species from one phase adheres to the surface of the other. The microscopic species can be atoms, molecules, radicals or even clusters. The adsorbed species are known as adsorbates which adhered to surfaces of the absorbent. Generally, adsorption can occur by physical or chemical forces. Physical adsorption, known as physisorption occurred due to the van der Waal attraction between the adsorbates and the absorbent surface. The binding energy is normally weak, in the range of thermal energy. In adsorption due to chemical process known as chemisorption the binding energy can be high, in the range of a few eVs. Here, electronic bonding occurred between the adsorbates and the surface of the adsorbent. Chemisorption is common with metallic adsorbate surfaces. The chemical reaction can be visualized in simple terms as the bonding between adsorbate valence electrons with the free electrons in the metal. As such, it is not a purely chemical bond in the sense of ionic or covalent bonding. A related process known as absorption involves the penetration into the pores of absorbates which is a macroscopic process. Under many situations, both adsorption and absorption may occur for a particular system. The general term to describe the process is sorption, which covers both the microscopic and macroscopic processes (Dąbrowski, 2001).

In the generalized form, adsorption has been described based on the time evolution of the process. These kinetic evaluation average out the reversible processes of adsorption and desorption that may have occurred. The significant of the kinetic models are that they can be directly verified experimentally.

For industrial applications porous adsorbents are desirable due to the significant increase in surface area afforded by the pores. Owing to its superior properties such as large specific surface area, highly porous and hollow structure and highly reactive surface carbon nanotubes (CNTs) are excellent candidate as adsorbents. A variety of adsorption applications used CNTs as adsorbent has been reported. These including application in gas molecules adsorbents, removal of different pollutants such as metallic ions (Li et al., 2002; Moghaddam & Pakizeh, 2015), synthesized dyes (Gupta et al., 2013; Wang et al., 2012) and hazardous organic compounds (Shao et al., 2011).

As adsorbent in sensor materials, CNTs have exhibited good stability in terms of chemical and mechanical properties (Saito et al., 1998). A number of researchers have utilized CNTs in fabricating a variety of sensors like biosensors (Balasubramanian & Burghard, 2006; Yang et al., 2015), electrochemical sensors (Hu & Hu, 2009; Yáñez-Sedeño et al., 2010) and gas sensors (Cantalini et al., 2003; Rajaputra et al., 2008). The selection of sensor based of the CNTs was due to their lower functioning temperatures compared to existing semiconducting oxide sensor which required operational temperatures in the range of 300 to 600^{o}C to boost up the reaction and gained sensible sensitivity. Semiconducting oxide sensors normally have high resistance and this makes the sensing integration more complex and pricey (Kohl, 2001). CNTs used as gas sensor for NO_2 and NH_3 have been reported (Kong et al., 2000). The authors reported that the conductance value of SWCNTs increased when exposed to NO_2 but decreased when exposed with NH_3. This demonstrates the idea of CNTs application as chemical sensors. Specific sensing methods that has been reported which are based on the change of resistance (Terranova et al., 2007), capacitance (Chen et al., 2009) and ionization potential (Modi et al., 2003). These have been used to study gas sensing properties of CNTs.

1.2 Objective of this work

The main objectives of this study are to investigate the adsorption behavior of MWCNTs. Adsorption capacity of MWCNTs was studied under two differ parameters which are effect of MWCNTs diameter and effect of MWCNTs amounts on the adsorption behavior towards R6G molecules in aqueous solution. Experimental adsorption behavior was fitted to three well known models, namely the Langmuir, Freundlich and Temkin models. The kinetic adsorption behavior was estimated by using the pseudo-first-order, pseudo-second order kinetic equations and the intraparticle diffusion model. The understanding of the adsorption behavior of the MWCNTS was then applied in the relationship between MWCNTS sensors and volatile organic compound (VOC).

In summary, the objectives of the study are as follows;

(i) To investigate the effect of MWCNTs diameter on adsorption behavior towards R6G molecules in aqueous solution.

(ii) To investigate the sensing properties of MWCNTs toward volatile organic compound (VOC) at room temperature.

(iii) To investigate the relationship of between adsorption properties and applications as volatile organic compound (VOC) sensor of MWCNTs.

1.3 Thesis overview

Chapter 2 of this thesis will give an overview of CNTs in terms of its discovery, structure of CNTs, and properties of CNTs which including electrical, optical, mechanical and thermal. In this chapter a brief discussion on ZnO nanoparticles and

ZnO decorated CNTs synthesis is presented. The applications of CNTs which were adsorbent and chemical sensors is examined in this chapter.

Chapter 3 presents the adsorption properties of R6G on MWCNTs. In this chapter, two parameters were analyses. One was the effect of different diameters of MWCNTs and another one was the effect of different amount of MWCNTs. The results will be discussed in terms of adsorption equilibrium and kinetic behaviour.

Chapter 4 focused on the studies of pure and ZnO decorated MWCNTs as VOC sensor. The VOC that have been used were ethanol and toluene. The results included several characterization of the sensor materials used to elucidate the morphological, thermal and electrical properties. The sensor response will also be discussed in terms of adsorption models as used in Chapter 3.

Chapter 5 concludes the overall study in this work. To enhance this work, several suggestions for further work are also included.

CHAPTER 2: LITERATURE REVIEW ON MWCNTS AS VOC SENSOR AND ADSORBENT FOR DYE IN AQUEOUS SOLUTION

2.1 Introduction

In this chapter a brief overall review of carbon nanotubes (CNTs) is presented. It covers the structure of CNTs, the history of CNTs discovery, general CNTs properties including electrical, optical, mechanical and thermal properties. Different techniques to enhance the dispersion of CNTs are also discussed. In order to improve properties of CNTs especially in applications as vapor sensor, metal oxide specifically zinc oxide (ZnO) decoration is discussed. ZnO nanoparticles structures are briefly presented in the next section followed with the decoration of ZnO on multiwalled carbon nanotubes (MWCNTs). The next section is devoted to the applications of CNTs as adsorbent materials together with the adsorption equilibrium model and kinetic adsorption models in explaining the adsorption mechanism. The literature review section ends by describing some applications of CNTs as chemical sensors.

2.2 Carbon nanotubes

2.2.1 The Structure of CNTs

CNTs consist of one atom thick layers of graphite known as the graphene sheet. The graphene sheet will be scrolled up into smooth and continuous cylinder form with the diameter in the range of nanometers (Dresselhaus et al., 2004). Basically there are two types of CNTs namely single-walled CNTs (SWCNTs) and multi-walled CNTs (MWCNTs) as shown in Figure 2.1. Another form of MWCNTs is the double-walled CNTs (DWCNTs) (Aqel et al., 2012). SWCNTs consist only one graphene sheet, while DWCNTs consist two layers of graphene sheets and MWCNTs have many layers of graphene sheets.

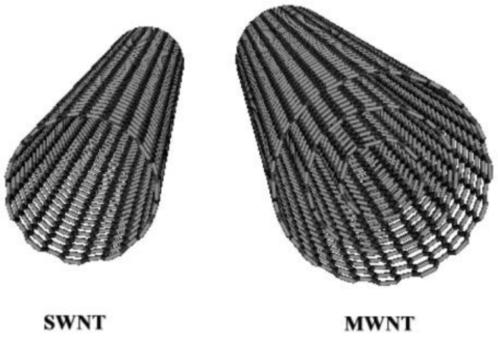

Figure 2.1: Structure of SWCNTs (left) and MWCNTs (right).

There are several ways to roll up the sheet and the ways will be determined the pattern of the CNTs. This pattern will affect some properties of the CNTs such as electrical properties and the position of hexagonal bonding with corresponding nanotube axis.

The CNTs with specific geometry can be described by a combination of integers *n* and *m* which known as chiral vector, $\boldsymbol{C_h}$ such that;

$$\boldsymbol{C_h} = n\boldsymbol{a}_1 + m\boldsymbol{a}_2 \tag{2.1}$$

where $\boldsymbol{a_1}$ and $\boldsymbol{a_2}$ are the two units vectors of the carbon sheet. The chiral vector goes along the edge of the fabricated CNTs (Marinković, 2008). The opening point (tail) and the ending point (tip) of the chiral vector are superimposed at which the carbon lattice are rolled.

There are three well defined patterns for nanotube structure which are arm-chair nanotube ($n = m$), zigzag nanotube ($n = 0$ or $m = 0$) or chiral nanotube (any other *n* and *m*) as listed in Figure 2.2, Figure 2.3 and Figure 2.4, respectively (Aqel et al., 2012). It is known as arm-chair when the graphene sheet is rolled along the x-axis. The arm-chair line moves along continuous hexagon thus dividing them into two even portions. The nanotube shape is similar to the upholstered chair with side support for the arm. The vector **OA** is the chiral vector (x-axis) and the vector **OB** is the translation vector represented as **T**. The $\boldsymbol{a_1}$ and $\boldsymbol{a_2}$ vectors are the unit vectors and x and y is the Cartesian coordinates. The graphene sheet pattern is called as zigzag nanotube when it is rolled along the y-axis. Shown in Figure 2.5 are the chiral nanotube generated from other chiral vector orientations of rolling graphene sheet.

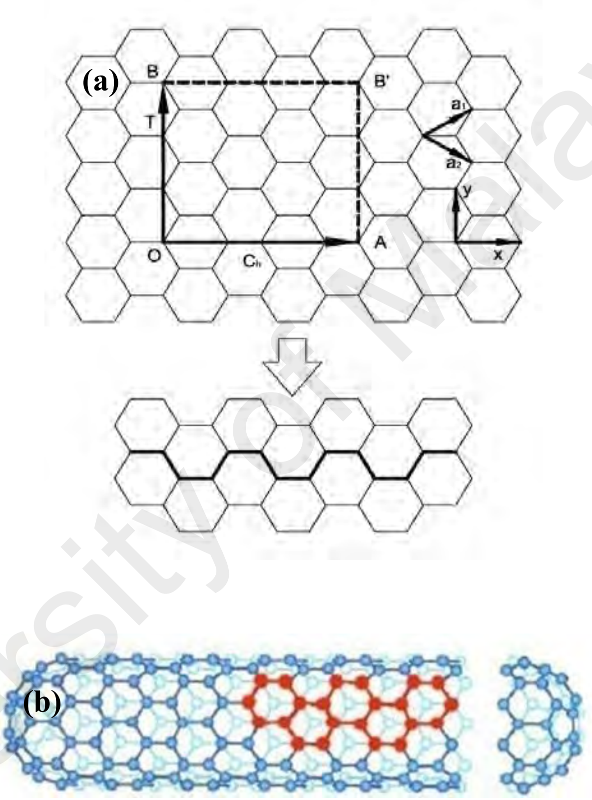

Figure 2.2: (a) Graphene sheet rolled up in the armchair formed. (b) Armchair carbon nanotube (*n*,*m*) = (5,5) (Dresselhaus et al., 1996).

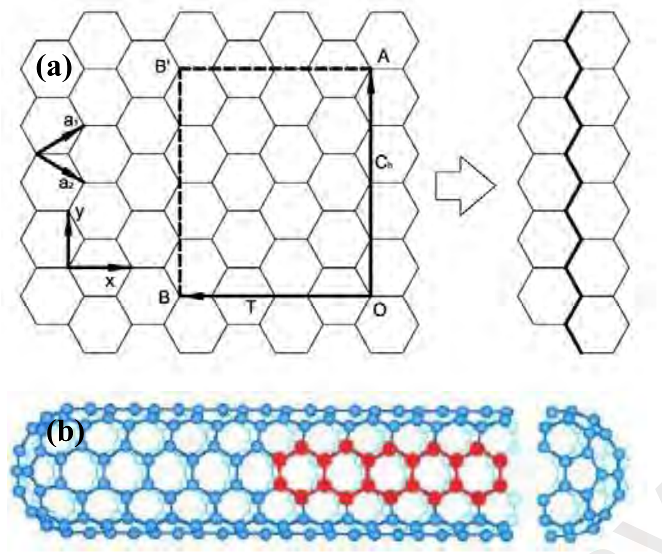

Figure 2.3: (a) Graphene sheet rolled up in the zigzag formed. (b) Zigzag (*n*,*m*) = (9,0) (Dresselhaus et al., 1996).

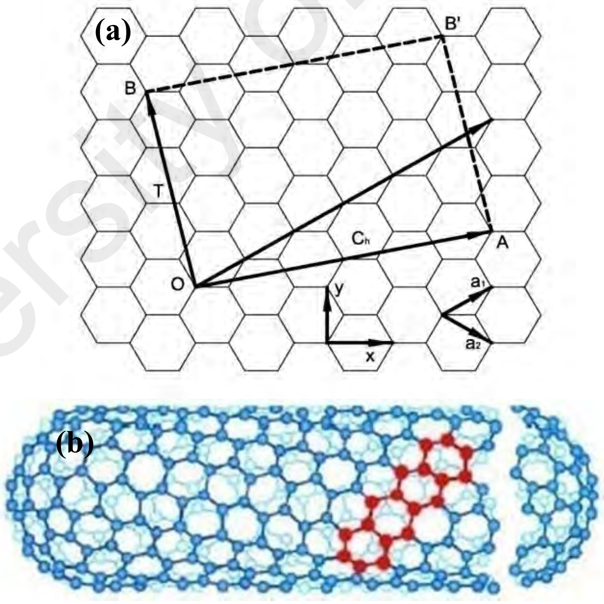

Figure 2.4: (a) Graphene sheet rolled up as chiral nanotube. (b) Chiral (*n*,*m*) = (10,5) (Dresselhaus et al., 1996).

CNTs can exhibit two different electrical responses which are metallic or semiconducting depending on its geometrical structure (Figure 2.5) (Dresselhaus et al., 1996). The nanotube is metallic if (*n*-*m*) is divisible by 3 while become semiconducting when (*n*-*m*) is not divisible by 3. The CNTs can act as semimetal or zero bandgap semiconductors which means that it exhibit metallic properties at some direction and change to semiconducting properties at other direction. It was reported the band gap, E_g was inversely proportional with nanotube diameter ($E_g \approx 0.84$ eV/d) (Baughman et al., 2002). SWCNTs have a diameter in the range of 1-2 nm and the lengths from a micrometres to several millimetres (Aqel et al., 2012).

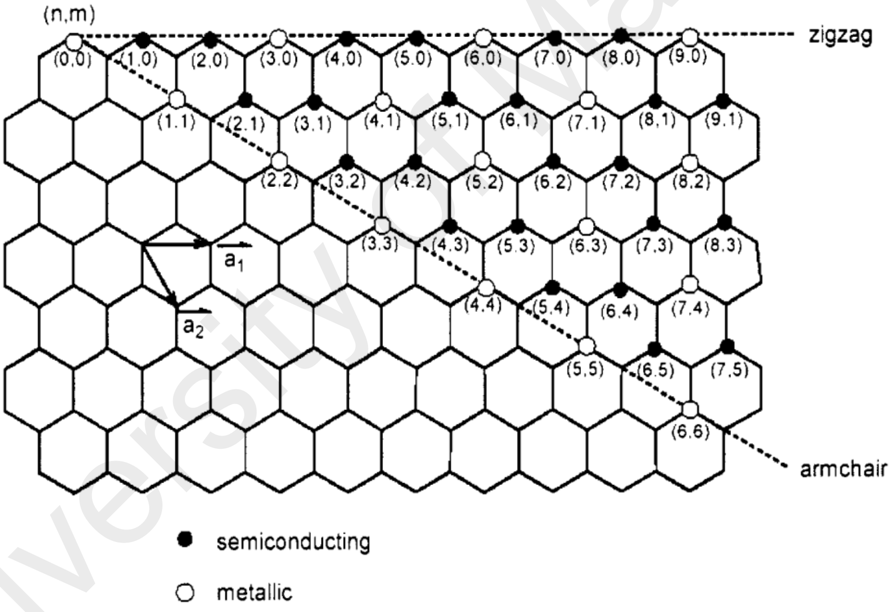

Figure 2.5: The CNTs specified using (*n*, *m*) notation. The solid dots represent semiconducting nanotubes and the hollow dots represent metallic nanotube. Zigzag and armchair direction are shown by dotted line (Charlier & Issi, 1998).

2.2.2 History of CNTs

Carbon in the form of graphite and diamond were discovered in 1779 and 1789, respectively. Later it was found that they belonged to the same family of a chemical element. It took about 200 years for a new discovery of carbon in 1985 when a new molecule purely made from carbon was discovered by Kroto and his co-workers (Kroto et al., 1985). This molecule was known as fullerene and consists of 60 carbon atoms that are bonded in pentagons and hexagons structures and was named as the C_{60}.

However, CNTs were believed to be found as early as 1952 by Radushkevich and Lukyanovich (Monthioux & Kuznetsov, 2006) and later by Roger Bacon in the 1960 where he discovered a strange new carbon filament with straight and hollow tubes with diameter <100 nm (Bacon, 1960). In 1972, Baker and his co-researchers successfully fabricated small carbon filament with a diameter of 15 nm by using metal as catalyst (Baker et al., 1972).

MWCNTs was discovered accidentally by a group of researchers led by Sumio Iijima (Iijima, 1991). They found by using TEM imaging, a material with needle-shaped pattern which was deposited on the carbon cathode of an arc discharge while conducting a study on fullerenes (Kroto et al., 1985). This material was later named carbon nanotubes by Iijima. The first figures from the discovery are shown in Figure 2.6(a)-(c) (Iijima, 1991).

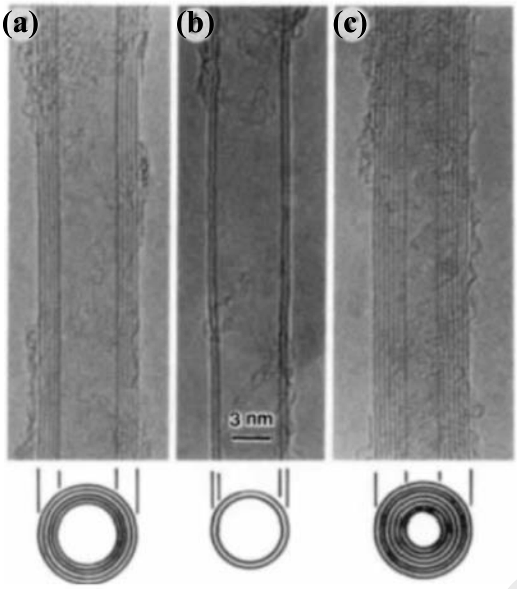

Figure 2.6: (a)-(c) Figures of CNTs found by Iijima in 1991 through transmission electron microscope (TEM) (Iijima, 1991).

SWCNTs was independently reported in 1993 with the same arc-discharge technique by Bethune with his group (Bethune et al., 1993) and Iijima with Ichihashi (Iijima & Ichihashi, 1993).

2.2.3 CNTs properties

The CNTs have gained great interest by many researchers as promising materials both in basic science and novel applications due to their excellent properties. This section will discuss the electrical, optical, mechanical and thermal properties of CNTs.

2.2.3.1 Electrical properties

The diameter and chirality of SWCNTs are the determination factors for the conductivity for the CNTs. For CNTs, it can be either metallic or semiconducting. It was reported that metallic CNTs can transfer up to 25 μA of current with high current density of 10^9 A/cm^2 (Peng et al., 2014) while the maximum current density for copper is only 10^5 A/cm^2 (Hong & Myung, 2007).

The covalent bonded structure of CNTs prevented such breakdown in CNTs wires and due to ballistic transport, the intrinsic resistance of CNTs is almost zero. The failure condition of CNTs under great current is different from metallic wire conductors. In CNTs, the current is carried by the outermost tube layer whereas in metallic wires charge travelling throughout the cross-section. (Guldi & Martín, 2010). Therefore in MWCNTs, if the current capacity is achieved, only the outer wall of the tube is expected to fail and then the current is carried by a new exposed tube layer (Avouris, 2002; Collins et al., 2001). On the other hand for regular wire whenever the current carrying capacity is reached a complete failure causes the wire to break.

Bending of CNTs can also affect the electrical properties, for example at twisting angle greater than 45°, kink will form at the tube wall and the tube resistance increases (Rochefort et al., 1999). The conductivity in MWCNTs is more complex than SWCNTs as each of the multiple rolled layers in MWCNTs can have different electrical properties. Doping and annealing have been shown to change the electrical properties of CNTs. Terrones et al. demonstrated that CNTs doped with nitrogen or boron exhibited novel electronic properties which is not seen in pure CNTs structure (Terrones et al., 2004). The incorporation of other element, for example less than 0.5 % of dopant would enhance the electrical conductance but the mechanical properties were not affected at all. This is due to the presence of donor for nitrogen-doped and holes for boron-doped CNTs, the CNTs surface then become reactive. This reactivity is useful in applications as electron emission sources, sensor and nanoelectronics applications. Annealing CNTs at 200°C for 10 hours in vacuum will change the semiconducting

CNTs to n-type (as-prepared semiconducting CNTs tend to demonstrate p-type behaviour) (Guldi & Martín, 2010).

2.2.3.2 Optical properties

Several characterization have been done in order to examine the optical properties of CNTs such as reflective measurement (Bommeli et al., 1996), optical ellipsometry (De Heer et al., 1995) and electron energy loss spectroscopy (Kuzuo et al., 1992). It was reported by Yang et al. in 2008 that CNTs is the darkest material known when they discovered the reflectance of nanotube was ~0.045 % (Yang et al., 2008). It was believed that this is due to random scattering which occur on rough tube's surface (Guldi & Martín, 2010).

It was found from Raman spectroscopy that different radial breathing mode (RBM), G and D peaks can change relying on the polarization angle and nanotube axis (Murakami et al., 2005; Rao et al., 2000). The degree of alignment of nanotubes can also be determined from optical adsorbance due to the dependency of tube adsorption on its axis orientation towards incident light polarization (Murakami et al., 2005). The value for adsorption coefficient for armchair and zig zag nanotubes was found to be different especially for lower energy area. This corresponds to the peak that attributed to between π bands (Huaxiang et al., 1994).

2.2.3.3 Mechanical properties

The covalent bond between the carbon-carbon in CNTs resulted in excellent mechanical properties. In terms of tensile strength and elastic modulus, CNTs are the strongest and stiffest material compared to other materials such as steels and aluminium

(Fischer, 2006; Guldi & Martín, 2010). The individual SWCNTs give an excellent bending behaviour without breaking or suffering big transverse deformation (Falvo et al., 1997; Yakobson, 1998) and CNTs returned to their original form once the force is removed.

CNTs are also light weight with density of 1300-1400 kg/m^3 compared to diamond which has comparable mechanical properties (Collins & Avouris, 2000; Guldi & Martín, 2010). Because of this, many future applications such as automotive manufacturing where CNTs can be used in composite for lighter and stronger body parts for better fuel utilization in automobiles. The specific strength for CNTs at 48 000 kNmkg^{-1} is higher than carbon steel which is about 154 kNmkg^{-1} (Fischer, 2006).

The mechanical properties of CNTs depend on the tube diameter and from simulation and experimental analysis showed that the reducing of tube diameter enhanced the elastic modulus value. In 2006, Huang and co-workers studied that SWCNTs at room temperature and 2000 °C have maximum tensile strain of 5-15 % and 280 %, respectively before mechanical failure (Huang et al., 2006).

CNTs will buckle under compression and bending pressure. This is caused by the high aspect ratio and its hollow structure (Jensen et al., 2007). Popov et al. have found that the SWCNTs was able to hold a pressure of up to 24 GPa without any change in shape and structure (Popov et al., 2002). They also evaluated that the bulk modulus of 462-546 GPa which were higher than that for diamond (420 GPa).

2.2.3.4 Thermal properties

From simulation methods, it has been estimated that thermal conductivity of CNTs ranged from 1000-6600 Wm^{-1}K^{-1} and are higher than that of graphite or diamond

(Berber et al., 2000; Osman & Srivastava, 2001). From experiments thermal conductivity of SWCNTs at room temperature were measured in the range of 200-300 $\mathrm{Wm}^{-1}\mathrm{K}^{-}1$ (Hone et al., 2002; Yang et al., 2002). This might be due to the existence of defects in the surface of CNTs in real samples. Another measurement reported that the thermal conductivity for MWCNTs and SWCNTs at room temperature were 3000 $\mathrm{Wm}^{-1}\mathrm{K}^{-1}$ and 3500 $\mathrm{Wm}^{-1}\mathrm{K}^{-1}$, respectively (Pop et al., 2006). This value was greater than copper (385 $\mathrm{Wm}^{-1}\mathrm{K}^{-1}$). This means CNTs are superior for many applications such as in cooling of integrated circuit where fast dissipation of heat is required (Cao et al., 2001).

It was reported that the temperature stability of CNTs in vacuum and air is about 2800 °C and 750-900 °C, respectively (Thostenson et al., 2005). The specific heat of bundled SWCNTs at room temperature was close to that of bulk graphite (600 $\mathrm{mJg}^{-1}\mathrm{K}^{-1}$) (Hone et al., 2002).

2.3 Agglomeration of CNTs

In nature, the CNTs will mostly be present in bundled form. Highly entangled CNTs which are difficult to disperse will reduced performance below the theoretical assumptions. In order to maximize the CNTs dispersion much effort has been invested. Different techniques including mechanical treatments and chemical functionalization have been reported to dispersing the CNTs.

Mechanical treatment for dispersion of the CNTs includes high power sonication (Yu et al., 2007), shear mixing (Baskaran et al., 2005), ball milled (Dyke & Tour, 2003), and magnetic stirring in organic or highly polar solvents (Bystrzejewski et al., 2010). Even though these techniques can be used to dispersed the CNTs, however they can also cause CNTs to break and will reduce their aspect ratio (Vaisman et al., 2006).

There are two methods for chemical functionalization of CNTs which are covalent and non-covalent methods. There are two ways of covalent functionalization of CNTs which are functionalized at ends tube of CNTs or defects or functionalized at sidewalls of CNTs. The functionalization of ends and defect sites of the CNTs can only occurred when acids are used in CNTs purification and opening. In order to achieve this process, strong acids like HNO_3 (Tsang et al., 1994), HNO_3+H_2SO_4 (Dujardin et al., 1998) and H_2SO_4+$KMnO_4$ (Hiura et al., 1995) have been used resulting formation of carboxyl and other groups to functionalize the ends and defect sites of CNTs. The functionalization of CNTs sidewalls can be only happening if a highly reactive reagent is used. Processes including fluorination (Mickelson et al., 1998), addition of carbenes (Holzinger et al., 2001), addition of nitrenes (Holzinger et al., 2003) and addition of radicals (Peng et al., 2003) have been reported.

The interaction of non-covalent happens through adsorption of the chemical moieties onto the CNTs surface, either via π–π stacking interaction can form between chemical moieties and the graphitic sidewalls of the CNTs or through coulomb attraction for the situation of charged chemical moieties. The examples of non-covalent technique to dispersed CNTs are using surfactants (Di Crescenzo et al., 2014) and polymers (Bilalis et al., 2014). The polymer chains will wrapped around the CNTs surface while the surfactant molecules will be adsorbed on the surface of CNTs and make it soluble in aqueous or organic solvents.

Fujigaya and Nakashima had summarized the polymer wrapping on the surface of CNTs using π-conjugated polymers, aromatic polymers, non-aromatic polymers, cationic polymers and block polymers (Fujigaya & Nakashima, 2015). Example of dispersing CNTs by a π-conjugated polymer in solvents was carried out using poly(p-pheny-lenevinylene) derivatives (PPVs) as the polymer dispersant (Coleman et al., 1998). They found that the dispersion was stable up to three days before some of the soot start to precipitate. Polyimide was in the group of aromatic polymers used in polymer wrapping of CNTs surfaces. In 2006, Shigeta et al studied the solubilization of SWCNTs using totally aromatic polyimide (Shigeta et al., 2006). From visible-near IR absorption and near-IR fluorescence spectroscopy, they concluded that aromatic polyimides carrying sulfonate were highly capable of solubilizing a large amount of SWCNTs in solution. Poly(methyl methacrylate) (PMMA) (Baskaran et al., 2005) and poly(vinyl alchohol) (PVA) (Zhang et al., 2003) are examples for non-aromatic polymers used in wrapping SWCNTs. Dispersion using these types of polymers depended on the CH–π interaction between CH bonds of polymers and π bonding of CNTs. Polymers such as poly(diallyldimethylammonium chloride) (PDDA) (Leubner et al., 2012) and polyaniline (PANI) (Yan et al., 2007) are classified as cation polymers through interaction of the π-π stacking with CNTs surfaces. Kang and Taton have demonstrated the dispersion of SWCNTs using polystyrene-b-poly (acrylic acid) (PS-PAA) in dimethylformamide (DMF) solution (Kang & Taton, 2003). This is an example of using block polymer technique for CNTs dispersion.

The used of surfactants to disperse CNTs have great advantages because they can be easily removed from the system. From the beginning until now, a variety of choices of surfactants have been applied to disperse CNTs such as sodium dodecyl benzenesulfonate (SDBS) (Islam et al., 2003), dodecyl trimethylammonium bromide (DTAB) (Whitsitt & Barron, 2003), hexadecyltrimethylammonium bromide (CTAB) (Ryabenko et al., 2004), octyl phenol ethoxylate (Triton X-100) (Wang et al., 2004a) and sodium dodecyl sulfate (SDS) (Yu et al., 2007).

The dispersion of CNTs by covalent functionalization was reported to have good stability compared to non-covalent functionalization. However, chemical and electrical properties will be affected by the covalently attached moieties (Bystrzejewski et al., 2010).

Varieties of approaches have been made by the researchers in order to optimize the dispersion of CNTs. This was including either a single or combination technique of mechanical and chemical functionalization. Every technique has their owned advantages and disadvantages. It was depends on the researcher to choose the suitable technique based on their applications and experimental requirement.

2.4 ZnO nanoparticles

Zinc oxide (ZnO) is an intrinsically semiconducting material with direct band gap 3.37 eV at room temperature and high exciton energy 60 meV with piezoelectric, and pyroelectric properties (Wang et al., 2004c). ZnO is also a unique metal oxide that can be grown into various shape and size including highly ordered nanowire arrays (Subannajui et al., 2012), tower-like structures (Wang et al., 2007), nanorods (Bhat, 2008), nanobelts (Xing et al., 2010), nanosprings (Gao & Wang, 2005), nanocombs (Pan et al., 2005), and nanorings (Kong et al., 2004). Some of these structures are shown in Figure 2.7. ZnO has the widest range of morphology for many applications in the field of optoelectronics, sensors, transducers, and biomedical science.

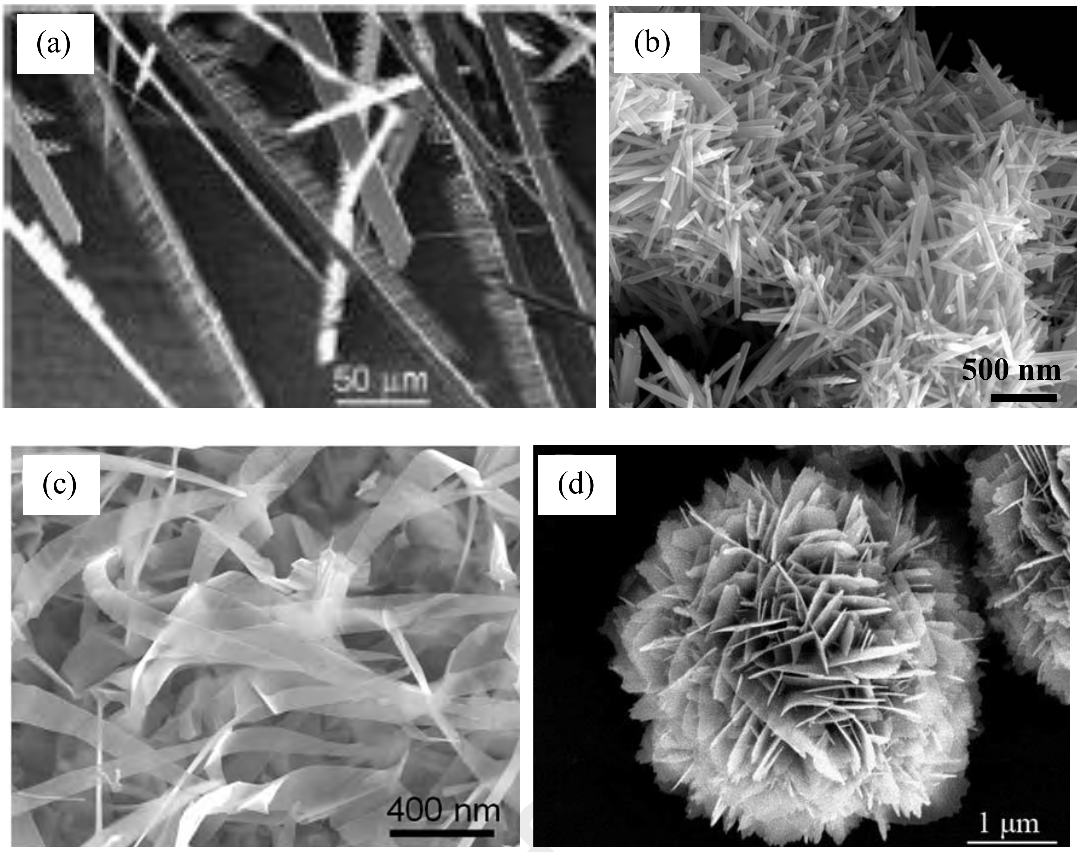

Figure 2.7: ZnO with various shape; (a) nanocombs (Pan et al., 2005), (b) nanorods (Bhat, 2008), (c) nanobelts (Xing et al., 2010) and (d) flowers like structures (Sun et al., 2012).

ZnO crystals can be in the form of wurtzite, zinc blende, and rocksalt (Rochelle salt) as shown in Figure 2.8(a), (b) and (c), respectively. The wurtzite structure are formed under room temperature and normal pressure while zinc blende must grow on cubic substrates to form stable structure and Rochelle salt can be obtained at very high pressure.

For a wurtzite crystal structure, ZnO has shape of hexagonal closed packed of O and Zn atoms in space group $P6_3mc$ in the Hermann-Mauguin notation and C_{6v}^4 in the Schoenflies notation with Zn atoms in tetrahedral sites (Kathalingam et al., 2015). The existent of inherent asymmetry along the c-axis in ZnO is due to wurtzite structure does not has center of inversion which means the anisotropic growth of the crystal occur along the [001] direction (Chen & Lo, 2011). In chemical solution mechanism growth, there is a possibility to create OH^- and Zn^{2+} ions at the same time in the solution regardless of the precursors. A very well deformed of ZnO nuclei can only be generated impulsively in the aqueous complex solution when the concentrations of Zn^{2+} and OH^- ions achieved critical value for the supersaturation of ZnO. Afterwards, the ZnO nucleated organized into energy minimizing hexagonal wurtzite structure.

The zinc blende structure of ZnO can be stabilized only by epitaxial growth on cubic substrates such as ZnS (Catti et al., 2003), GaAs/ZnS (Ashrafi et al., 2000), and Pt/Ti/SiO_2/Si (Chichvarina et al., 2015). The symmetry of the zinc blende is given by space group $F\bar{4}3m$ and T_d^2 in the Hermann-Mauguin and Schoenflies notation, respectively (Morkoç & Özgür, 2009). The zinc blende consists of two interpenetrating face-centered cubic (fcc) sublattices varied along the body diagonal by 25% of the length of the body diagonal.

ZnO can also be in the rocksalt or Rochelle salt structure at at relatively modest external hydrostatic pressures. This is due the decreases of the lattice dimensions produce from interionic Coulomb interaction to support the iconicity compared to covalent nature. The rocksalt have six fold coordinated structure and the space group symmetry is known as $Fm3m$ in the Hermann–Mauguin notation while O_h^5 in the Schoenflies notation (Morkoç & Özgür, 2009).

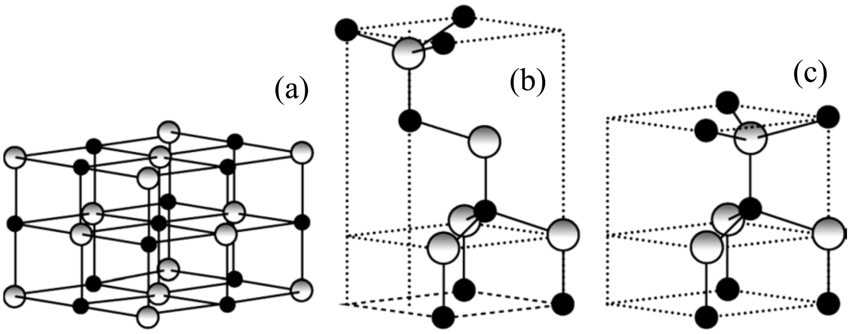

Figure 2.8: ZnO crystal structures: (a) cubic rocksalt, (b) cubic zinc blende and (c) hexagonal wurtzite. Shaded gray and black spheres indicate Zn and O atoms, respectively (Morkoç & Özgür, 2009).

2.5 ZnO Nanoparticles decorated CNTs

As discussed earlier, CNTs have gained much attention for their unique structures, absolute mechanical and electrical which brings to potential materials in many applications (Kim, 2006; Peng et al., 2014; Zare et al., 2015). Several researches have demonstrated enhancement of CNTs optical and electrical properties. These processes involved the modification the CNTs using other materials such as metal (Azamian et al., 2002; Kim et al., 2006a; Kim et al., 2006b) and semiconductor nanocrystals (Haremza et al., 2002; Švrček et al., 2006).

ZnO has appeared to be prospective materials to decorate with CNTs since it was used in various applications such as chemical and biological sensors (Özgür et al., 2005), photodetectors (Law & Thong, 2006), optical switches (Kind et al., 2002), optically pumped lasers (Huang et al., 2001) and field effect transistors (Ju et al., 2007). This is due ZnO having a wide band gap which is ~3.4 eV, huge exciton binding energy (~60 meV) and is easy to produce.

A few techniques have been demonstrated by other researchers to decorate ZnO nanoparticles with CNTs. Wang and his group have fabricated MWCNTs with ZnO decoration by using $ZnCl_2$ (Wang et al., 2008). In order to produce the carboxyl groups (-COOH), they treated MWCNTs with HNO_3. After that, the MWCNTs was soaked into $ZnCl_2$ and $NH_3.H_2O$ solution. Through chemical reaction between $NH_3.H_2O$ and $ZnCl_2$, they found the $Zn(NH_3)_4^{2+}$ was produced. After that, the carboxyl groups from MWCNTs reacted with $Zn(NH_3)_4^{2+}$ and gave CONH-$Zn(NH_3)_3^{2+}$ as results. The ionic CONH-$Zn(NH_3)_3^{2+}$ was reduced throughout the soaked time leading to the formation of ZnO nanoparticles on the MWCNTs surfaces.

In 2009, Fang and coworkers fabricated ZnO/MWCNTs by suspended the MWCNTs and ZnO in dimethylformamide solution followed by sonication to disperse the materials (Fang et al., 2009). They found that the combination of ZnO and MWCNTs fabricated was applied as efficient amperometric sensors for the detection of hydrazine.

Another technique that have been used to synthesis ZnO/CNTs was direct mixing followed by centrifuged with different solvents such as diethylene glycol, ammonia and deionized water as demonstrated by many researchers (Sui et al., 2013; Wayu et al., 2013). The interaction of ZnO and CNTs was accomplished with the existent of binder such as polyethyleneimine (Sui et al., 2013).

2.6 Adsorption properties of CNTs

CNTs have gain great attention for environmental applications especially in water treatment. This was due to the potential of CNTs or CNTs based composites as adsorbent of dyes. Several examples involving CNTs as dye remover is summarized in Table 2.1.

A study to investigate adsorption efficiency of CNTs towards Procion Red MX-5B at various pHs and temperatures (Wu, 2007) found that the adsorbed dosage increased with amount of CNTs but the adsorption capacity initially increased with amount of CNTs (<0.25 g/l) and then reduced as the amount of CNTs increased further (>0.25 g/l). They determined the free energy of adsorption (ΔG^o), enthalpy (ΔH^o) and activation energy (E_a) and proposed that the adsorption of Procion Red MX-5B on CNTs was predominantly by physisorption.

The removal of safranine O (SO) by using activated carbon (AC), MWCNTs and cadmium hydroxide nanowire loaded on activated carbon ($Cd(OH)_2$- NW-AC) was reported by Ghaedi and co-workers (Ghaedi et al., 2012). Several parameters such as pH, temperature, concentration of the dye, amount of adsorbents, and contact time on the SO adsorption efficiency for all adsorbents were investigated. The experimental data was correlated for all adsorbents with adsorption models like Langmuir, Freundlich, Temkin, and Dubinin–Radushkevich. From the models, they discovered that adsorption of SO on all adsorbents was endothermic and feasible in nature. From kinetic analysis of the adsorption process, they have suggested the adsorption process was best fitted to the pseudo-second-order kinetics which means there was involvement of particle diffusion mechanism.

The efficiency of MWCNTs as adsorption material for Acid Red 18 solution has been examined (Shirmardi et al., 2012). They conducted the experiment by varying parameters such as contact time, pH, adsorbent dosage, and initial dye concentration. They discovered that the rate of dye adsorption increased when the amount of adsorbent increased but the dosage of adsorbed dyes per mass unit of adsorbent reduced. From experiment involving pH, they found that the best pH was acidic with value of pH equal to 3. They also fitted their experimental data with adsorption models and suggested that this experiment was best fitted to the Langmuir model (R^2=0.985) and maximum adsorption capacity obtained was 166.67 mg/g. From kinetic model they estimated that this experiment was best fitted to the pseudo second order which the correlation coefficient value, R^2 equal to 0.999.

Yao and co-workers studied the effect of temperature towards adsorption of methylene blue (MB) dye solution by using CNTs as adsorbents (Yao et al., 2010). They analyzed experimental data with two adsorption models which were the Langmuir and the Freundlich models and found that the Langmuir model gave better fitting compared than the Freudlich model. They also examined the adsorption in kinetic analyses by using pseudo-first and second-order models and the intraparticle diffusion model. Based on the regression results, they claimed that the adsorption kinetics was more accurately represented by the pseudo-second-order model. From negative values of ΔG^o obtained, they suggested that adsorption of MB on CNTs was a spontaneous and endothermic process.

Shahryani and his teams reported experimental results for the adsorption of MB dye solution by using CNTs (Zohre et al., 2010). They studied different parameters such as temperature, initial dye concentration, CNTs dosage, and pH. From their results, they proposed the removal of MB dye was enhanced with the increasing initial concentration of MB dye, amount of CNTs and temperature. From the experiment they found that the optimum amount of CNTs to adsorb 90% of MB dye solution is 400 mg L^{-1}. They also claimed the adsorption process was best described by the pseudo-second-order kinetic model and the Sips model.

Rodrígyez et al. investigated the effect of cationic dye (MB) and anionic dye (orange II (OII)) on MWCNTs and carbon nanofibers (CNF) as adsorbents (Rodriguez et al., 2010). Several parameters were investigated such as pH, temperature and surface modification of adsorbent. They found that optimum pH of OII and MB removed by MWCNTs were at 3 and 7, respectively while maximum removals by CNF were achieved at pH 9 and 5 for OII and MB, respectively. They found that the equilibrium data for both dyes and adsorbents were best described by Langmuir model. They concluded that both MWCNTs and CNF can be used as adsorbents for cationic or anionic dyes solution.

MWCNTs and powdered activated carbon (AC) have been used to remove Reactive Red M-2BE textile dye from aqueous solutions by Machado and co-workers (Machado et al., 2011). For their experiment several parameters had been varied such as pH, shaking time and temperature on adsorption capacity. They found for MWCNTs and AC, the adsorption of dye was favorable in acidic pH region which is at pH 2. For kinetic model, they discovered the Avrami fractional-order gave the best fit to the experimental data compared to other kinetic models while for equilibrium model, the best fitted was found to the Liu model.

Table 2.1: Dye adsorption of CNTs.

CNTs	Treatment	Dye adsorbed	q_e (mg/g)	Reference
MWCNTs		Procion red MX-5B	44.68	(Wu, 2007)
MWCNTs	HCl	Safranine O	43.48	(Ghaedi et al., 2012)
MWCNTs		Acid red 18	166.67	(Shirmardi et al., 2012)
CNTs		Methylene blue	64.7	(Yao et al., 2010)
MWCNTs		Methylene blue	132.6	(Zohre et al., 2010)
MWCNTs		Orange II, Methylene blue	66.12, 54.54	(Rodriguez et al., 2010)
MWCNTs		Reactive red M-2BE	335.7	(Machado et al., 2011)

q_e = maximum adsorption capacity

2.6.1 Adsorption equilibrium models

In this study, equilibrium data were modeled using the Langmuir (Langmuir, 1918; Patiha et al., 2016), Freundlich (Freundlich, 1906) and Temkin (Temkin & Pyzhev, 1940) models. The different models are described in the next section.

2.6.1.1 The Langmuir model

The Langmuir model can be expressed by the following equation:

$$q_e = q_m \frac{k_L C_e}{1 + k_L C_e} \tag{2.2}$$

Langmuir adsorption parameters were determined by transforming the Langmuir Equation 2.2 into linear form:

$$\frac{1}{q_e} = \frac{1}{q_m} + \frac{1}{q_m k_L C_e} \qquad (2.3)$$

or in another linear form:

$$\frac{C_e}{q_e} = \frac{C_e}{q_m} + \frac{1}{q_m k_L} \qquad (2.4)$$

where q_e (mg/g) is the quantity of substance adsorbed per gram of adsorbent, C_e (mg/L) is the equilibrium concentration of adsorbates in solution, k_L (L/mg) denotes the Langmuir constant that relates to the affinity of binding sites and q_m (mg/g) is a theoretical limit of adsorption capacity when the monolayer surface is fully covered with adsorbate molecules.

The model was based on Irving Langmuir who suggested the behavior of adsorption of gases on solid surfaces as a chemical phenomenon (Langmuir, 1918). Even though in the original model the mechanism aspects of the adsorption process were not discussed, it provided information regarding the uptake capabilities and the efficiency of the general equilibrium adsorption process. Other assumptions were as followed:

(1) Number of adsorption sites was fixed and for any temperature and pressure a portion of surface sites, θ is occupied by adsorbed molecules and the available sites are 1-θ.

(2) The probability of adsorption on all unoccupied sites is equal.

(3) Only one adsorbate molecule adsorb with one unoccupied site.

(4) There is no interaction between adsorbed molecules with each other.

Another parameter that can be determined from this model is the separation factor or equilibrium parameter written as R_L. With this parameter the feasibility or favorability of adsorption in a given concentration towards adsorbent can be estimated (Hall et al., 1966). It is written as follows;

$$R_L = \frac{1}{1+k_L C_o} \tag{2.5}$$

where k_L is the Langmuir adsorption constant (L/mg) and C_o is the initial substance concentration. From this relation, it was established that (Hall et al., 1966):

(1) $0 < R_L < 1$ for favorable adsorption;

(2) $R_L > 1$ for unfavorable adsorption;

(3) $R_L = 1$ for linear adsorption; and

(4) $R_L = 0$ for irreversible adsorption.

2.6.1.2 The Freundlich model

The Freundlich model also known as Halsey-Taylor has the following mathematical form:

$$q_e = k_F C_e^{1/n} \tag{2.6}$$

Adsorption parameters for Freundlich model were determined by transforming the Freundlich Equation 2.2 into linear form:

$$\log q_e = \log k_F + \frac{1}{n} \log C_e \tag{2.7}$$

where q_e is the quantity of substance adsorbed per gram of adsorbent (mg/g); k_F and n are the Freundlich constants, which represent the adsorption capacity and the adsorption strength or feasibility, respectively.

The magnitude of n expressed the favourability or feasibility of adsorption and the degree of heterogeneity of the adsorbent surface which describes as (Sun et al., 2013):

(1) If n = 2-10 then the adsorption is good.

(2) If n = 1-2 then the adsorption is moderately difficult.

(3) If $n < 1$ then the adsorption is poor.

n has an asymptotic value if the increment of pressure is without bound. The constants k_F and n changed with increasing temperature. This is in line with empirical observation which is the amount of adsorbed increase slower and more pressure needed in order to achieve saturated on the surface (Rosa et al., 2008).

2.6.1.3 Temkin model

This model which also known as Slygin-Frumkin and have a factor that clearly about interactions between the adsorbate and the adsorbent. This model proposed by disregarding value of concentrations, that the heat of adsorption of all molecules in the layer would reduce relatively linear than logarithmic with coverage (Aharoni & Ungarish, 1977).

As implied in the equation, the derivation is described by a similar distribution of binding energies which can be up to some optimum binding energy was carried out by plotting the amount of adsorbed q_e against $ln\ C_e$ and the constants were determined from the slope and intercept. The model is given by the following equation (Temkin & Pyzhev, 1940):

$$q_e = \frac{RT}{b_T}\ln(k_T C_e) \tag{2.8}$$

$$q_e = \frac{RT}{b_T}\ln k_T + \frac{RT}{b_T}\ln C_e; \qquad B_T = \frac{RT}{b_T} \tag{2.9}$$

$$q_e = B_T \ln k_T + B_T \ln C_e \tag{2.10}$$

where R is a universal gas constant (8.314 J/mol/K), T is an absolute temperature (K), k_T is the equilibrium binding constant (L/mol) corresponding to maximum binding energy, b_T is a Temkin isotherm constant and B_T (J/mol) is a constant related to adsorption heat.

2.6.2 Kinetic Adsorption Model

Adsorption is a method regarding the transformation of molecules from solution to the adsorbent surface. The transient behavior of the adsorption can be determined by using several kinetic models such as pseudo-first-order, pseudo-second-order and intraparticle diffusion models.

2.6.2.1 Pseudo-first-order Kinetic Model

The pseudo-first-order kinetic model can be represented by the following Lagergren rate equation:

$$\frac{dq_t}{dt} = k_1(q_e - q_t) \tag{2.11}$$

Integrating this equation for the boundary conditions $t = 0$ to $t = t$ and $q = 0$ to $q = q_t$, gives:

$$\ln(q_e - q_t) = \ln(q_e) - k_1 t \tag{2.12}$$

where q_e and q_t are the quantity of substance adsorbed (mg/g) at equilibrium and at contact time t (min), respectively and k_1 is the pseudo-first-order rate constant (min^{-1}).

2.6.2.2 Pseudo-second-order Kinetic Model

The pseudo-second-order equation based on adsorption equilibrium capacity can be expressed as:

$$\frac{dq}{dt} = k_2 (q_e - q)^2 \tag{2.13}$$

Rearranging the variables in Equation 2.13 gives:

$$\frac{dq}{(q_e - q)^2} = k_2 dt \tag{2.14}$$

Taking into account, the boundary conditions $t = 0$ to $t = t$ and $q = 0$ to $q = q_t$, the integrated linear form of Equation 2.14 can be rearranged to determine:

$$\frac{t}{q} = \frac{1}{k_2 q_e^2} + \frac{t}{q_e} \tag{2.15}$$

where q_e (mg/g) and q (mg/g) are the quantity of substance adsorbed onto adsorbent at equilibrium and at various times, t (min), and k_2 is the rate constant of the pseudo second-order model for adsorption (mg/g min) (Mall et al., 2006; Wu, 2007). The slope and intercept of the linear plot of t/q as a function of t yielded the values of q_e and k_2. Moreover, the initial adsorption rate, h (mg/g min) can be calculated using the equation:

$$h = k_2 q_e^2 \tag{2.16}$$

2.6.2.3 Intraparticle diffusion Kinetic Model

The adsorption in porous solids can be classified into three phase if motion of substance from bulk liquid to liquid film that only around the adsorbent is ignored (Rengaraj et al., 2004):

(1) Film diffusion or boundary layer diffusion or outer diffusion is external molecules transfer of adsorbate through the liquid phase to the adsorbent outer surface.

(2) Intraparticle diffusion or inner diffusion is phenomenon where molecules from the adsorbate transfer to the pores or capillaries of the adsorbent internal structure.

(3) Adsorption occurs only on the active sites which can either be on the inner or the outer of adsorbent surfaces.

Overall rate of adsorption system was determined from the slowest steps. The last step is not being taken into account as rate limiting step due to very rapid process. Commonly, rate of adsorption is ruled by film diffusion or intraparticle diffusion or both. The intraparticle diffusion model was evaluated to explain the diffusion mechanism because the pseudo first-order and pseudo second-order did not distinguished the diffusion mechanism. This model was derived by Weber and Morris in 1963 which is expressed as (Weber & Morris, 1963):

$$q_t = k_i t^{1/2} + C \tag{2.17}$$

where C is the intercept and k_i is the intraparticle diffusion rate constant (mg/mg min$^{0.5}$), which can be estimated from the slope of the linear plot of q versus $t^{1/2}$ (Mall et al., 2006; Wu, 2007). If the regression of q versus $t^{1/2}$ is linear and passes through the origin (intercept equal to zero), then intraparticle diffusion is the only rate-limiting step (Kannan & Sundaram, 2001; Özcan & Özcan, 2005).

2.7 Chemical Sensing Properties of CNTs

Since the year 2000, the potential for CNTs chemical gas sensing applications has attracted extensive research effort for three significant reasons. First, CNTs are surface reacting materials, i.e., they are composed entirely of surface atoms where adsorbed gas molecules can dramatically change CNTs electrical properties at room temperature. Next, the ballistic electronic transport along the CNTs axis provides excellent transmission of the altered electrical signal to the external contact. Third, the long-term performance of CNTs based sensor may be stable due to their chemically robust graphitic surface. CNTs for gas sensing at room temperature are of great interest because most currently available sensors operate at elevated temperatures. A brief review of research on CNTs for gas sensing is given in this section. Due to the nature of this research, the discussion will focus on non-functionalized as-grown CNTs based gas sensors and conductance-based detection vapor sensors.

The pioneer works by Kong, et al. (Kong et al., 2000) and Collins, et al. (Collins et al., 2000) were the first to report that the adsorption of certain gas molecules can dramatically change the electrical conductance of SWCNTs. Kong and coworkers investigated individual p-type semiconducting SWCNTs as a resistive sensor for NO_2 and NH_3 detection at room temperature in air or argon. They exhibited that conductivity of SWCNTs with p-type will be raised and reduce when exposed to oxiding agent or electron acceptor (NO_2) and reducing agent or electron donor (NH_3), respectively (Kong et al., 2000). They estimated the lowest detection of SWCNTs to be ~2 ppm for NO_2 and ~0.1% for NH_3. They also discovered recovery time of the sensor to be 12 hours and it was significantly reduced by heating the sample in air at 200 ºC (Kong et al., 2000).

Using transport measurement and scanning tunneling spectroscopy, Collins and coworkers demonstrated that the electrical resistance, thermoelectric power and local density of states of SWCNTs is sensitive to air or oxygen exposure. By alternating the medium between air (or oxygen) and vacuum, a reversible change in SWCNTs resistance was observed (Collins et al., 2000). They attributed this variation in resistance to the charge transfer between adsorbed oxygen molecules and SWCNTs. However, in order to fully recover, the sample had to be heated above 110 ºC for several hours in vacuum for oxygen to be desorbed (Collins et al., 2000). The authors also suggested that any intrinsic properties measurement on as-prepared CNTs could be compromised by extrinsic air exposure (oxygen exposure). Therefore they claimed that the electronic properties of a given nanotube are not only specified by its chirality and diameter but also depend on gas exposure history.

Li, et al. investigated SWCNTs based sensor for the detection of NO_2 and nitrotoluene vapors at room temperature (Li et al., 2003). Randomly orientated SWCNTs were dispersed in dimethylformamide (DMF) and drop-deposited on a sensor platform with interdigitated electrodes patterned on top. The SWCNTs sensor responded in seconds to the presence of NO_2 within the concentration range of 6-100 ppm while pure nitrogen was used as carrier gas for dilution and purging. The conductance of the SWCNTs sensor was increased significantly by exposure to the oxidizing agent NO_2. Due to the high bonding energy between SWCNTs and NO_2, the sensor recovered slowly with a recovery time on the order of 10 hours, which is consistent with the results reported by other researchers (Kong et al., 2000). Jing Li and coworkers applied ultraviolet (UV) light illumination during recovery and successfully accelerated the recovery time to 10 min (Kong et al., 2000; Li et al., 2003). They reported that the UV illumination lowered desorption energy barrier of CNTs thus facilitating the NO_2 desorption.

Chen, et al. were the first to discover the photo-induced molecular desorption in molecule-CNTs systems (Chen et al., 2001). They found that UV light induced desorption of oxygen, NO_2, and NH_3 molecules can drastically alter the electrical characteristics of semiconducting SWCNTs. Although the mechanism has not been fully understood, they suggested that the photodesorption in CNTs is a non-thermal process and wavelength dependent.

Zhao, et al. have performed first principles calculations on the electronic properties of SWCNTs upon adsorption of various gas molecules, such as NO_2, O_2, NH_3, N_2, CO_2, CH_4, H_2O, H_2 and Ar (Zhao et al., 2002). The authors found all molecules, either electron donor or electron acceptor, are weakly adsorbed on SWCNTs with small charge transfer. They also determined the equilibrium position, adsorption energy, charge transfer, and electronic band structures for SWCNTs with variety structures.

Bradley and coworkers used SWCNTs field-effect transistor to detect NH_3 through the shift of gate voltage (Bradley et al., 2003). They determined that the shift of gate voltage is due to the charge transfer between SWCNTs and adsorbed NH_3 molecules. Their experiments measured the amount of charge transfer to be approximately 0.04 electrons per NH_3 molecule.

Qi, et al. fabricated arrays of electrical devices with each comprising ensembles of SWCNTs bridging metal electrodes for NO_2 detection (Qi et al., 2003). The sensor is capable of detecting NO_2 at less than 1 ppb (parts per billion) concentration. Their calculations indicate that NO_2 binds to the SWCNTs surface with energy of 0.8 eV and withdraws approximately 0.1 electrons per molecule.

Chang and coworkers investigated the adsorption of NH_3 and NO_2 molecules on semiconducting (10,0) SWCNTs through density function theory (Chang et al., 2001). Their calculation shows that the binding energies are less than 0.5 eV for both molecules (0.18 eV for NH_3 and 0.42 for NO_2). Therefore they claim that both NH_3 and NO_2 molecules bind to nanotubes by physisorption and the electron charge transfer is the major mechanism for the change of conductivity.

Although most of the attention has focused on SWCNTs for gas sensing, MWCNTs do present one attractive feature with respect to SWCNTs, i.e., low production cost. Recently, there have been increasing numbers of reports on the studies of MWCNTs for gas detection. Cantalini, et al. reported the influence of the catalyst geometry on the growth of MWNTs and their electrical response to NO_2 of 10-100 ppb concentrations at different operating temperatures ranging from 25 to 215ºC (Cantalini et al., 2003). The resistive gas sensor was fabricated by PECVD depositing MWCNTs on Pt interdigitated electrodes based on Si/Si_3N_4 substrate. The maximum response was found at 165ºC and the sensor showed fast dynamic response and reproducible electrical properties.

Based on a similar sensor structure, Valentini and coworkers studied CH_4 detection by MWCNTs grown on a Ni catalyst (Valentini et al., 2004). They demonstrated that oxygen molecules are chemisorbed when CNTs walls contain defects and this caused the electrical response to CH_4. The authors also suggest that the semiconducting CNTs could be converted from p-type to n-type by adsorption of oxygen molecules at elevated temperature.

Wang, et al. investigated the effect of MWCNTs resistive sensor for NH_3 detection at room temperature (Wang et al., 2004b). The sensor was fabricated by patterning Ti/Au electrode on top of ultrasonically dispersed MWCNTs using evaporation and lift-off techniques. They observed a significant decrease in sensor conductance upon exposure to 1% NH_3 in air. The authors also demonstrated that the sensitivity is linearly proportional to the NH_3 concentration ranging from 10 to 200 ppm. While in vacuum, the sensor required more than 6 hours at 250 ºC to recover to baseline condition, therefore they conclude that the sensor response involved both physisorption and chemisorption.

CHAPTER 3: ADSORPTION OF RHODAMINE 6G ON MWCNTS

3.1 Introduction

CNTs as adsorbents have been applied to the removing of many kinds of organic and inorganic contaminants including 1,2-dichlorobenzene (Peng et al., 2003), trihalomethanes (Lu et al., 2005), microcystins (Yan et al., 2006), fluoride (Li et al., 2001), nickel (Chen & Wang, 2006) and arsenate (Peng et al., 2005). The effect of temperature on the equilibrium adsorption of methylene blue dye from aqueous solution using CNTs was reported by (Yao et al., 2010). Their equilibrium adsorption data were analyzed based on the Langmuir and Freundlich models. They revealed that Langmuir isotherm fitted the experimental results well. They also analyzed the kinetic behavior using the pseudo-first, second-order and the intraparticle diffusion models. They found that the regression results showed that the adsorption kinetics was more accurately represented by pseudo-second-order model. The activation energy of system (E_a) was calculated as 18.54 kJ/mol. Standard free energy changes (ΔG^o), standard enthalpy change (ΔH^o), and standard entropy change (ΔS^o) were obtained using adsorption equilibrium constants obtained from the Langmuir isotherm at different temperatures. All ΔG^o values were negative; the ΔH^o values and ΔS^o values of CNTs were 7.29 kJ/mol and 64.6 J/mol K, respectively. From the results, they suggested that methylene blue adsorption on CNTs was a spontaneous and endothermic process.

The adsorption efficiency of CNTs for Procion Red MX-5B at various pHs and temperatures was examined by (Wu, 2007). They found that the amount adsorbed increased with the CNTs dosage; however, the adsorption capacity initially increased with the CNTs dosage (<0.25 g/l) and then declined as the CNTs dosage increased further (>0.25 g/l). They determined the linear correlation coefficients and standard deviations of Langmuir and Freundlich isotherms and the results revealed that Langmuir isotherm fitted the experimental results well. They also conducted kinetic analyses using pseudo first-order, second-order and the intraparticle diffusion models and discovered that the regression results showed that the adsorption kinetics were more accurately represented by a pseudo second-order model. They calculated ΔH^o and ΔS^o were 31.55 kJ/mol and 216.99 J/mol K, respectively, at pH 6.5 and 41.47 kJ/mol and 244.64 J/molK at pH 10. The E_a value was 33.35 kJ/mol at pH 6.5. They suggested that the adsorption of Procion Red MX-5B onto CNTs was predominantly physisorption.

Kuo and his group had examined the feasibility of removing direct dyes C.I. Direct Yellow 86 (DY86) and C.I. Direct Red 224 (DR224) from aqueous solutions using CNTs (Kuo et al., 2008). They evaluated the effects of dye concentration, CNTs dosage, ionic strength and temperature on adsorption of direct dyes by CNTs. Pseudo second-order, intraparticle diffusion and Bangham models were adopted to evaluate experimental data and thereby elucidate the kinetic adsorption process. Additionally, this study used the Langmuir, Freundlich, Dubinin and Radushkevich (D–R) and Temkin isotherms to describe equilibrium adsorption. They found that the adsorption percentage of direct dyes increased with CNTs dosage, NaCl addition and temperature increase. Conversely, the adsorption percentage of direct dyes decreased as dye concentration increased. For adsorption kinetics, they found that pseudo second-order model was best fitted to their results. Based on the regressions of intraparticle diffusion and Bangham models, they suggested data that the adsorption of direct dyes onto CNTs involved intraparticle diffusion, but that was not the only rate limiting step. They evaluated the equilibrium adsorption of DR86 was best fitted in the Freundlich isotherm and that DR224 was best fitted in the D–R isotherm. The capacity of CNTs to adsorb DY86 and DR224 was reported as 56.2 and 61.3 mg/g, respectively. They estimated for DY86, ΔH^o and ΔS^o were 13.69 kJ/mol and 139.51 J/molK, respectively, and those for DR224 were 24.29 kJ/mol and 172.06 J/molK, respectively. From the values of ΔH^o,

ΔG^o and E_a they concluded that the adsorption of direct dyes onto CNTs was predominantly the physisorption process.

In this chapter the results of a study on the adsorption behavior of R6G on pristine MWCNTs as the adsorption materials are presented. Diameter effects and amount of adsorbent which are expected to influence the properties of the MWCNTs as adsorbent have been investigated. The equilibrium adsorption data were analyzed the Langmuir, Freundlich and Temkin models. Kinetic analysis of the R6G adsorption using different amounts of MWCNTs based on the the pseudo first-order, pseudo second-order and intraparticle diffusion models were performed.

3.2 Materials

Rhodamine 6G which is also called as R6G, Rh6G, C.I. Pigment Red 81, C.I. Pigment Red 169 used in this experiment, is a reactive azo dye with a molecular structure as shown in Figure 3.1, was purchased from Aldrich (M_w = 479.01 g/mol) and used without further purification.

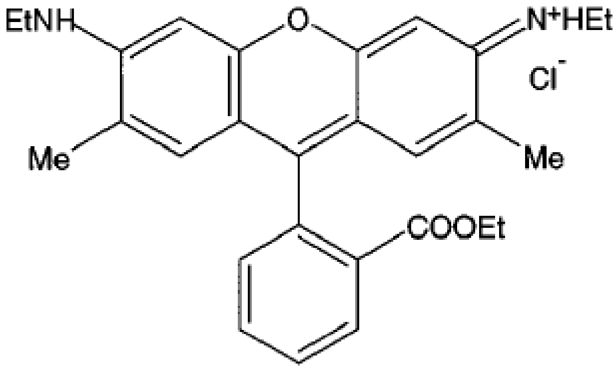

Figure 3.1: Molecular structure of R6G (Elking et al., 1996).

The UV-vis absorption spectra of R6G in aqueous solution are classified by three main bands as shown in Figure 3.2. The absorbance was measured with water as reference. The first and second bands which represent the absorption of benzene like and naphthalene like structures in the molecule were in the UV region, λ_{max} = 246 nm and 345 nm, respectively (Dükkancı et al., 2010). The most intense peak was due to chromophoric components for color of R6G resulting from aromatic rings connected by azo group, which is in the visible region of λ_{max} = 526 nm (Dükkancı et al., 2010). A high energy shoulder band at around 495 nm is due to the aggregates of R6G (sometimes called H dimer) (Selwyn & Steinfeld, 1972). These dimers are formed through van der Waals dye-dye interactions and Rhodamine-water (counterions) interactions (Dare-Doyen et al., 2003). In our experiment, the adsorption process was monitored by recording the change of the absorbance maximum of R6G (λ_{max} = 526 nm).

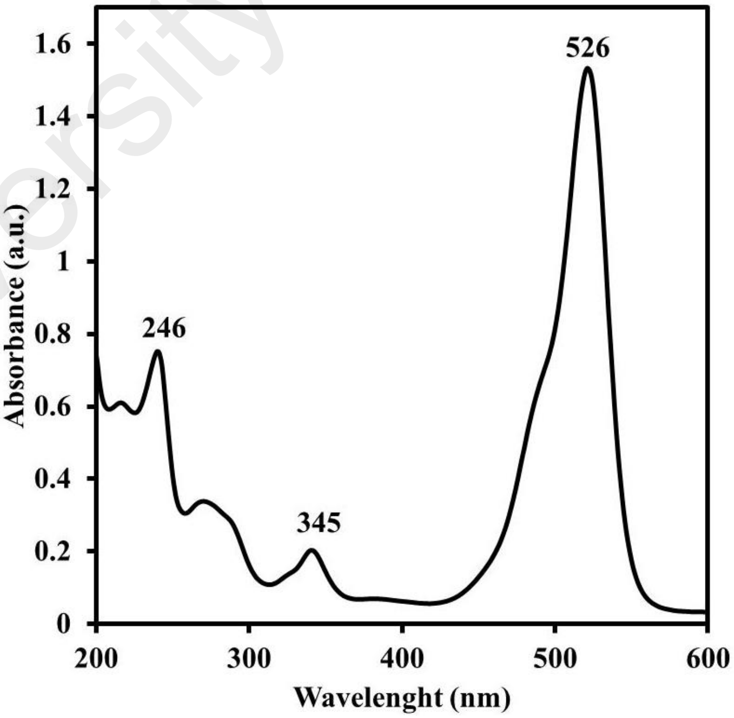

Figure 3.2: UV–vis absorption spectra of aqueous solutions of Rhodamine 6G.

MWCNTs used in this experiment were obtained from Timesnano, China reportedly synthesized by the chemical vapor deposition (CVD) technique. Outer diameter for MWCNTs used in this work ranged from ~8, 20-30 and ~50 nm with length 0.5-2, 10-30, and 10-20 µm, respectively reported from High Resolution Transmission Electron Microscopy (HRTEM). The MWCNTs have electrical conductivity more than 100Scm^{-1}, purity more than 98 wt. % with ash content less than 1.5 wt. %. These values were based on Thermogravimetric Analysis (TGA) and Transmission Electron Microscopy (TEM) measurements. Special surface area calculated using Brunauer-Emmett-Teller (BET) method were; ~8 nm (>350 m^{2}g^{-1}), 20-30 nm (>110 m^{2}g^{-1}) and ~50 nm (60 m^{2}g^{-1}). The MWCNTs properties as specified by the manufacturer are summarized in Table 3.1.

Table 3.1: Specifications of MWCNTs with different diameters ("Carbon Nanotubes - Price - Chinese Academy of Sciences, Chengdu Organic Chemistry Co., Ltd.,").

Properties	MWCNTs			Method of measurement
*Outer diameter (nm)	~8	20-30	~50	HRTEM, Raman
*Purity (wt.%)	>98	>98	>98	TGA, TEM
*Length (µm)	0.5-2	10-30	10-20	TEM
*Special surface area (m^2/g)	>350	>110	>60	BET
*Ash (wt.%)	<1.5	<1.5	<1.5	TGA
*Electrical conductivity (S/cm)	>100	>100	>100	

* As given by manufacturer.

3.3 Experimental methods

The study on the MWCNTs size effect on the adsorption of R6G was conducted based on the change in concentration aqueous solution of R6G with time. The concentration of R6G and amount of MWCNTs used in this experiment were fixed at 10 mg/L and 8 mg, respectively. The study for the effect of amount on adsorption R6G on MWCNTs was conducted with various amounts of MWCNTs ranging from 2-12 mg for the MWCNTs of different diameters and at the same concentration of R6G of 10 mg/L.

The adsorption activities of the MWCNTs were evaluated for the adsorption of R6G solution as target pollution with continuous stirring at 800 rpm. Different amounts of MWCNTs with different diameters (~8, 20-30 and ~50 nm) were added into 100 ml of R6G solution at a concentration of 10 mg/L for a total reaction time of 50 minutes. At every 5 minutes 4 ml of the R6G solution was withdrawn from the reaction beaker, centrifuged and analyzed by UV-vis spectrometry. The example of this plot obtained is as Figure 3.3. From this graph, the concentration of adsorbed R6G was calculated by using the relationship:

$$C_t = \frac{A_0 - A_t}{A_o} \times C_o \tag{3.1}$$

where A_o and A_t are the UV-vis absorbance peak intensity at 526 nm at $t = 0$ and $t = t$, respectively, C_o is initial concentration of R6G which was 10 mg/L.

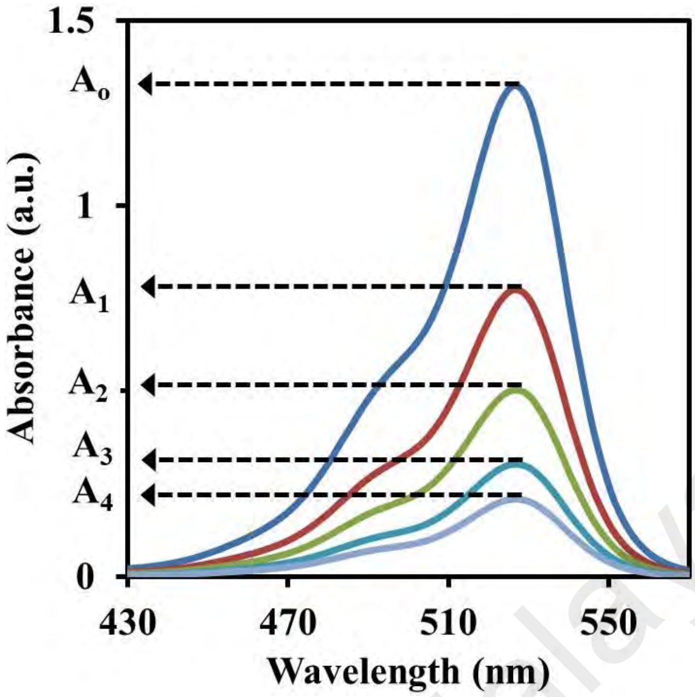

Figure 3.3: Absorbance versus wavelength for aqueous solution just after adding the CNTs (A_o), after 5 minutes (A_1), 10 minutes (A_2), 15 minutes (A_3) and 20 minutes (A_4).

Amount of R6G adsorbed at reaction time was calculated from the equation:

$$q_t = \frac{C_o - C_t}{W} \times V \tag{3.2}$$

The equilibrium adsorption of R6G was calculated by this equation:

$$q_e = \frac{C_o - C_e}{W} \times V \tag{3.3}$$

where C_o, C_e and C_t (mg/L) are concentrations of R6G at initial, equilibrium and after certain reaction time, t, respectively, V (L) is the volume of the solution and W (g) is the mass of adsorbent used. The equilibrium data were modeled using the Langmuir (Langmuir, 1918; Patiha et al., 2016), Freundlich (Freundlich, 1906) and Temkin (Temkin & Pyzhev, 1940) models. Removal efficiency in percentage was calculated using the following formula:

$$Removal\ efficiency\ (\%) = \frac{C_o - C_t}{C_o} \times 100 \tag{3.4}$$

3.4 Results and discussion

3.4.1 Effect of MWCNTs diameters on adsorption of R6G

The characteristic UV-vis absorption peak for R6G at about 526 nm for solutions reacted with MWCNTs of different diameters of MWCNTs at 5 minutes interval up to 50 minutes are shown in Figure 3.4. From these peaks the time evolution of the R6G concentration can be evaluated denoting the amount adsorbed. Adsorption was observed to occur at various degrees for all MWCNTs samples. From the image in the inset of Figure 3.4(a), the R6G solution which was initially very dark-reddish in color changed into a very pale color solution after 5 minutes using MWCNTs for MWCNTs of diameter of ~8 nm at room temperature, and the continued stirring resulted in clean and colorless solution after 50 minutes. These changes were confirmed when R6G UV-vis absorbance intensity peaks reduced from initial to 50 min reaction times.

For MWCNTs with diameters 20-30 nm (Figure 3.4(b)) less effect was observed compared to ~8 nm MWCNTs. It took about 50 min for this sample to reduce to half of initial R6G UV-vis absorbance peak intensity. The change of R6G color was barely noticeable by naked eyes based on the images in the inset of Figure 3.4(b). The lowest R6G adsorption was observed when ~50 nm MWCNTs were used as adsorbent (Figure 3.4(c)). The reduction of R6G UV-vis absorbance intensity was barely noticeable for the whole duration of the 50 minutes based on the image in the inset of Figure 3.4(c).

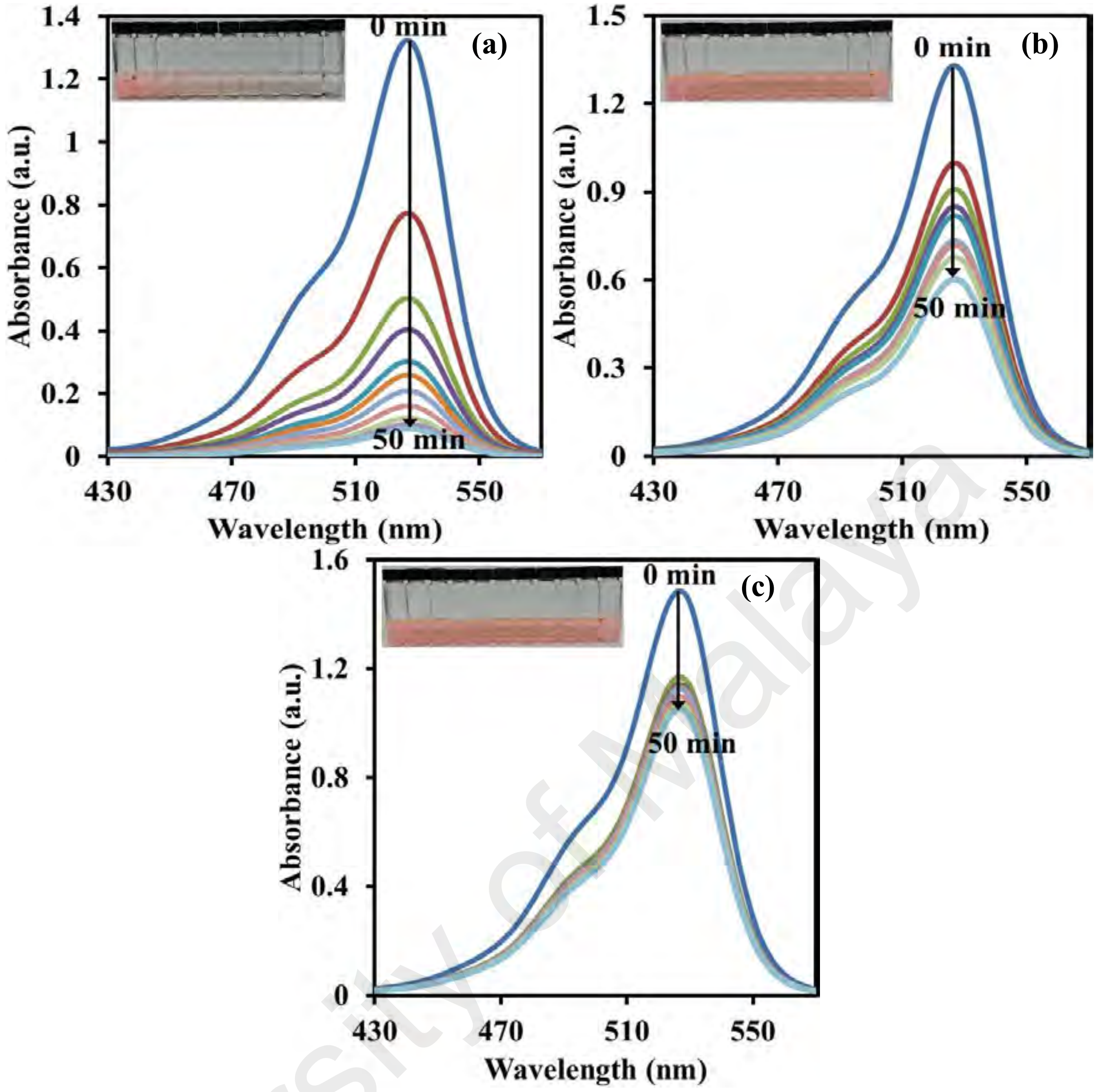

Figure 3.4: UV-vis spectra of degradation R6G dye from 0 min to 50 min with existent of different diameters MWCNTs; (a) ~8 nm, (b) 20-30 nm and (c) ~50 nm as adsorber.

MWCNTs used in this study had several different properties such as length, external diameter and surface area as listed in Table 3.1. The high adsorption capacity of MWCNTs was attributed to their large surface areas, and their affinity towards both volatile and semi-volatile organic compounds were achieved through hydrogen bonding interactions, π–π stacking interactions, van der Waals forces, and hydrophobic interactions (Yu et al., 2014). In this experiment, it is predicted that the chemical structure of R6G that has rich aromatic rings and cationic atoms (N^+) (Figure 3.1) was favorable for adsorbing on the MWCNTs surface through π−π stacking and ionic interaction. The adsorption interactions usually occur on the MWCNTs walls and in the interstitial spaces between the tubes. So, it is reasonable for the MWCNTs diameter with the highest surface areas have the highest R6G adsorption.

The time evolution of the mount of adsorption R6G was calculated by evaluating the time varying R6G concentration in the solution using Equation 3.2. The plot of q_t versus time is shown in Figure 3.5. For all MWCNTs samples used, the adsorption was observed to occur in a two stage kinetic behavior with a rapid initial adsorption in contact time up to 15 minutes, followed by a second stage with a much lower adsorption rate.

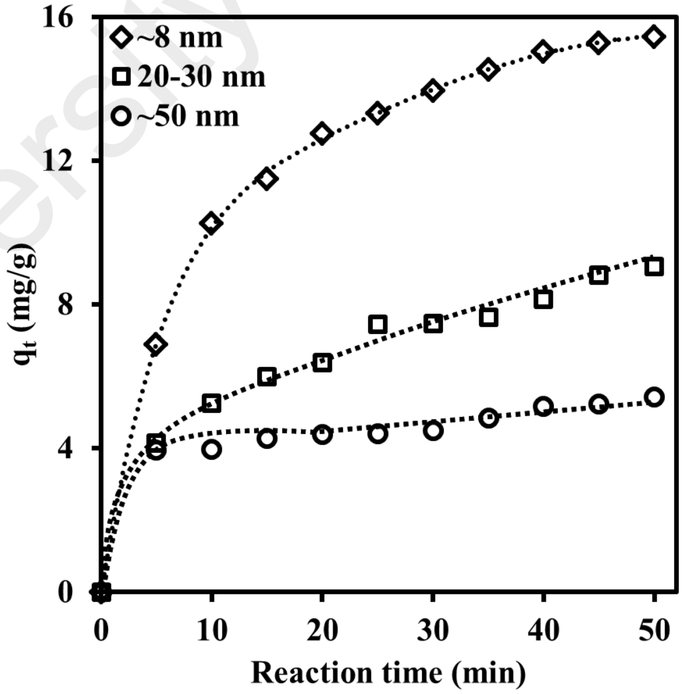

Figure 3.5: Normalized adsorbed amount of R6G by MWCNTs of different diameters as a function of time from 0 to 50 min.

This is obvious from the fact that a large number of vacant surface sites were available for the adsorption during the initial stage and with the passage of time, the remaining vacant surface sites were more difficult to be occupied due to repulsive forces between the adsorbed molecules on the MWCNTs and those in the bulk liquid phase (Anbia & Ghaffari, 2009).

Figure 3.6 shows the removal efficiency for a 10 mg/L R6G solution under stirring at 800 rpm with 8 mg and different diameters of MWCNTs from 0-50 min. The removal efficiency was calculated according to Equation 3.4. It was observed that the highest removal efficiency was obtained using MWCNTs with diameter ~8 nm. R6G solution was quickly decolorized during the 50 min with ~8 nm MWCNTs, yielding 93.4% removal efficiency, whereas for the same time, 20-30 and ~50 nm gave 54.5% and 24.1% removal efficiency, respectively. These results indicate that small diameter of MWCNTs can effectively accelerate the removal efficiency.

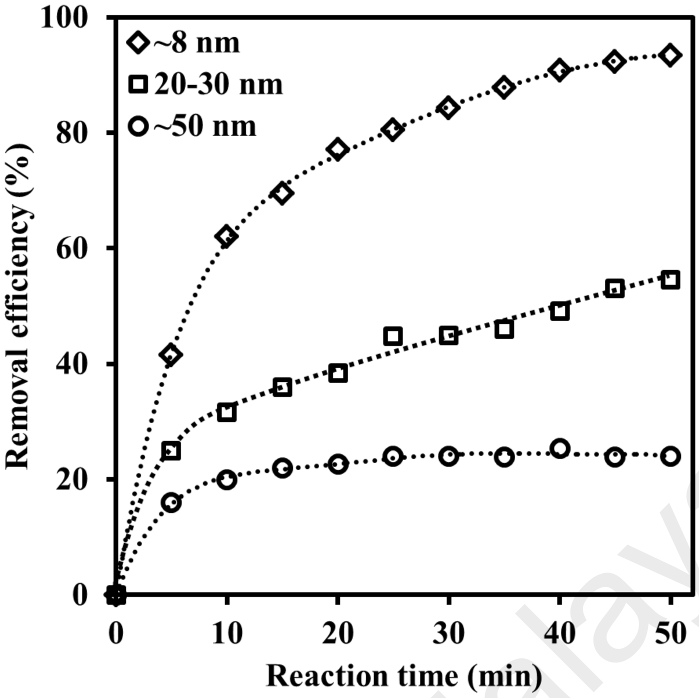

Figure 3.6: Removal efficiency of different diameters MWCNTs as a function of time.

3.4.2 Effect of MWCNTs amount on adsorption rate of R6G

To evaluate the effect of the amount of MWCNTs on the adsorption rate of R6G, a series of experiments were carried out using different amounts of MWCNTs, from 2 to 12 mg MWCNTs with same diameter as shown in Figure 3.7. The adsorbent dose is an important parameter in adsorption studies because it determines the adsorption capacity of the adsorbent to a point of equilibrium for a given initial concentration of dye solution. From Figure 3.7(a), after 50 min the R6G adsorption intensity peak was reduced into half using 2 mg MWCNTs with diameter ~8 nm. However, as shown in Figure 3.7(b)-(d) only 5 min adsorption time was required for 4, 6 and 8 mg MWCNTs with same diameter to reduce the absorbance intensity to half. Further enhancement of the reduction of absorbance intensity after 5 min time was observed with 10 and 12 mg MWCNTs which gave reduction to about 14 and 1.5%, respectively.

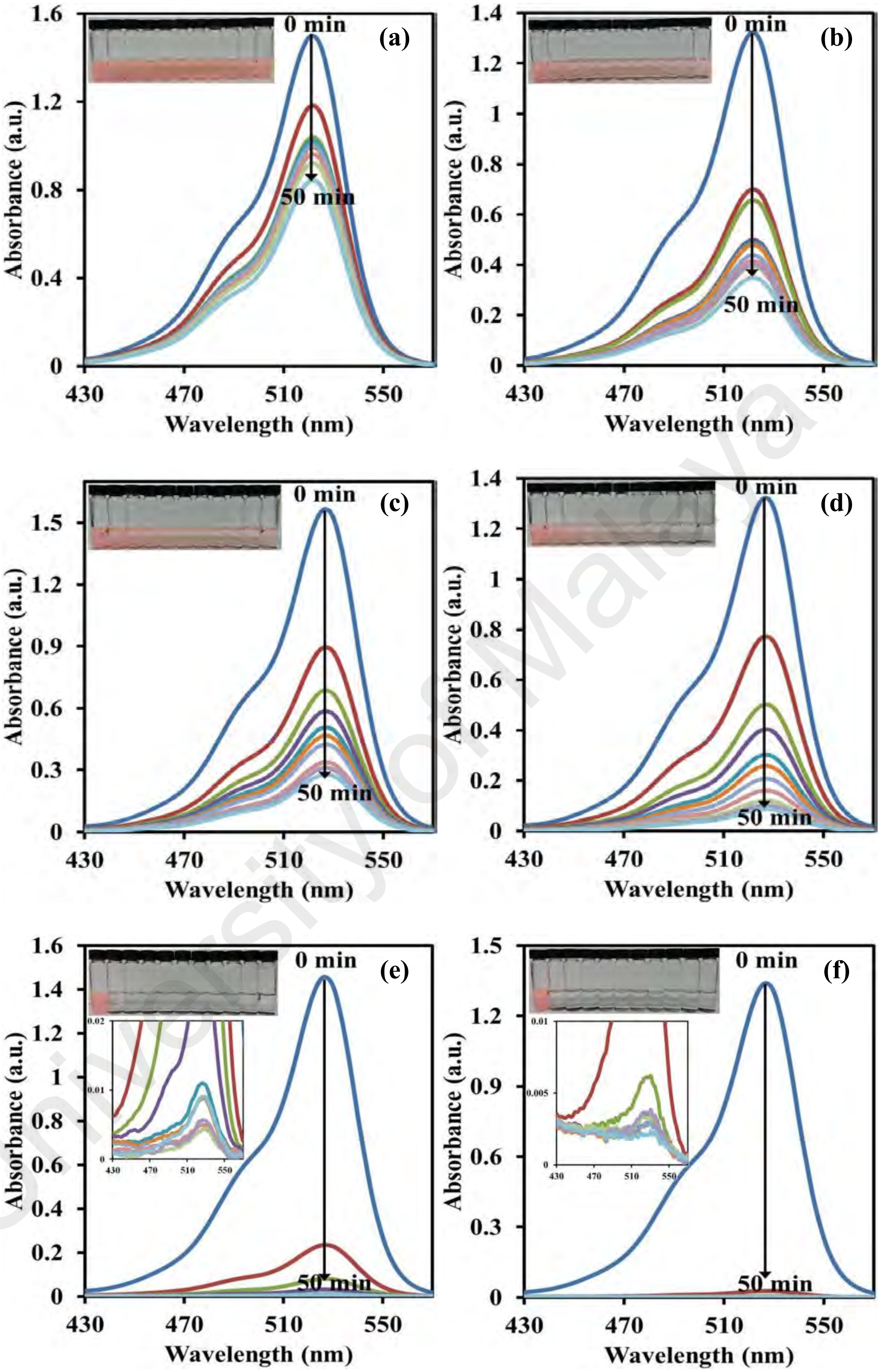

Figure 3.7: UV-vis spectra and degradation rate vs. reaction time under continuous stirring of MWCNTs ~8 nm with different amounts; (a) 2 mg, (b) 4 mg, (c) 6 mg, (d) 8 mg, (e) 10 mg and (f) 12 mg.

Figure 3.8(a) shows the adsorption capacity using different amounts of MWCNTs of diameter (~8 nm) MWCNTs in 10 mg/L R6G solution. The adsorption capacity increased with time but decreased as the MWCNTs dosage increased. Increasing the MWCNTs dose increased the probability of the MWCNTs entanglement in the solution, causing adsorption in the interlayer space and a decrease in the aggregation of R6G at the external surface. Accordingly, the adsorption capacity declined as the MWCNTs dosage increased. Moreover, the high MWCNTs dosage may influence the physical characteristics of the solid–liquid suspensions, such as by increasing the viscosity and inhibiting the diffusion of R6G molecules to the surface of the MWCNTs. Since the concentration of R6G was fixed, the adsorption capacity decreased as the MWCNTs dosage increased. The increase with MWCNTs dosage of the amount of R6G adsorbed was caused by the availability of more surface area of the MWCNTs.

For removal efficiency results for this experiment as shown in Figure 3.8(b), it was observed that the highest amounts of MWCNTs have the highest of removal efficiency. Since the value of R6G was set to 10 mg/L for all samples, the removal efficiency remained constant at one stage especially for high amount such as 10 and 12 mg. This might be due to the adsorption capacity (MWCNTs) was higher than the concentration of adsorbate itself.

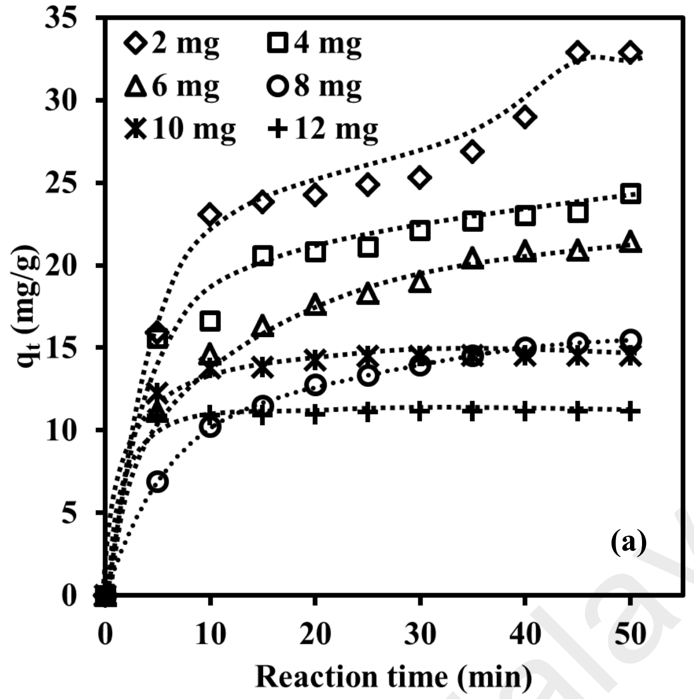

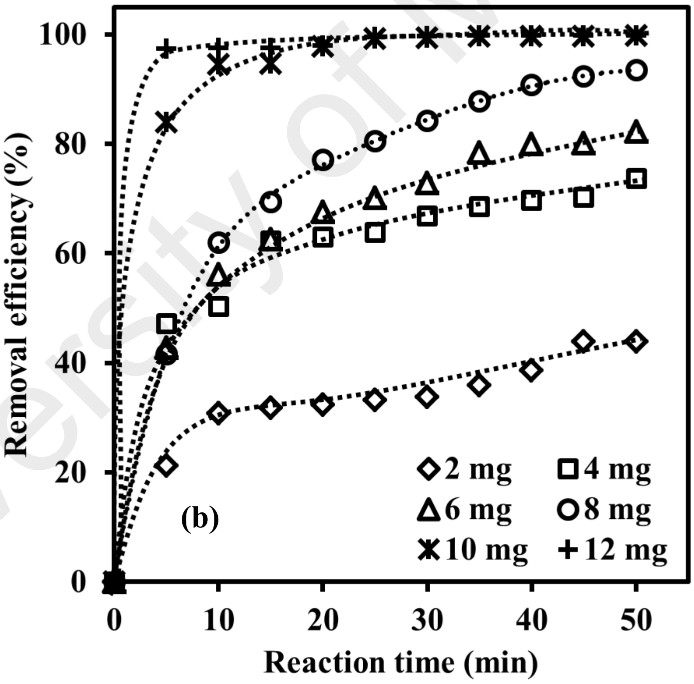

Figure 3.8: (a) Adsorbed amounts and (b) removal efficiency of MWCNTs with different amounts on R6G as a function of time.

3.4.3 Adsorption equilibrium studies

3.4.3.1 Langmuir isotherm

Figure 3.9(a)-(d) show the Langmuir isotherm plot used for adsorption equilibrium obtained from this experimental setup. Values of C_e and q_e were obtained from different amounts of MWCNTs plots as in Figure A1. For ~8 nm MWCNTs (Figure 3.9(a)), the equation $y = 0.0045x + 0.0018$ was obtained with R^2 value of 0.961. Other diameter of MWCNTs which is 20-30 nm (Figure 3.9(b)), was fitted to the equation $y = 0.0146x + 0.0046$ with R^2 value 0.974. The largest diameter of MWCNTs used (~50 nm) was plotted in Figure 3.9(c) showed the equation of $y = 0.0203x + 0.0568$ and R^2 value 0.805.

The values of maximum monolayer capacity, q_m and affinity of binding sites, k_L were computed from the slope and intercept of the Langmuir plot of $1/q_e$ versus $1/C_e$. These parameters of the Langmuir isotherm together with correlation coefficient, R^2 were listed in Table 3.2. The Langmuir isotherm fitted quite well with the experimental data (correlation coefficient, R^2>0.805) indicating this model is suitable for describing the adsorption equilibrium of R6G onto MWCNTs. This model represented monolayer adsorption of molecules on the surface of different diameters of MWCNTs.

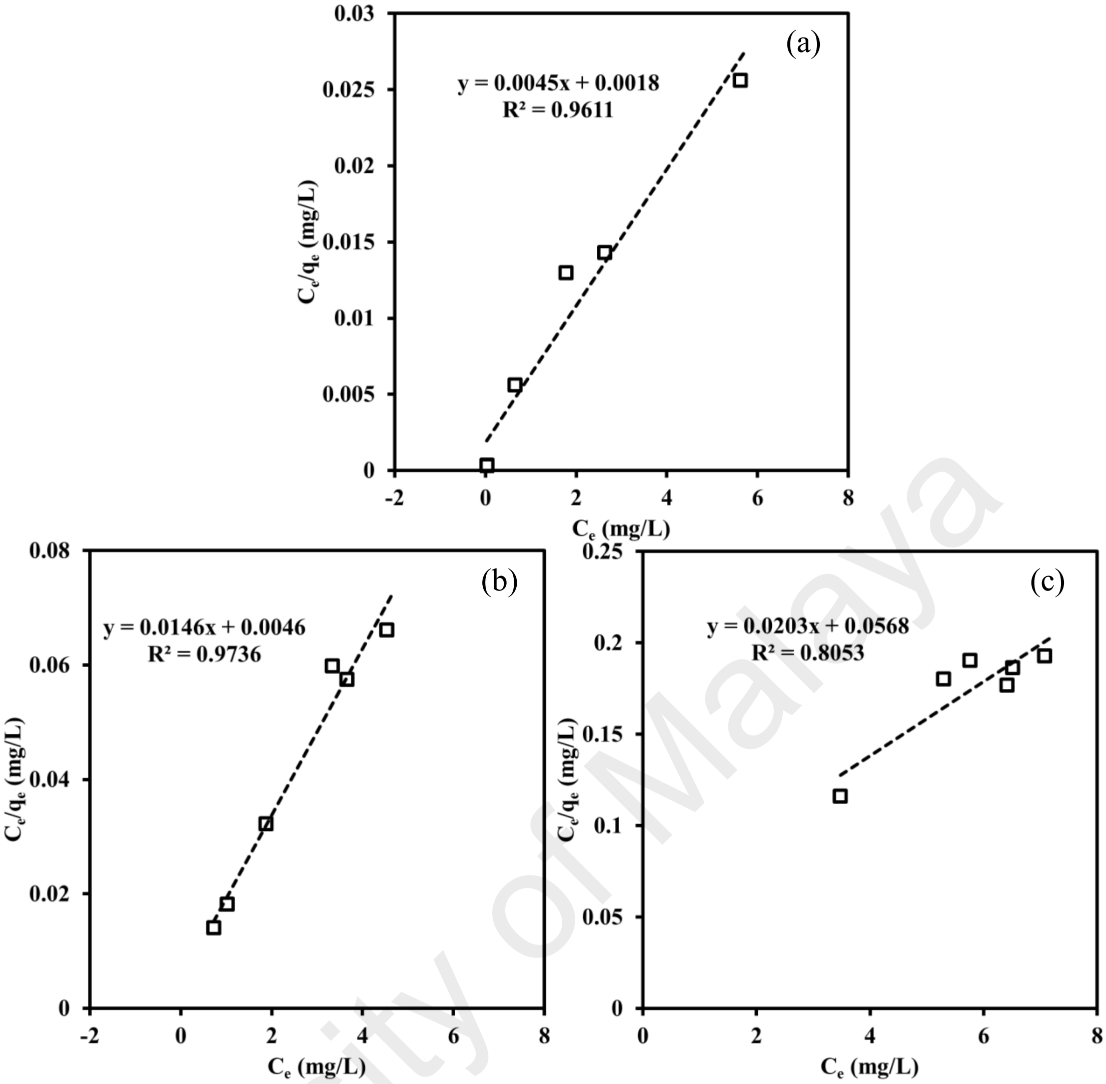

Figure 3.9: Langmuir isotherm analyses of R6G solution with different diameters MWCNTs; (a) ~8 nm, (b) 20-30 nm and (c) ~50 nm.

Table 3.2 indicates that the computed maximum monolayer capacity, q_m on the MWCNTs gave values, ranging from 222.2 to 49.3 mg/g for R6G solution. As mentioned before, q_m is a theoretical limit adsorption capacity when the monolayer surface was fully covered with adsorbate molecules to assist in the comparison of adsorption performance. Therefore it is not surprising that the highest q_m values was MWCNTs with diameter ~8 nm since it was related with the highest surface area.

The values of k_L for MWCNTs with diameters ~8, 20-30 and ~50 nm were 2.5, 3.2 and 0.4 L/mg, respectively. The k_L which indicates the affinity of binding sites to adsorbate molecules, showed little difference between MWCNTs at ~8 and 20-30 nm, but was significantly low for MWCNTs of ~50 nm diameter. This may be due to the difference in surface electronic structures of MWCNTs of different diameters due to greater number of walls and the curvature of the outer wall.

The R_L values were found to vary within a range, 0.22 to 0.02 for the initial R6G concentration values of 10 mg/L. These results are in the range of 0 to 1 which indicates this adsorption process was favorable under the conditions used in this study.

Table 3.2: Langmuir isotherm parameters for the removal of R6G solution by different diameters MWCNTs.

Langmuir constants	k_L **(L/mg)**	q_m **(mg/g)**	R^2	R_L
~8 nm	2.5	222.2	0.961	0.04
20-30 nm	3.2	68.5	0.974	0.03
~50 nm	0.4	49.3	0.805	0.22

3.4.3.2 Freundlich isotherm

The experimental equilibrium data were compared with the theoretical equilibrium data obtained from Freundlich isotherm model (Figure 3.10). For this model as plotted in Figure 3.10(a), MWCNTs with diameter ~8 nm gave a fitting equation $y = 0.1489x + 2.1661$ with R^2 = 0.854, diameter 20-30 nm (Figure 3.10(b)) yielded equation $y = 0.1111x + 1.7331$ with R^2 = 0.663 and diameter ~50 nm as plotted in Figure 3.10(c) gave $y = 0.2946x + 1.2944$ with R^2 = 0.536.

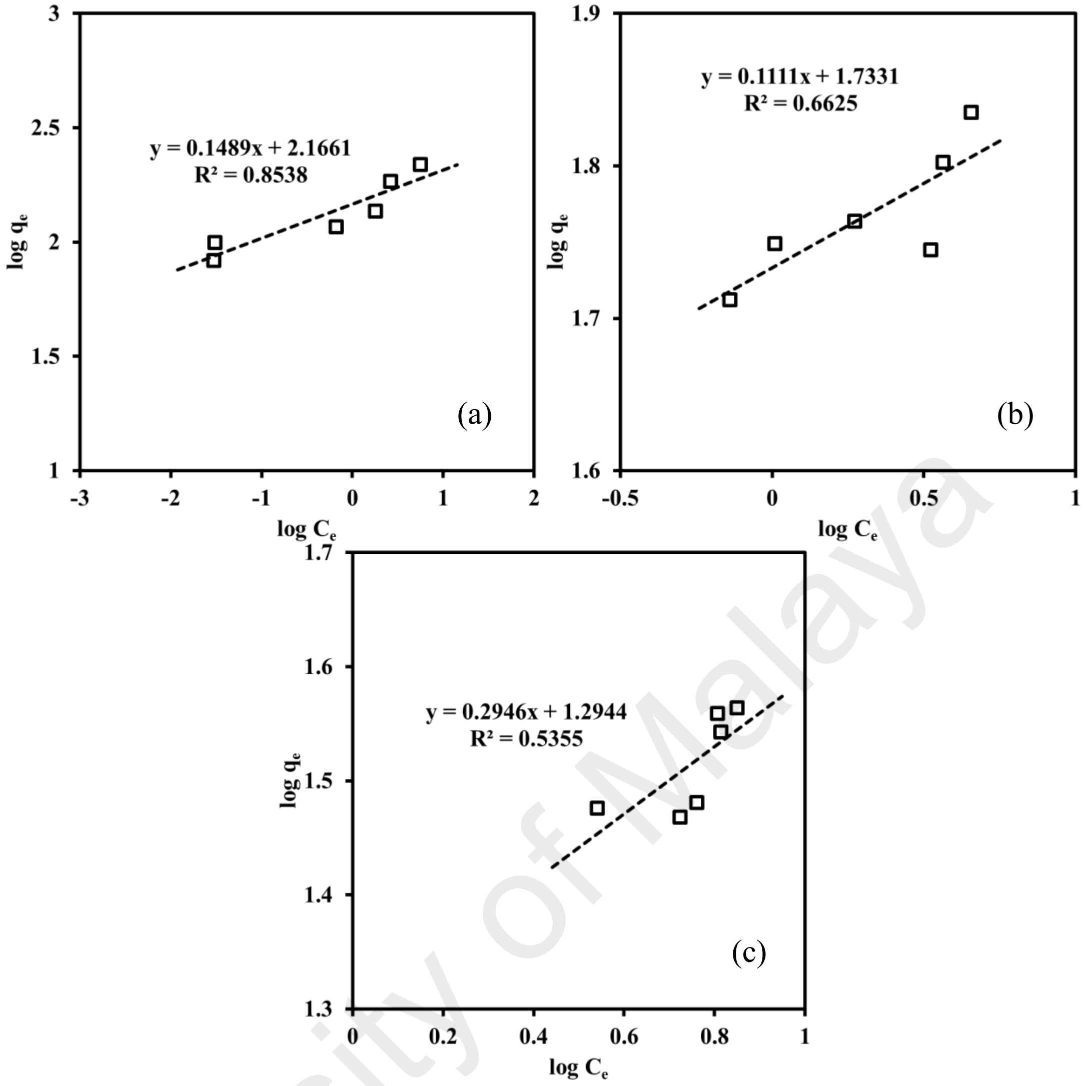

Figure 3.10: Freundlich isotherm analyses of R6G solution with different diameters MWCNTs; (a) ~8 nm, (b) 20-30 nm and (c) ~50 nm.

The values of Freundlich constants, k_F and n, were obtained from the linear fitting of the Freundlich isotherm ((2.7) and are listed in Table 3.3. Recall that the n and k_F of a linearized Freundlich model roughly represent the adsorption intensity and the adsorption capacity respectively. The adsorption intensity, n obtained was an indication of the favorability of adsorption. The n values for all different diameters were in the range $0 < n < 10$ which showed that the adsorption of R6G molecules on MWCNTs was favorable. As in the values of k_L, significantly smaller value n for MWCNTs with ~50 nm diameter was due to the difference in surface electronic structures of MWCNTs of different diameters due to greater number of walls and the curvature of the outer wall. The k_F values were in the sequence for diameters ~8 > 20-30 > ~50 nm indicating that the lowest diameter had the highest adsorption capacity which was related with specific surface area. The correlation coefficient, R^2 values of R6G for MWCNTs was below 0.854 indicating that the adsorption of R6G molecules on MWCNTs were as not well fitted using the Freundlich model.

Table 3.3: Freundlich isotherm parameters for the removal of R6G solution by MWCNTs.

Freundlich constants	**k_F (mg/g)**	***n***	**R^2**
~8 nm	146.589	6.716	0.854
20-30 nm	54.088	9.001	0.663
~50 nm	19.697	3.394	0.536

3.4.3.3 Temkin isotherm

Figure 3.11(a)-(c) showed the Temkin model plots of R6G with different diameter MWCNTs. The adsorption data were analyzed according to linear form of the Temkin model (Equation 2.10). From q_e vs $ln\ C_e$ at 27 ^{o}C, the equation were obtained as $y = 20.237x + 153.99$ (R^2 =0.784), $y = 6.5861x + 54.11$ (R^2 = 0.649) and $y = 9.6856x + 16.178$ (R^2 = 0.536) for diameter ~8, 20-30 and ~50 nm MWCNTs, respectively.

A plot of q_e versus $ln\ C_e$ (Figure 3.11) enabled the determination of the model constants k_T and B_T. The values of the parameters together with correlation coefficient (R^2) are given in Table 3.4. It can be assumed from B_T values obtained that the adsorption process of R6G on MWCNTs involved physical adsorption process. Also, it was observed that using all MWCNTs samples poor agreement of fitting Temkin model with the experimental data where R^2<0.784 were obtained.

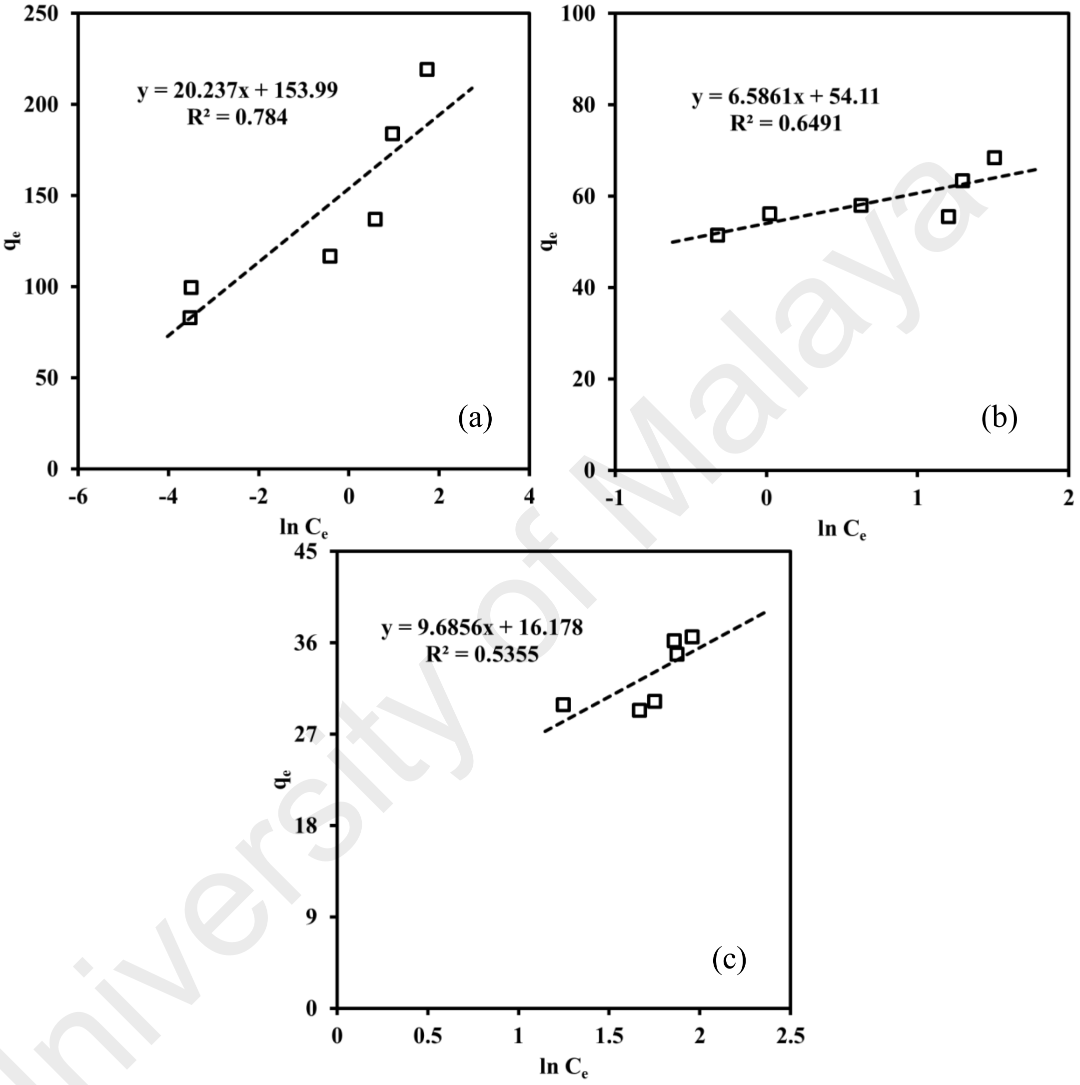

Figure 3.11: Temkin isotherm analyses of R6G solution with different diameters MWCNTs; (a) ~8 nm, (b) 20-30 nm and (c) ~50 nm.

Table 3.4: Temkin isotherm parameters for the removal of R6G solution by MWCNTs.

Temkin constants	k_T **(L/mg)**	B_T **(J/mol)**	R^2
~8 nm	2017	20.237	0.784
20-30 nm	3699	6.586	0.649
~50 nm	5	9.686	0.536

3.4.4 Adsorption equilibrium discussion

It was observed that the adsorption behavior of R6G on MWCNTs was modeled well with the Langmuir model with the highest R^2 were obtained compared to the other two models under the concentration range studied. It can be concluded that:

1) The adsorption of R6G towards MWCNTs was monolayer adsorption (the adsorbed layer is one molecule thick);
2) Once a R6G molecule occupies a site, no further adsorption can take place at that site;
3) All sites are energetically equivalent;
4) There is no interaction between R6G molecules which adsorbed towards another in the neighboring sites;
5) At equilibrium, MWCNTs has a finite capacity for R6G molecules adsorption (a saturation point is reached where no further adsorption can occur);

The adsorption of R6G on MWCNTs can be classified as favorable since the values for R_L and n obtained from Langmuir and Freundlich model, respectively were in the range of favorable adsorption. Maximum monolayer capacity, q_m (from Langmuir model) and adsorption capacity, k_F showed that MWCNTs with high specific surface area (small diameter) were found to be better compared to low specific surface area (high diameter) MWCNTs.

3.4.5 Adsorption kinetics

To study the adsorption kinetics of R6G on different amounts MWCNTs, 10 mg/L initial concentration of R6G solution was used. The transient behavior of the R6G adsorption process was analyzed by using different kinetic models which were pseudo-first-order, pseudo-second-order and intraparticle diffusion models.

3.4.5.1 Pseudo-first-order

Figure 3.12 is the pseudo-first-order kinetic plots for the adsorption of R6G on MWCNTs calculated using Equation 2.12. The intercept and slope of this plot gave values for $ln\ q_e$ (log of the equilibrium adsorption capacity) and k_1 (pseudo-first-order rate constant), respectively. The values of k_1, q_e (experimental and calculation) and correlation coefficients (R^2) for different amounts MWCNTs used are presented in Table 3.5. The values of the rate constants, k_1 were found to increase from 0.094 to 0.453 (min^{-1}) with increase in the MWCNTs dose from 2 to 12 mg. The equilibrium adsorption capacity, q_e decreased with increasing MWCNTs amount due to less number of R6G molecules adsorbed at the available adsorption sites.

The correlation coefficients for the pseudo-first-order model changed in the range of 0.846 to 0.973. However, if the value of the intercept is not equal to q_e based on Equation 3.3, the interaction would not likely to be first order even though this plot has high correlation coefficient (R^2) with the experimental data. From the experimental q_e values ($q_{e,exp}$) and calculated values ($q_{e,cal}$) obtained from the linear plots, it obtained that the kinetics of R6G adsorption on different amounts of MWCNTs did not follow the pseudo-first-order kinetic model.

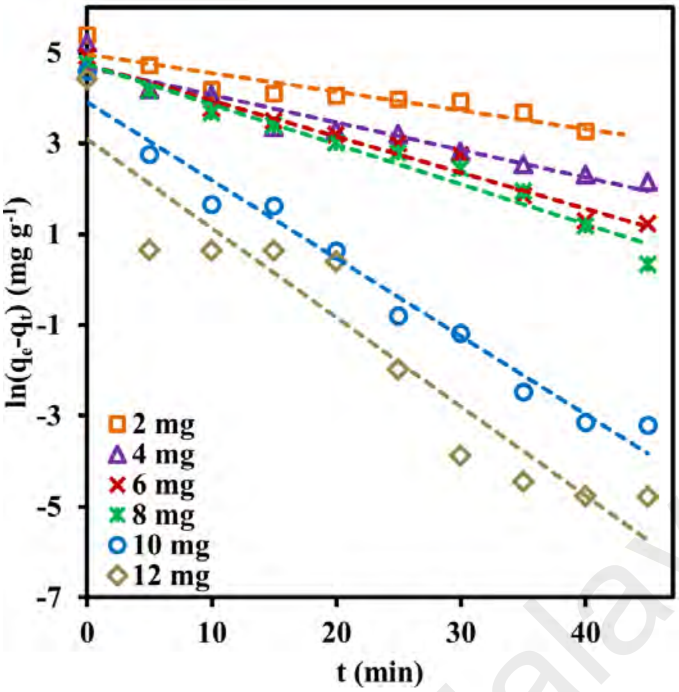

Figure 3.12: Pseudo-first-order kinetics plots for the adsorption of R6G onto MWCNTs at different amounts.

Table 3.5: Coefficients pseudo-first-order adsorption kinetic models for different amounts MWCNTs.

Pseudo-first-order model	$q_{e,exp}$ (mg/g)	k_1 (min^{-1})	$q_{e,cal}$ (mg/g)	R^2
2 mg	219	0.094	143	0.846
4 mg	184	0.140	108	0.929
6 mg	137	0.183	116	0.971
8 mg	117	0.202	115	0.970
10 mg	100	0.397	51	0.973
12 mg	83	0.453	22	0.904

3.4.5.2 Pseudo-second-order

Figure 3.13 displays the linear regressions of pseudo-second-order plot for different amounts of MWCNTs and all parameters obtained are listed in Table 3.6. Value of equilibrium adsorption capacity as calculated from this model is using equation:

$$q_{e,cal} = \frac{1}{slope} \tag{3.5}$$

where the slope is from the pseudo-second-order plot. While the value of equilibrium adsorption capacity experiment ($q_{e,exp}$) was obtained using Equation 3.3. It was observed that the value of equilibrium adsorption capacity between experimental ($q_{e,exp}$) and calculated ($q_{e,cal}$) were in good agreement with each other. Furthermore, the plots of t/q_t versus t showed linearity with correlation coefficients, R^2 greater than 0.959 as listed in Table 3.6. As a result, it can be suggested that the pseudo-second-order kinetic equation was the better kinetic expression to represent the R6G uptake by different amounts of MWCNTs.

The values of the rate constants, k_2 were found to increase from 0.001 to 0.06 (g/mg min) with increasing MWCNTs dose from 2 to 12 mg. The pseudo-second-order kinetic analysis revealed that the values of the initial adsorption rates, h increased with increasing MWCNTs amount. The higher amount of MWCNTs means the higher adsorption sites which caused the lower the probability of R6G adsorption and hence the faster R6G molecules could be bonded to the active sites on the surface of the MWCNTs (Kumar & Kirthika, 2009).

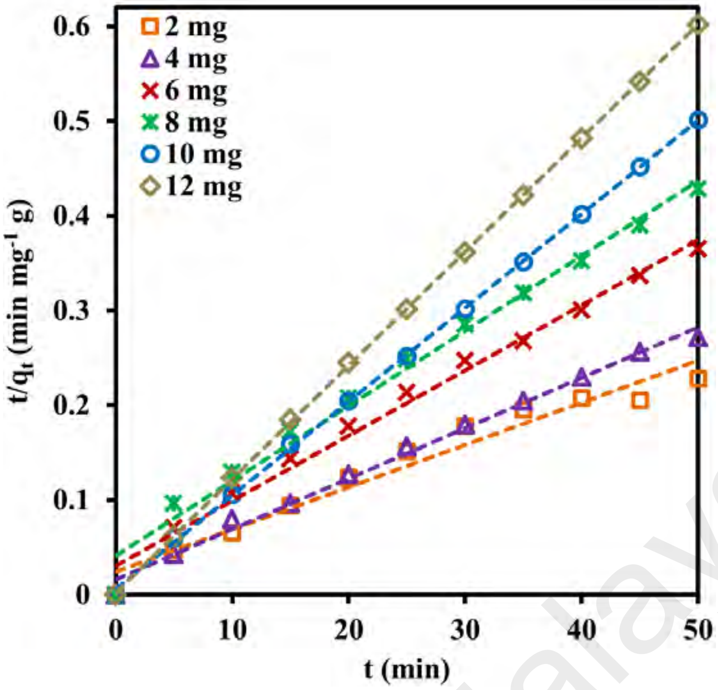

Figure 3.13: Regressions of kinetic plots at different amounts of MWCNTs pseudo-second-order model R6G solution adsorption.

Table 3.6: Coefficients pseudo-second-order adsorption kinetic models for different amounts MWCNTs.

Pseudo-second-order	$q_{e,exp}$ **(mg/g)**	k_2 **(g/mg min)**	h **(mg/g min)**	$q_{e,cal}$ **(mg/g)**	R^2
2 mg	219	0.001	24.4	222	0.959
4 mg	184	0.002	32.8	189	0.993
6 mg	137	0.002	41.1	145	0.988
8 mg	117	0.002	62.1	127	0.986
10 mg	100	0.016	166.7	101	1.000
12 mg	83	0.060	416.7	83	1.000

3.4.6 Intraparticle diffusion

There are different stages involving the adsorption process on porous adsorbents which are:

1) Bulk diffusion;
2) Film diffusion;
3) Intraparticle diffusion;
4) Adsorption of the solute onto surface.

Generally for bulk and film diffusion are assumed to be rapid thus there will be no rate determining factor. Since both models for adsorption kinetic (pseudo-first-order and pseudo-second-order) cannot identified the diffusion mechanism, the intraparticle diffusion model was used to explained the diffusion mechanism.

According to Weber and Morris if the rate limiting step is intraparticle diffusion, a plot of adsorbate adsorption against the square root of the contact time should yield a straight line passing through the origin (Weber & Morris, 1963). The plots obtained in Figure 3.14 were related by two straight lines for low amount of MWCNTs (2-8 mg) and 3 straight lines for high amount of MWCNTs (10 and 12 mg). The first straight line depicted the adsorption on the external surface which occurred almost instantaneously. The second portion indicated a comparatively slower adsorption process when the adsorbate diffused gradually into the interior surfaces of the particles and the adsorption becomes intraparticle diffusion controlled (Wu et al., 2000). The third portion could also be distinguished as the final equilibrium stage when the intraparticle diffusion started to slow down due to saturation of adsorption sites. The deviation of the straight lines from the origin may be due to the difference in the rate of mass transfer in the initial and final stages of adsorption (Panday et al., 1986).

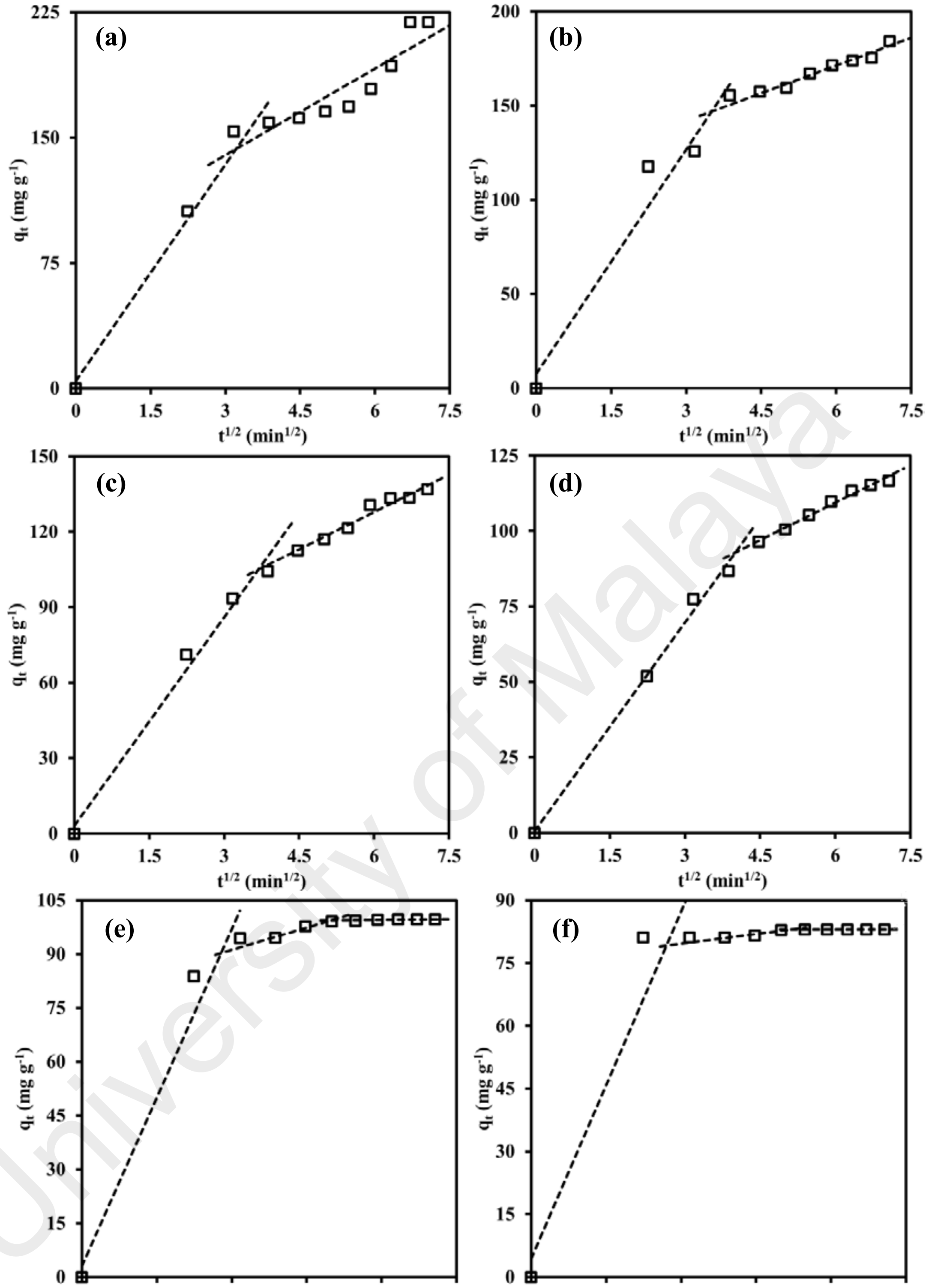

Figure 3.14: Regressions of intraparticle diffusion models at different amounts of MWCNTs; (a) 2 mg, (b) 4 mg, (c) 6 mg, (d) 8 mg, (e) 10 mg and (f) 12 mg.

Table 3.7 summarized the coefficients of intraparticle diffusion model for every curve in Figure 3.14. The k_i value was higher at the lower amount of MWCNTs. It is seen that the order of adsorption rates was first stage (k_{i1})> second stage (k_{i2})> third stage (k_{i3}). At the beginning, the R6G was adsorbed by the exterior surface of MWCNTs, so the adsorption rate was very high. When the exterior surface reached saturation, the R6G entered into MWCNTs by the pore within the CNTs and were adsorbed by the interior surface of the CNTs. When the R6G diffused in the pore of MWCNTs, the diffusion resistance increased, which caused the diffusion rate to decrease. With the decrease of the R6G concentration in the solution, the diffusion rate became lower and lower, and the diffusion processes reached the final equilibrium stage. Therefore the changes of k_{i1}, k_{i2} and k_{i3} could be attributed to the adsorption stages of the exterior surface, interior surface, and equilibrium, respectively (Rengaraj et al., 2004).

Table 3.7: Coefficients of intraparticle diffusion parameters obtained with different ~8 nm MWCNTs loading.

MWCNTs loading	k_{i1} (mg/g min$^{0.5}$)	k_{i2} (mg/g min$^{0.5}$)	k_{i3} (mg/g min$^{0.5}$)	R^2
2 mg	43.3	20.5	-	0.8492
4 mg	39.8	9.8	-	0.9606
6 mg	27.6	9.9	-	0.9541
8 mg	23.1	8.3	-	0.9836
10 mg	31.3	4.1	0.17	0.9694
12 mg	27.6	1.5	0.01	0.8834

3.4.7 Adsorption kinetics discussion

For the pseudo-first-order model, it was observed that the large differences between experimental ($q_{e,exp}$) and calculated ($q_{e,cal}$) values of the equilibrium adsorption capacity, indicating that the adsorption of R6G on the MWCNTs did not obey the pseudo-first-order model. In contrast, the pseudo-second-order model showed a good fit with experimental data. The values of $q_{e,cal}$ also appeared to be close to the experimentally observed values of $q_{e,exp}$. These results suggested that the adsorption kinetic followed the pseudo-second-order model.

If the initial concentration of solute (C_o) is high, adsorption kinetics better fitted the pseudo-first-order model, while for values of C_o that are not too high, the fit of adsorption to the pseudo-second-order kinetics was better (Azizian, 2004). The concentration of R6G (10 mg/L) used in this experiment setup was not too high and the rate constant is a complex function of initial concentration of R6G.

For intraparticle diffusion, the regression was linear, but the plot did not pass through the origin (Figure 3.14), suggesting that adsorption involved intraparticle diffusion, but that was not the only rate-controlling step.

3.4.8 Raman analysis

Figure 3.15 show Raman spectra for MWCNTs before and after adsorption with R6G solution. It was observed that for MWCNTs there were two peaks. The first was the ‘‘defect’’ mode (*D*) at about 1342 cm^{-1}, induced by sp^3 electronic states (considered to be defects in the planar sp^2 graphitic structure) (Machado et al., 2012). The second peak was at 1571 cm^{-1} known as the G band, which was related to the graphite E_{2g}

symmetry of the interlayer mode. This mode reflected the structural integrity of *sp*^{2}-hybridised carbon atoms of the nanotubes.

Through introduction of R6G solution, several new peaks corresponding to R6G existed together with MWCNTs peaks as listed in Table 3.8. These peaks located at 612 cm^{-1}, 773 cm^{-1}, 1184 cm^{-1} and 1309 cm^{-1}, were known as C-C-C ring in-plane bending, C-H out-of-plane bending, C-H in-plane bending and in plane xanthene ring, respectively. For peaks located at 1506 cm^{-1} and 1647 cm^{-1} both of them corresponded to aromatic C-C stretching.

The Raman spectra of the MWCNTs loaded with R6G dye showed a shift in position of *D* band to 1359 cm^{-1} but *G* band was unchanged but the intensity was reduced in relation to the *D* band. The interaction between R6G molecules and surface of adsorbent can induce the shift of the characteristic MWCNTs bands to higher of Raman shift values due to the increase in the elastic constant of the harmonic oscillator of MWCNTs (Mishra et al., 2010). The van der Waals attraction between the dye and the graphene sheets of MWCNTs may increase the energy needed for vibrations, which was reflected in the higher frequency of Raman peaks (Mishra et al., 2010). Moreover, Hildebrandt and Stockburger studied the stretching of C-O-C of R6G molecules reported strong Raman band at 1363 cm^{-1}, therefore the interaction between this band with the *D* band of MWCNTs resulted in the strong peak at 1359 cm^{-1} (Hildebrandt & Stockburger, 1984).

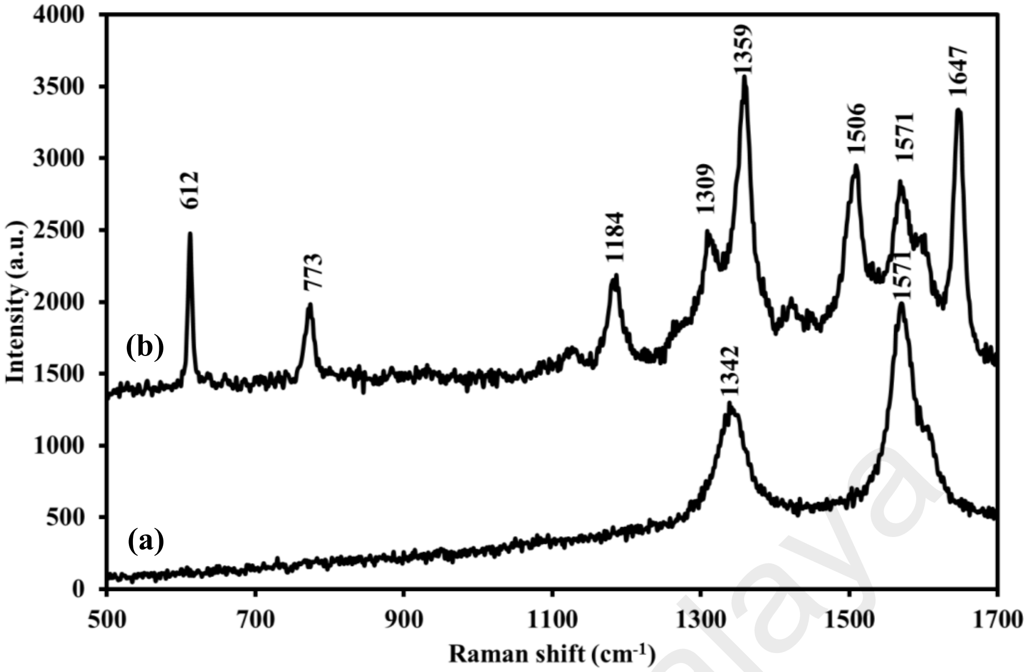

Figure 3.15: Raman spectra of (a) MWCNTs and (b) MWCNTs after adsorption with R6G solution.

Table 3.8: Experimental Raman shifts and assignment of selected band of R6G.

Raman shift (cm^{-1})	Assignment	Reference
612	C-C-C ring in-plane bending	(Habouti et al., 2011; Hildebrandt & Stockburger, 1984)
773	C-H out-of-plane bending	(Habouti et al., 2011; Hildebrandt & Stockburger, 1984)
1184	C-H in-plane bending	(Hildebrandt & Stockburger, 1984)
1309	In plane xanthene ring breath	(Jensen & Schatz, 2006)
1359	C-O-C stretching	(Hildebrandt & Stockburger, 1984)
1506	Aromatic C-C stretching	(Hildebrandt & Stockburger, 1984)
1647	Aromatic C-C stretching	(Hildebrandt & Stockburger, 1984)

CHAPTER 4: PURE AND ZNO DECORATED MWCNTS AS ETHANOL AND TOLUENE VAPOUR SENSORS

Commercial volatile organic compound (VOC) sensors available in the market are based on metal oxides. Some examples are listed in Table 4.1. The gas responses of the NiO nanoflowers were investigated towards 100 ppm of a variety of gases including H_2, NO_2, CO, toluene, NH_3 and H_2S at 150 °C (Wu et al., 2012). It was reported that NiO nanoflowers were excellent for NO_2 sensing materials owing to their excellent response and selectivity.

A microwave-assisted hydrothermal method have been used to produce CuO nanorods with the diameter of 15–20 nm and the length of 60–80 nm by Yang and co-workers (Yang et al., 2011). They discovered that response of the CuO sensor to 1000 ppm of ethanol was 9.8 at the operating temperature of 210 ^{o}C and the response time and the recovery time were within the range of 13–42 s and 17–51 s, respectively. They also investigated other target gases such as ethyl-acetate, acetone, xylene, toluene and cyclo-hexane and found that higher response compared to ethanol gas.

Co_3O_4 mesocrystals with concave octahedral structures were successfully prepared by a facile, polymer-mediated route (Liu et al., 2012). It was found that they show high sensitivity and good response and recovery characteristics for formaldehyde and ethanol for working temperature at 200 ^{o}C. As compared with Co_3O_4 powder, Co_3O_4 mesocrystals exhibit 1.8-fold and 1.4-fold enhancement in gas responses to 100 ppm of formaldehyde and ethanol, respectively.

The sensing response of pure Cr_2O_3 and Cr_2O_3 activated SnO_2 to ethanol vapor has been investigated (Singh et al., 2010). They found that response to ethanol vapor significantly improved with the addition of SnO_2 but the operating temperature (300 ^oC) remained the same.

Ag@α-Fe_2O_3 core–shell nanoparticles were synthesized using a simple two step chemical route (Ag nanoparticles synthesis by sodium borohydride as the reducing agent in a first step and the subsequent mixing with a Fe^{3+} sol for α-Fe_2O_3 coating) (Mirzaei et al., 2015). They developed sensor that can detect ethanol at concentrations as 100 ppm at 250 °C with response and recovery time 5.5 and 16 s, respectively.

Table 4.1: Various metal oxide VOC sensor reported by other researchers.

Metal oxide	**VOC**	**Sensing Temperature (^{o}C)**	**VOC concentration (ppm)**	**Response time (s) /Recovery time (s)**	**References**
NiO	Ethanol	150	100	-	(Wu et al., 2012)
CuO	Ethanol	160-300	5-1000	13-42/17-51	(Yang et al., 2011)
CO_3O_4	CH_2O	200	100-1000	-	(Liu et al., 2012)
Cr_2O_3	Ethanol	300	250	~39/~50	(Singh et al., 2010)
Ag@ Fe_2O_3	Ethanol	250	100	5.5/16	(Mirzaei et al., 2015)

Although metal oxide based sensors have good performance, they require high operating temperatures and exhibit poor chemical selectivity (Tasaltin & Basarir, 2014). Another disadvantage of this type of sensing materials is that they required post treatments such as calcination and annealing (Jimenez-Cadena et al., 2007). In a way to overcome this problem, novel nanomaterial are sought to provide better solution over conventional metal oxide. Nanomaterials are ideal for gas molecule adsorption and storage since it have very large surface to volume ratio and void structure. Thus, nanomaterials such as carbon nanotubes (CNTs) have been widely studied as gas sensors based materials (Izadi et al., 2012; Kim, 2006; Sayago et al., 2008). Multiwalled carbon nanotubes (MWCNTs) based gas sensors have attracted great interest due to their high surface area volume ratio, high electron mobility and high potential of gas adsorption (Tasaltin & Basarir, 2014).

MWCNTs based ammonia sensor by dielectrophoresis on a microelectrode array has been fabricated (Suehiro et al., 2003). They discovered sensor for ammonia by MWCNTs could quantitatively and reversibly detect ppm-level ammonia gas by the conductance decrease at room temperature.

CNTs based NO_x gas sensors which were fabricated on Al_2O_3 substrates with interdigitated Pt-electrodes and operating at ambient temperature were reported (Ueda et al., 2008). Resistance of samples reduced with increasing of concentration of NO or NO_2 gas. They also found that the used of ultraviolet light irradiation as a method to remove the adsorbed gas molecule at room temperature.

In this chapter, a study on the effect of diameter of pure MWCNTs on the sensing efficiency of ethanol and toluene vapours is presented. Also, the effect of ZnO decorated MWCNTs of ~50 nm diameter compared to pure MWCNTs will be reported. The behavior of each diameter as sensor vapor will be related with adsorption behavior as discussed on Chapter 3.

4.1 Preparation of pure MWCNTs and ZnO decorated MWCNTs sensors

MWCNTs used in this experimental were as described in Table 3.1. A good dispersion of MWCNTs in water can be accomplished by physical adsorption of SDS. Hydrophilic parts of surfactants interact with water while the hydrophobic parts are adsorbed into MWCNTs surface. It was predicted, the alkyl chain of SDS molecules attaches along the outer surface of pristine MWCNTs as shown in Figure 4.1. Electrostatic repulsion produced by the existence of $–SO_3^-$ ions assisted to stabilize the suspension and generate a lot of negative functional groups around MWCNTs surfaces.

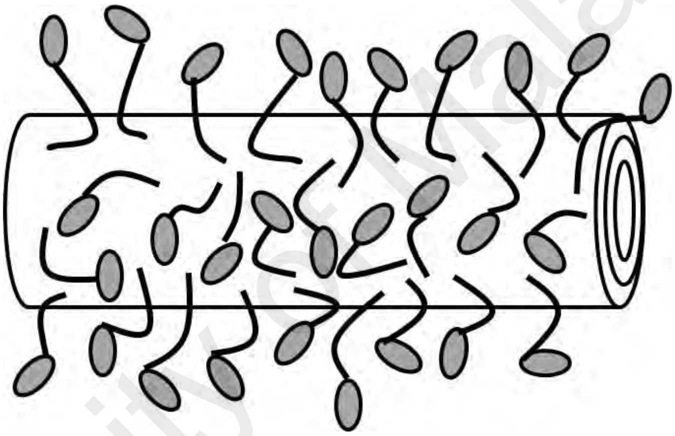

Figure 4.1: Adsorption of SDS molecules on MWCNTs (Ellipsoids shape are representing the hydrophilic groups and black lines are hydrophobic group).

Typically 1 g SDS dissolved in deionized water was used as the dispersion solution. 50 mg MWCNTs was added to 100 ml SDS solution and sonicated for 4 hours resulting in a dispersed suspension of MWCNTs which was stable for months.

To fabricate the sensor, 10 µl dispersed MWCNTs suspensions were dropped on printing paper with dimension of 0.5 cm x 1.0 cm. After drying at 100 ^oC for 1 h conductive silver paint was applied at the edge as electrodes for the sensor as shown in

Figure 4.2. The sensor was then glued on top of glass slide in order to form a good standing sensor.

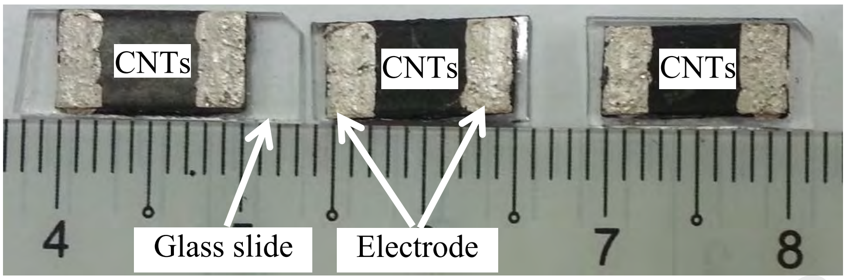

Figure 4.2: MWCNTs on printing paper as VOC sensor.

MWCNTs with diameter ~50 nm was chosen because it has a large outer diameter compared to others to be decorated with ZnO. The synthesis process of ZnO decorated MWCNTs nanocomposites comprised of two steps. 50 mg MWCNTs was added to 1 wt. % SDS solution and dispersed ultrasonically. Then, NaOH was added into the solution to facilitate abundance of OH^- ions for formation of ZnO. In the second step, $Zn(NO_3)_2.6H_2O$ of weight 4.55, 9.10, 13.65, 18.20, or 22.75 mg which was equivalent to 0.37, 0.73, 1.10, 1.47, or 1.84 mol % Zn with respect to C was added to the suspension containing 50 mg dispersed MWCNTs and was stirred at 95 ^oC for 3 h. After that, the solution was stirred at room temperature for about 24 h. Zn decorated MWCNTs were obtained after centrifuging and thoroughly washed with deionized water. The ZnO decorated MWCNTs were calcined at 300 ^oC for 1 h.

4.2 Analysis of Pure MWCNTs and ZnO NPs Decorated MWCNTs

4.2.1 Sensor characterization

All the samples used in this experiment which were pure MWCNTs and ZnO decorated MWCNTs were analyzed by Energy Dispersive X-ray Spectroscopy (EDX), Field Emission Scanning Electron Microscopy (FESEM), Thermogravimetric Analysis (TGA), X-ray Diffraction (XRD), Raman spectroscopy and (High Resolution Transmission Electron Microscopy) HRTEM..

For EDX samples preparation, a few drop of sensor suspension was cast on silicon wafer. An acceleration voltage of 15 kV was applied and each spectrum collected with acquisition time of 30 s during the calibration process. The measuring spots were randomly selected from surface of the sample.

For FESEM analysis, preparation sample was done differently between the pure MWCNTs and ZnO decorated MWCNTs samples. In order to understand the distribution of MWCNTs on printing paper, the sample was prepared like sample for vapor sensor (suspension dropped on printing paper). To achieve better morphology image of ZnO decorated MWCNTs, silicon wafer was used as a substrate instead of printing paper since silicon wafer is more conducting compared to printing paper.

TGA test was carried out in nitrogen with a heating rate of 50 ^{o}C/min. TGA is to evaluate the thermal stability of material and analyzed the purity of samples. There were three parameters measured in the TGA which were the initiation temperature, oxidation temperature and residual mass as shown in Figure 4.3. The temperature when the material starts to decompose was defined as an initiation temperature while the oxidation temperature is defined as the thermal stability temperature of the material or peak in the derivative thermal analysis (DTA) as a function of temperature. The residual mass is the mass remaining after the decomposition process.

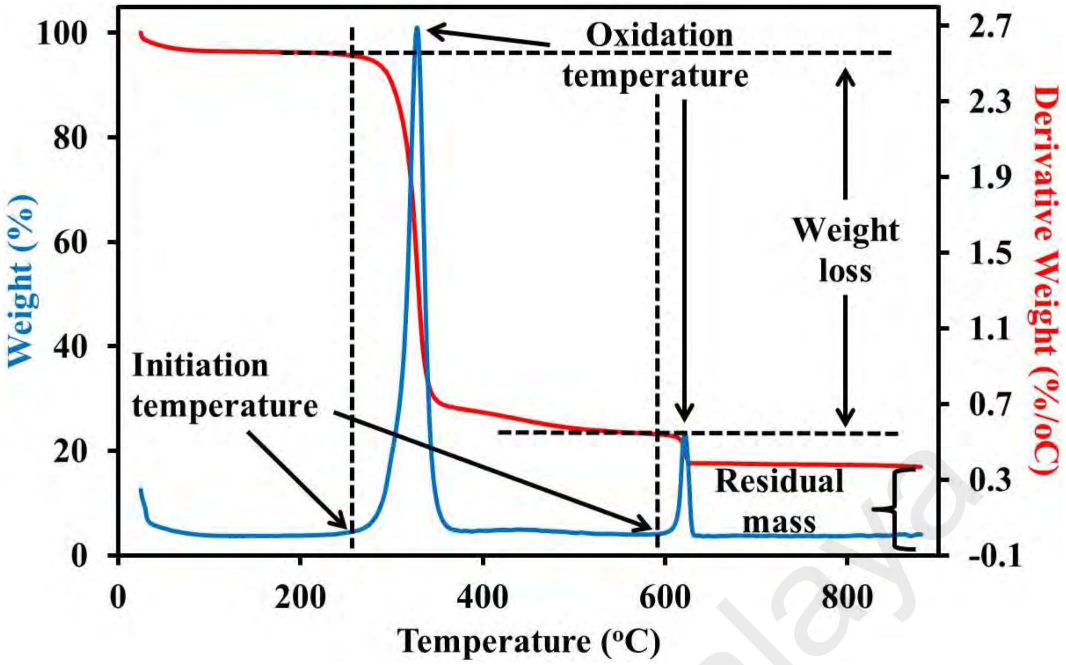

Figure 4.3: TGA and DTA as a function of temperature.

For XRD samples preparation, powder form of the MWCNTs was used in the characterization. The sample was stacked on the microscope slide and placed in the sample holder. Monochromatic beam, CuK_{α} with radiation wavelength of 1.5406 Å was used and the sample was rotated in the range of 2θ between 5^{o} to 80^{o} with a scanning rate of 0.013^{o}.

The similar samples preparation as XRD was used for Raman spectroscopy analysis. These measurements were carried with laser excitation wavelength 532 nm.

HRTEM sample was prepared by diluting one drop of the sensor suspension onto isopropanol solution and cast it onto copper grid. The measurement was done with an accelerating voltage of 120 kV.

4.2.2 Sensing Set up

The fabricated samples were then tested for ethanol or toluene vapors exposure in a closed stainless steel chamber as shown in Figure 4.4. The chamber volume was approximately 11.4 L. The sensing sample was placed in the center of the chamber. Air was pump in into the chamber to stabilize the electrical resistance for 40 s. VOC was injected into the chamber by using the micropipette. To monitor constant pressure, a vacuum gauge was used. The concentration of VOC on the sensor can be estimated from these relations:

$$n_a = \frac{PV_c}{RT} \tag{4.1}$$

where n_a is numbers of moles of air, P is pressure inside the chamber, V_c is volume of chamber, R is the universal gas constant (8.31 x 10^{-5} m^3Bar K^{-1} mol^{-1}) and T is the absolute temperature (300 K).

$$n_{voc} = \frac{m_{voc}}{m_w} \tag{4.2}$$

$$m_{voc} = \rho_{voc} V_{voc} \tag{4.3}$$

Substitute Equation 4.3 into Equation 4.2:

$$n_{voc} = \frac{\rho_{voc} V_{voc}}{m_w} \tag{4.4}$$

where n_{voc} is the VOC numbers of moles, m_{voc} is the VOC mass, ρ_{voc} is the VOC density, V_{voc} is the volume of the VOC injected and m_w is the molecular weight of VOC injected.

Concentration of VOC in part per million:

$$C_{ppm} = \frac{n_{voc}}{n_a} \times 10^6 \tag{4.5}$$

Substitute Equation 4.1 and 4.4 into Equation 4.5:

$$C_{ppm} = \frac{\rho_{voc} V_{voc} RT}{m_{voc} P V_C} \times 10^6 \tag{4.6}$$

With typical pressure P of 0.96 Bar, the volume of the VOC injected into the chamber was between 20 to 200 µL with an interval of 20 µL giving equivalent concentrations of 780 to 7803 ppm for ethanol and 425 to 4253 ppm for toluene.

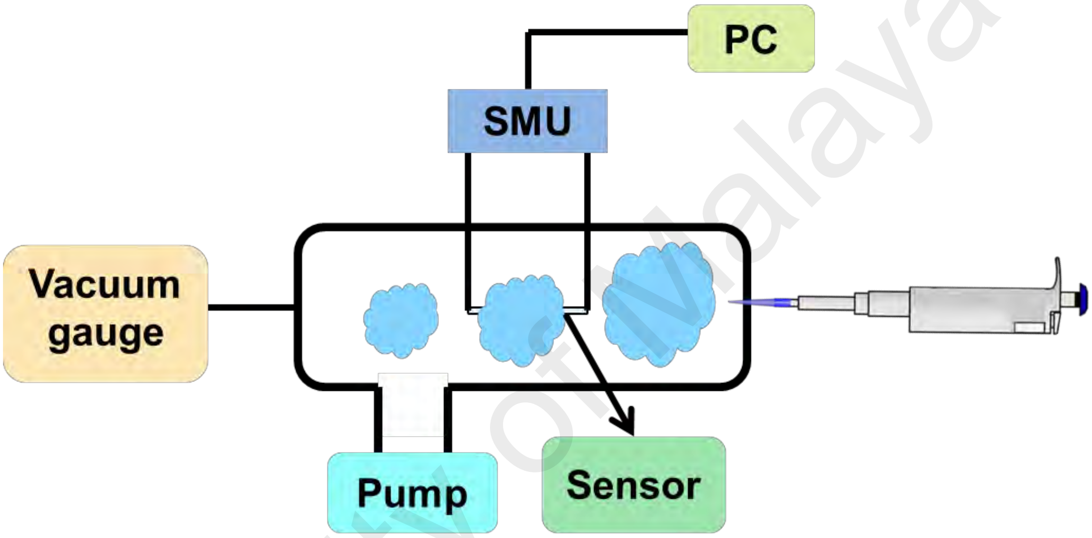

Figure 4.4: Schematic diagram of the test setup used for sensor characterization.

In a typical measurement, the voltage of source measuring unit (SMU) was set to 6 V and current through the sensor was measured. The electrical response was monitored in the form of changes in current vs times as shown in Figure 4.5(a). The SMU was connected to a computer and data acquisition was facilitated by a software. The time variation of current through the sensor was recorded in current (I) vs times (t) over period of 650 s. VOC liquid was injected every 60 s, each time at an increased volume. Current response was almost immediate and typically lasted for ~30 s. Different current peaks denoted the sensor response in the form reduced in current flow which resulted from increase in resistance as shown in Figure 4.5(b).

The sensor response, SR is defined as:

$$SR(\%) = \frac{Rg - R_o}{R_o} \times 100 \tag{4.7}$$

where R_o and R_g represent the resistance in air and resistance during VOC exposure, respectively. Within a sampling period of 650 s, the calibration graph of ethanol was linear $R^2 = 0.96$ (Figure 4.5(c)).

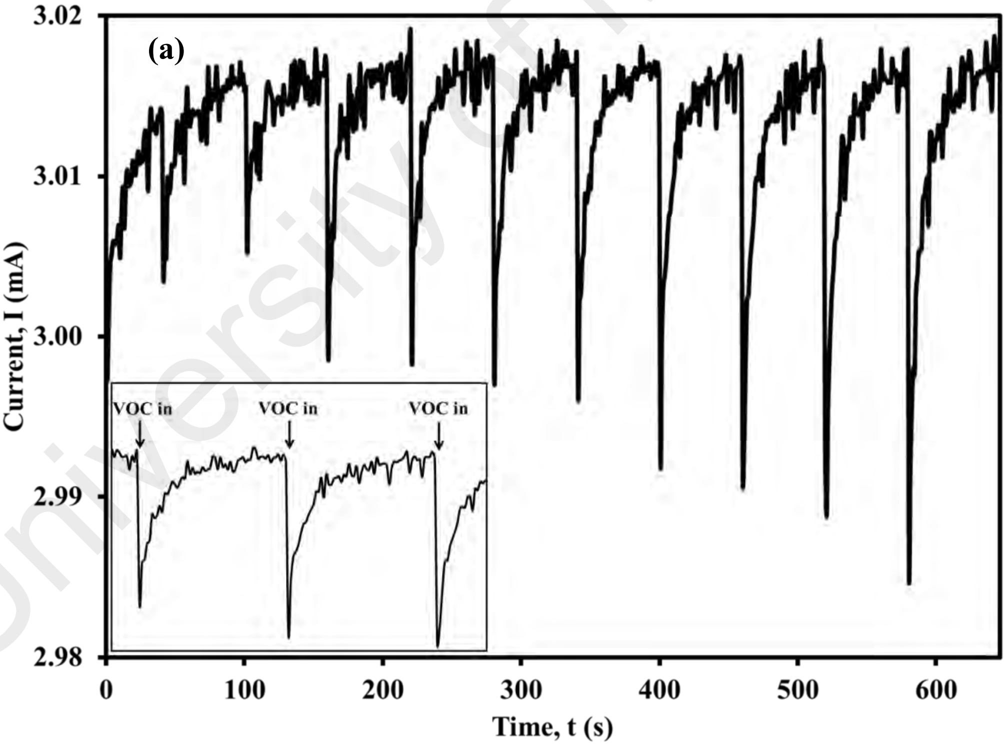

Figure 4.5: Output of ethanol sensing for MWCNTs (a) current vs time (b) resistance vs time and (c) sensor response versus ethanol concentrations.

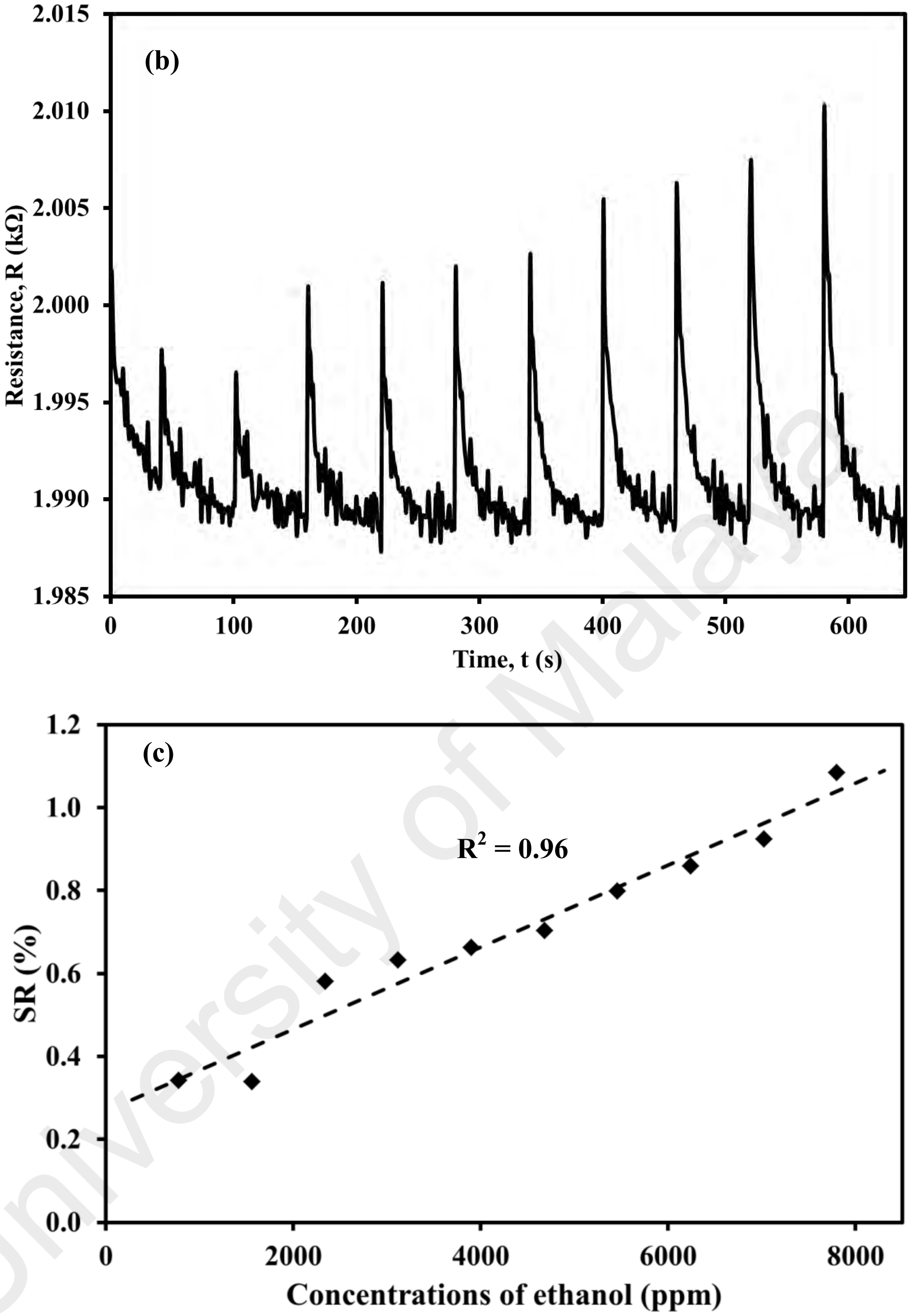

Figure 4.5, continued.

4.3 Results and discussion

4.3.1 EDX and FESEM analysis

Figure 4.6 shows the EDX spectrum of ZnO decorated MWCNTs synthesis with different amount of $Zn(NO_3)_2.6H_2O$ sample. Peaks due to C, Zn, O, Si, Ni and S were observed. The presence of Ni was due to the Ni being used as catalyst in CVD process to grow MWCNTs. Sulphur was from SDS used for the dispersion of MWCNTs and Si was from silicon wafer used as substrate for the EDX analysis. ZnO decoration levels of different concentration of $Zn(NO_3)_2.6H_2O$ used is summarized in table along with each EDX spectrum.

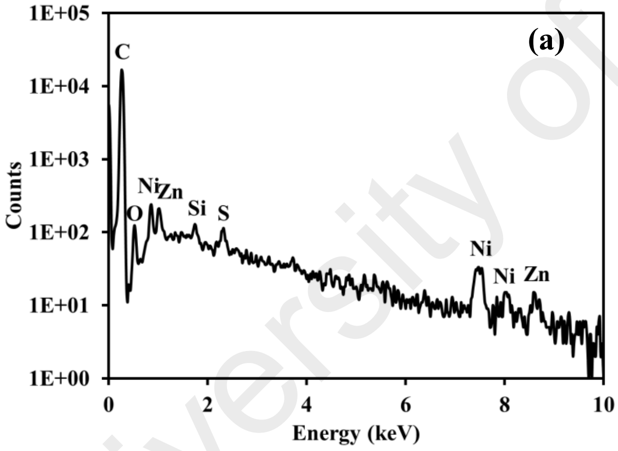

Elements	Weight (%)	Atomic (%)
C K	95.83	98.06
O K	1.87	1.44
S K	0.21	0.08
Ni K	1.23	0.26
Zn L	0.85	0.16

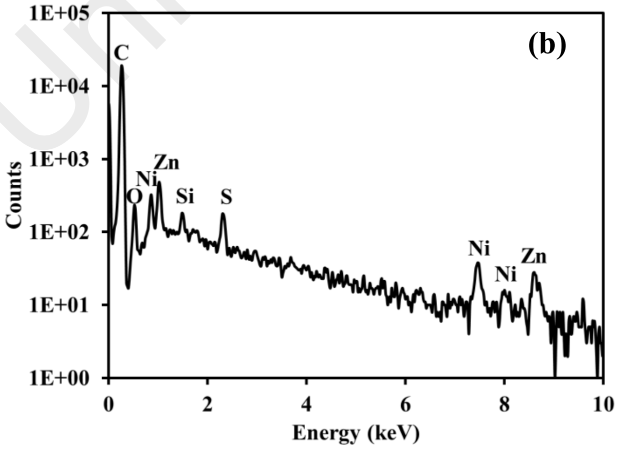

Elements	Weight (%)	Atomic (%)
C K	91.62	96.15
O K	3.53	2.78
S K	0.48	0.19
Ni K	1.45	0.31
Zn L	2.91	0.56

Figure 4.6: EDX and spectrum analysis of decorated MWCNTs with different amounts of $Zn(NO_3)_2.6H_2O$ used; (a) 2 wt. %, (b) 4 wt. %, (c) 6 wt. %, (d) 8 wt. % and (e) 10 wt. %.

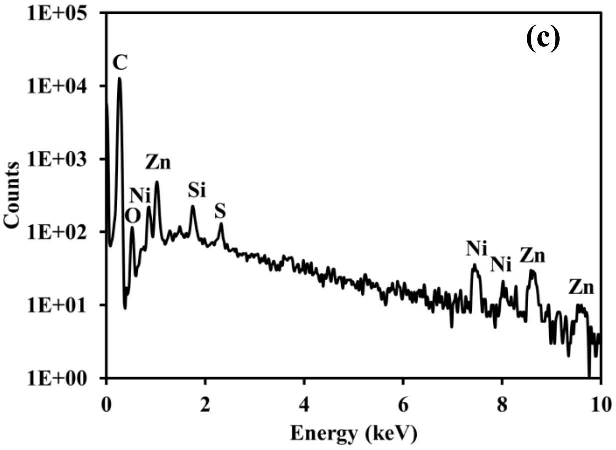

Elements	Weight (%)	Atomic (%)
C K	92.59	97.07
O K	2.39	1.88
S K	0.28	0.11
Ni K	1.47	0.32
Zn L	3.27	0.63

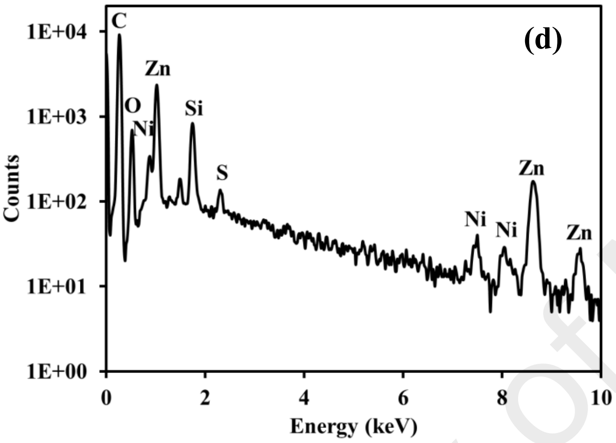

Elements	Weight (%)	Atomic (%)
C K	75.40	87.85
O K	10.30	9.01
S K	0.25	0.11
Ni K	0.81	0.19
Zn L	13.25	2.84

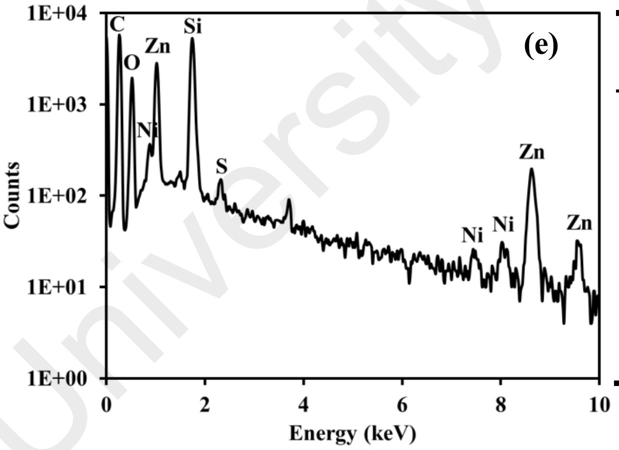

Elements	Weight (%)	Atomic (%)
C K	58.44	73.69
O K	18.54	17.55
S K	0.19	0.09
Ni K	0.35	0.09
Zn L	11.51	2.67

Figure 4.6, continued.

As shown in Figure 4.7, the percentage ratio of ZnO decorated MWCNTs increased non-linearly with composition of $Zn(NO_3)_2.6H_2O$ used during synthesis. From the EDX results, it was discovered that using 2, 4, 6, 8 and 10 wt. % of $Zn(NO_3)_2.6H_2O$ produced ZnO decoration at 0.002, 0.006, 0.007, 0.032 and 0.036 mol %, respectively.

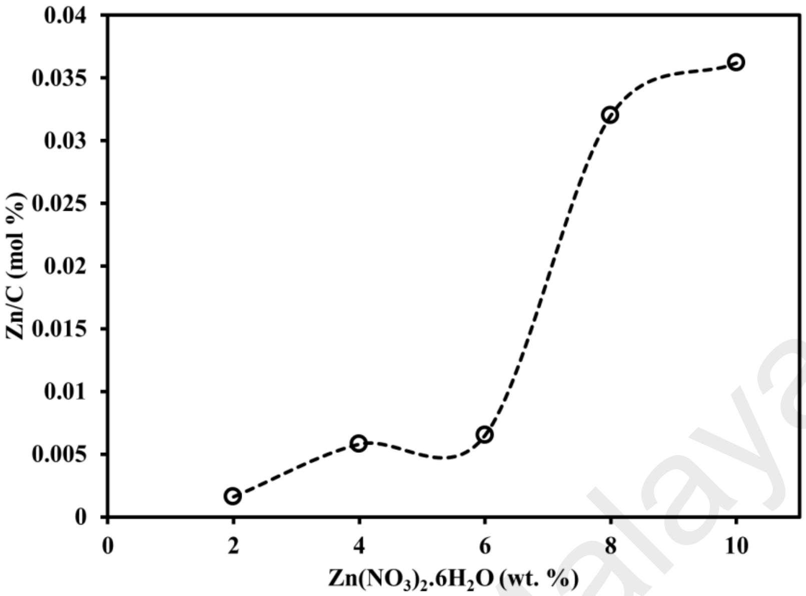

Figure 4.7: Zn over C versus $Zn(NO_3)_2.6H_2O$ weight percent.

Figure 4.8 shows FESEM images for MWCNTs with 20-30 nm diameter fabricated on a printing paper substrate. In Figure 4.8(a) the cellulose fibers of printing paper are appeared to be randomly oriented on the surface. The diameters of the fibers were about 15 µm. It can be observed from the image that cellulose surfaces were covered with MWCNTs which became more evident form a close-up view shown in Figure 4.8(c). The images showed that paper cellulose can be used to bind pure MWCNTs together in order to form free standing samples.

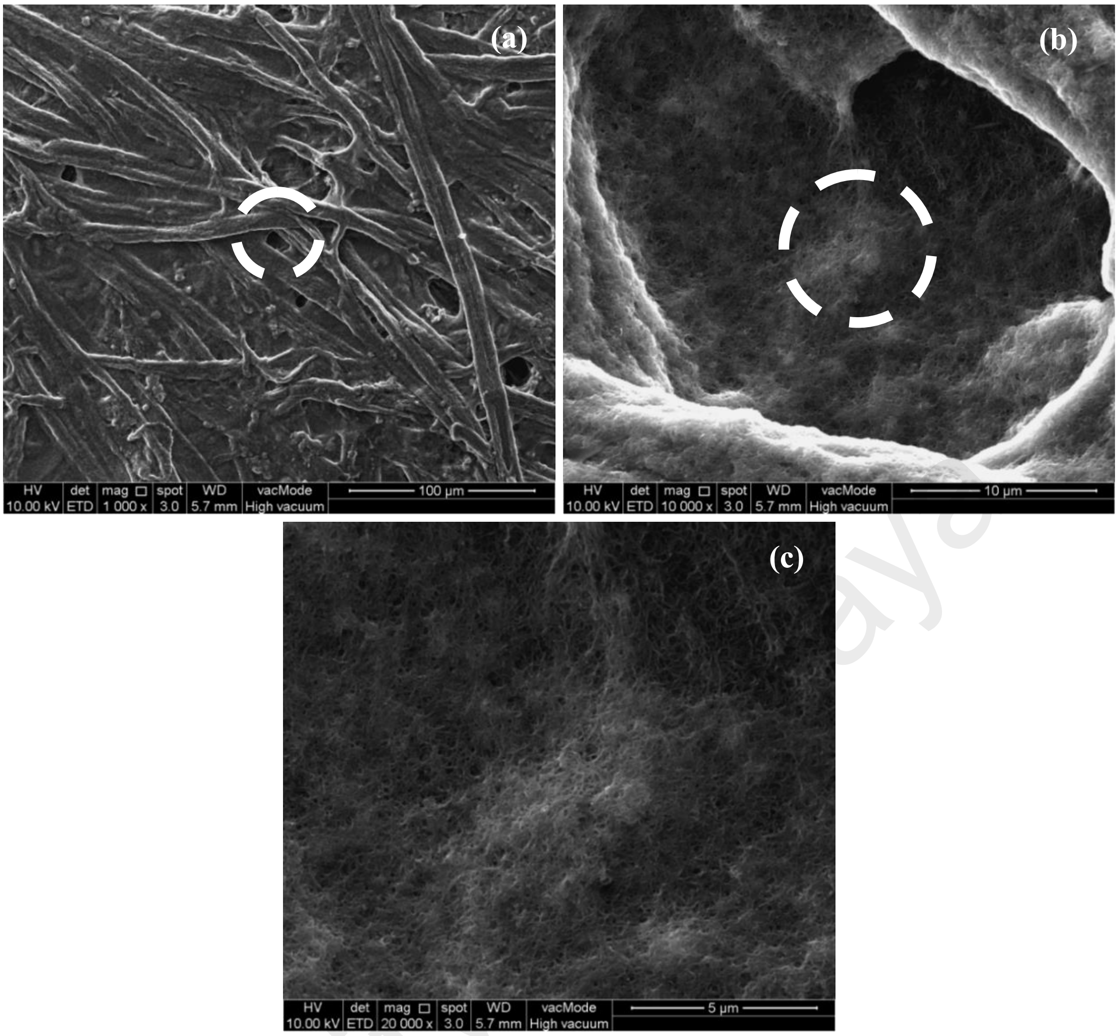

Figure 4.8: FESEM images of MWCNTs with diameter 20-30 nm on printing paper substrate in magnifications (a) 1k, (b) 10k and (c) 20k.

Figure 4.9 shows FESEM images for different diameters MWCNTs used in this experiment. For MWCNTs with diameter of ~8 nm (Figure 4.9(a)), it was observed that the bundles of MWCNTs entangled with each other. As for MWCNTs of diameter 20-30 nm (Figure 4.9(b)), the bundles of MWCNTs were in diameter range of 19.5 nm to 30.1 nm. For the biggest diameter MWCNTs labeled as ~50 nm (Figure 4.9(c)), it was estimated that the diameter was in the range of 49.6 nm to 52.8 nm. Overall, all different diameters of MWCNTs appeared as bundle of seamless cylindrical entangle to each other.

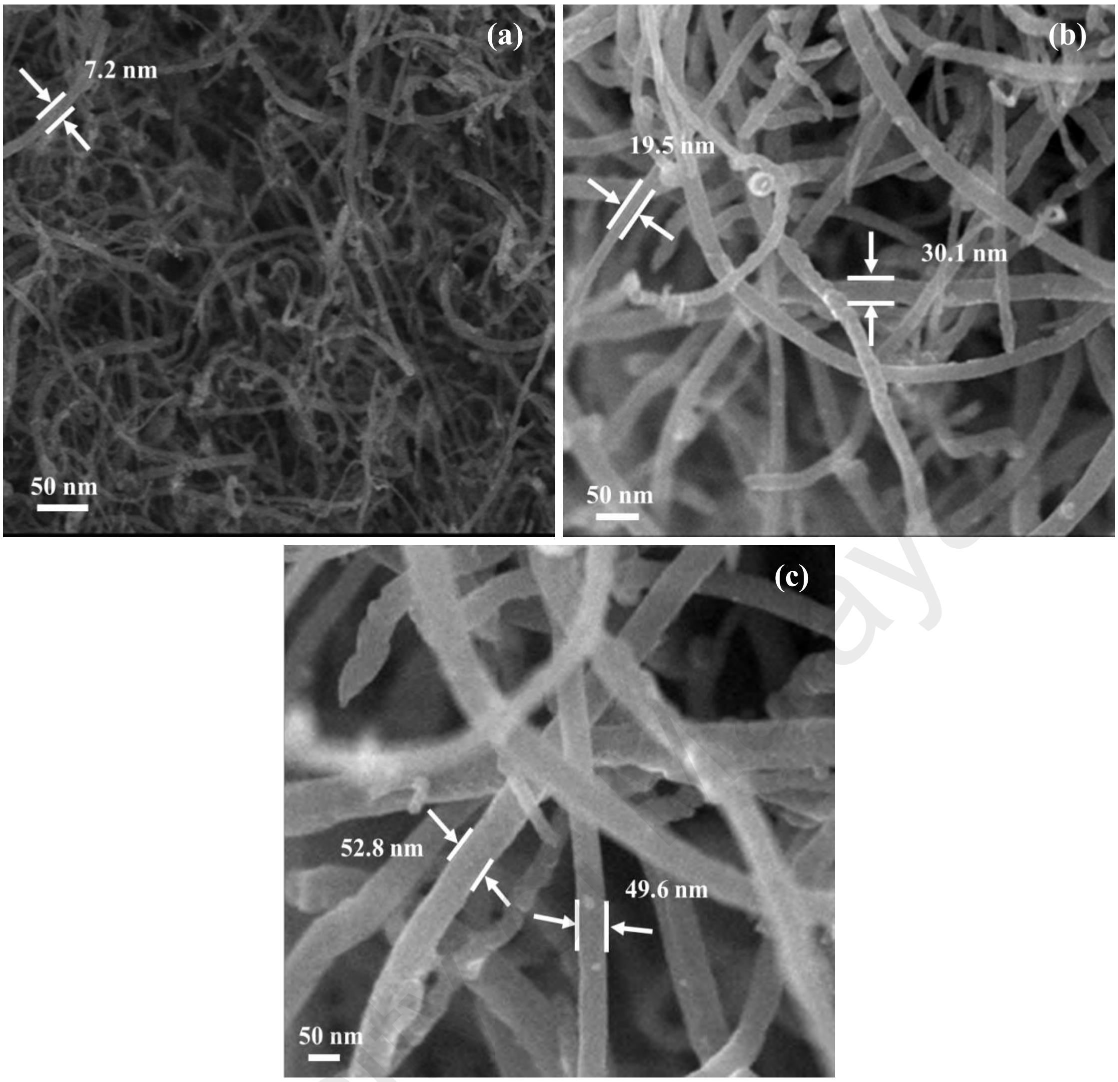

Figure 4.9: FESEM images of different diameters of MWCNTs; (a) ~8 nm, (b) 20-30 nm and (c) ~50 nm.

Figure 4.10 shows FESEM images of pure MWCNTs and different amount of ZnO decorated with MWCNTs. Pure MWCNTs were curved, tangled and with smooth surfaces (Figure 4.10(a)). Figure 4.10(b)-(e) show typical ZnO decorated MWCNTs structures. It can be seen that at low decorated concentration of precursor (0.002 mol % and 0.006 mol %), the ZnO grew around MWCNTs surface and formed an enclosure.

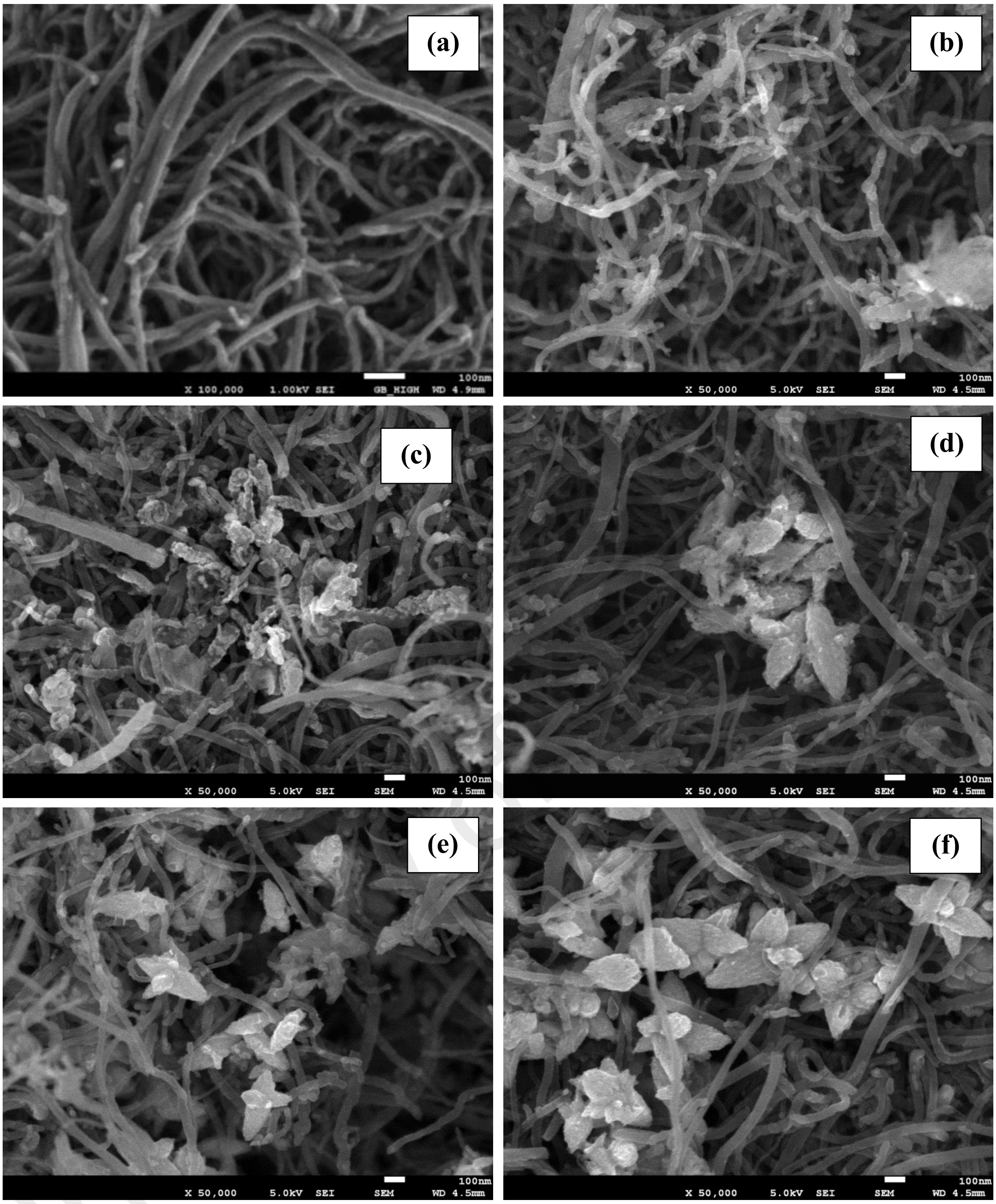

Figure 4.10: FESEM images of decorated MWCNTs with ZnO at (a) 0 mol %, (b) 0.002 mol %, (c) 0.006 mol %, (d) 0.007 mol %, (e) 0.032 mol % and (f) 0.036 mol %.

Figure 4.10(d)-(f) shows flower-like ZnO microstructures with average length of flower petals about 2 μm. It can be seen from Figure 4.10(e) that the growth of ZnO particles were well distributed and uniform above MWCNTs surface. The size of ZnO flower petals increased with increasing amount of precursor Zn concentration used, as shown in Figure 4.10(f). Thus, depending on the Zn precursor concentration, the ZnO can grow throughout completely, covering the MWCNTs surface.

In order to enhance ZnO decoration of MWCNTs, high density of active sites for Zn^{2+} ions condensation should be available (Jiang & Gao, 2005). Originally, the Zn^{2+} ions from $Zn(NO_3)_2.6H_2O$ would nucleate on the surface of MWCNTs because of electrostatic attraction and then produce ZnO nanoparticles when NaOH added to the solution. This can be explained by the simple chemical reaction between zinc nitrate hexahydrate and sodium hydroxide and schematic diagram as shown in Figure 4.11 and Equation 4.8-4.10 (Shi et al., 2013; Wu et al., 2006). Firstly, with the presence of alkali solution, (NaOH), $Zn(NO_3)_2.6H_2O$ produced $Zn(OH)_2$ as in Equation 4.8. Through the interaction with the alkaline solution, $Zn(OH)_2$ changed to $\mathrm{Zn(OH)_4^{2-}}$ as shown in Equation 4.9. $\mathrm{Zn(OH)_4^{2-}}$ produced into ZnO (Equation 4.10) through hydrothermal process. This process continued until the ZnO nuclei form agglomeration to each other due to supersaturated. Furthermore, the increasing concentration of $\mathrm{Zn(OH)_4^{2-}}$ will lead to the development ZnO crystal into nanorods form, and the creation of flower-like ZnO as shown in Figure 4.10(b) to (f).

$$Zn(NO_3)_2.6H_2O + 2NaOH \rightarrow Zn(OH)_2 + 2NaNO_3 + 6H_2O \quad (4.8)$$

$$\mathrm{Zn(OH)_2 + 2OH^- \rightarrow Zn(OH)_4^{2-}} \quad (4.9)$$

$$\mathrm{Zn(OH)_4^{2-} \rightarrow ZnO + 2H_2O + 2OH^-} \quad (4.10)$$

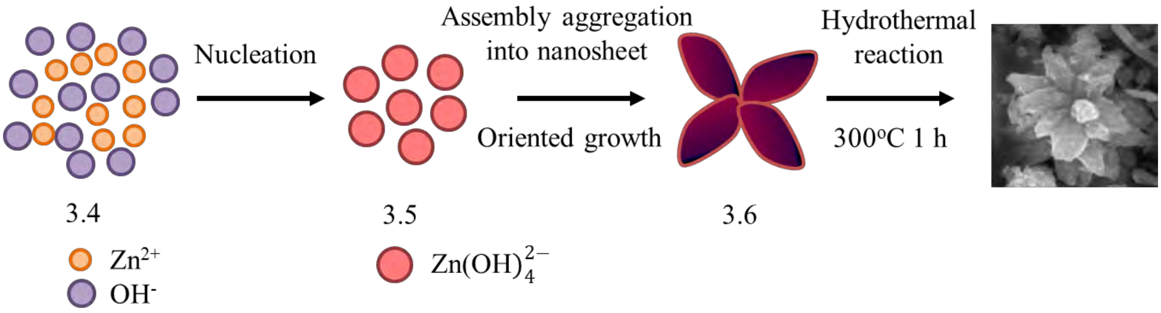

Figure 4.11: Schematic diagram of possible formation process of flower-like ZnO NPs.

It can be observed that the increment of decorated element ($Zn(NO_3)_2.6H_2O$), had evidently increased the diameter of flower-like ZnO structure grown on the MWCNTs surface. ZnO nanoparticles were more efficiently bound on the entangled MWCNTs in the solution since there were no active sites on the surface of MWCNTs for the in-situ growth of ZnO (Du et al., 2008).

4.3.2 Thermogravimetric Analysis (TGA)

Figure 4.12 is the thermal analysis samples of MWCNTs on printing paper and pure printing paper. For printing paper, thermal decomposition occurred in two steps as it is observed from the derivative weight change curve by the presence of two peaks. The first step corresponds to cellulosic materials have thermal degradation began at about 270 °C and was essentially completed by approximately 380 °C with a peak at 320 °C (Arenales Rivera et al., 2016). This cellulosic material decomposed by mainly carbon-carbon and carbon-oxygen bonds for forming CO and CO_2 at lower temperature. The second step is decomposed of carbon-hydrogen bonds for forming hydrogen and hydrocarbon at higher temperature. All these happen due to the bonding energy of carbon-carbon and carbon-oxygen is lower than that of carbon-hydrogen bonds (Bhuiyan et al., 2008).

In this experiment it was found that for printing paper, the first step start to occur between 220 ^{o}C to ~380 ^{o}C with 72.84 % of weight loss and peak at 327 ^{o}C. The second steps have in the temperature range between 580 ^{o}C to 640 ^{o}C and peak at 621 ^{o}C with 6.35 % weight loss. It can be noticed weight loss of printing paper remained constant after 640 ^{o}C to 850 ^{o}C. This is because of the dehydration and cross-linking reactions which will cause cellulose tends to be carbonized (Arseneau, 1971) and the rearrangement of cellulose structure after preheating process will provide end product of char residue (Maschio et al., 1992).

For samples containing MWCNTs with different diameters exhibit three steps. The first step was in the range between ~180 ^{o}C to ~240 ^{o}C and peak at ~216 ^{o}C with 4.53 % of weight loss. This weight loss is due to the decomposition of SDS (Sen et al., 2015) used as surfactant in this experiment. The second mass loss with maximum rate at ~334 ^{o}C and a hump at ~308 ^{o}C is due to the decomposition of cellulose (Arseneau, 1971) together with amorphous carbon impurities of the MWCNTs (Li & Zhang, 2005). The third mass loss occurred between ~380 ^{o}C to ~640 ^{o}C was due to decomposition of carbon (Shamsudin et al., 2012; Shamsudin et al., 2013), both originating from the paper and the MWCNTs deposited. The residual mass is attributed to the metal catalyst particles that remained as verified by EDX analysis in section 4.3.1. Amounts of MWCNTs incorporated in the sensor are visible based on the difference between samples of MWCNTs on printing paper and printing paper. For the samples measured, the incorporation MWCNTs on the paper substrates were about 0.6, 1.8 and 0.3 weight (%) for diameter ~8, 20-30, and ~50 nm respectively.

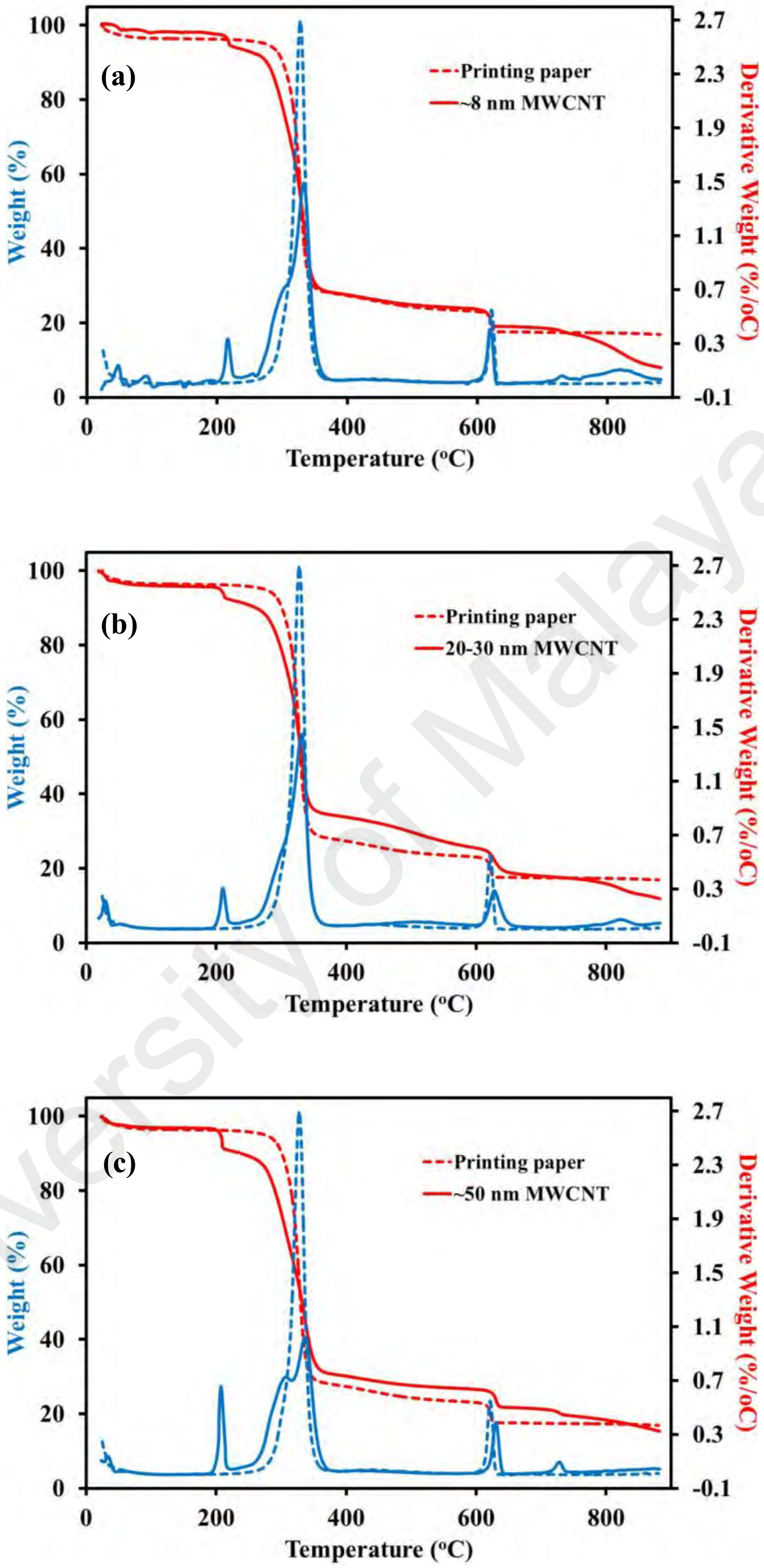

Figure 4.12: Thermal analysis curves of printing paper, and different diameters of MWCNTs samples; (a) ~8 nm, (b) 20-30 nm and (c) ~50 nm.

Figure 4.13 shows the thermal decomposition expressed in terms of weight loss as a function of temperature curves for printing paper and printing paper filled with different amounts of ZnO decorated MWCNTs. The weight loss trend of ZnO decorated MWCNTs on printing paper was similar to samples of MWCNTs on printing paper. The first step of weight loss for ZnO decorated MWCNTs occurred at ~200–250 ^{o}C with oxidation peak at ~213 ^{o}C. The highest weight loss achieved at 250-400 ^{o}C and consist two maximum rates. The first maximum rate was around 295 ^{o}C and the second maximum rate at ~337 ^{o}C. The last decomposition occurred at temperature between ~580 ^{o}C to 640 ^{o}C with oxidation peak at 620 ^{o}C. The incorporation of MWCNTs together with decorated ZnO on the printing paper was estimated as 0.5, 0.4, 0.3, 0.2 and 0.1 weight (%) for 0.002 mol %, 0.006 mol %, 0.007 mol %, 0.032 mol % and 0.036 mol %, respectively.

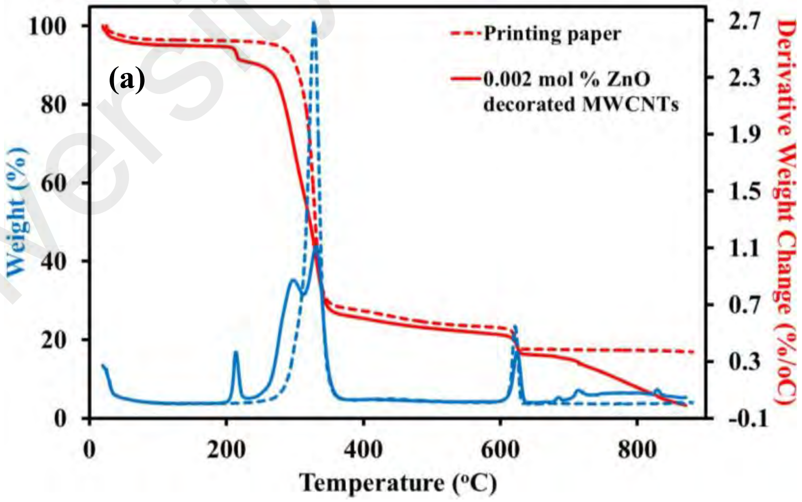

Figure 4.13: Thermal analysis curves of different amounts of ZnO; (a) 0.002 mol %, (b) 0.006 mol %, (c) 0.007 mol %, (d) 0.032 mol % and (e) 0.036 mol % decorated MWCNTs on the printing paper substrate.

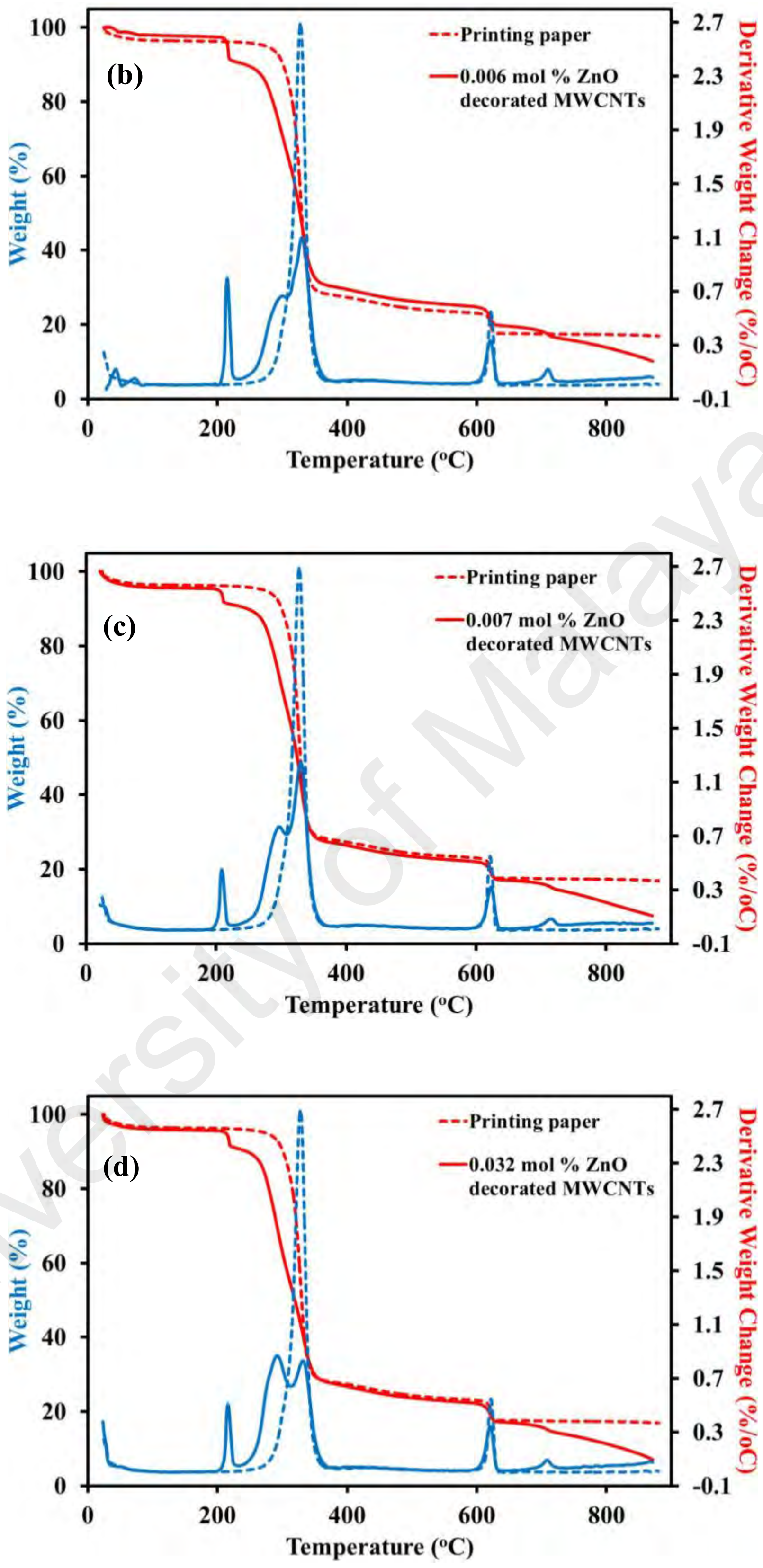

Figure 4.13, continued.

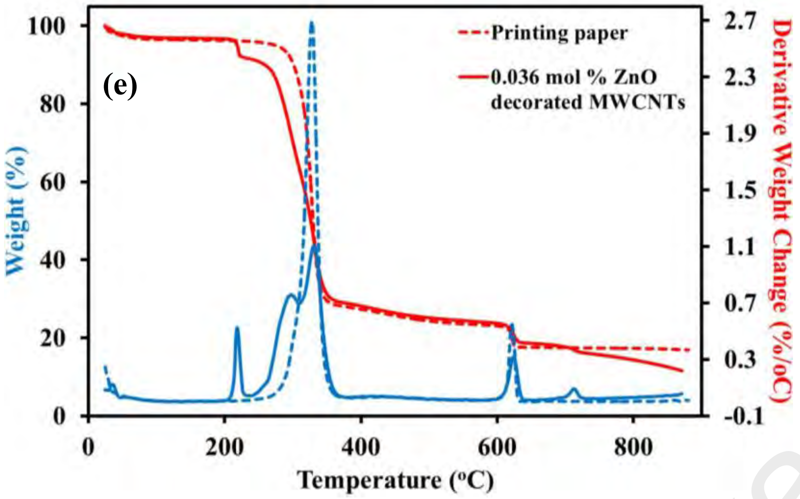

Figure 4.13, continued.

4.3.3 XRD analysis

XRD spectra of ZnO decorated MWCNTs samples are shown in Figure 4.14. Peaks at $2\theta = 26.23^{\circ}$, 43.01°, 44.60°, and 51.88° assigned to (0,0,2), (1,0,0), (1,0,1) and (2,0,0) planes of MWCNTs or graphite, respectively (Sun et al., 2006; Zhang et al., 2009). For ZnO decorated MWCNTs samples, diffractions of both MWCNTs and ZnO could be observed. The (1,0,0), (0,0,2), (1,0,1), (1,0,2), (1,1,0) and (1,0,3) plane of ZnO were observed at $2\theta = 31.84^{\circ}$, 34.50°, 36.33°, 47.65°, 56.73° and 63.01°, respectively indicating the hexagonal wurtzite ZnO structure (Kou et al., 2012). With the increase of ZnO concentration, the peaks of MWCNTs become weaker and the ZnO peaks tend to be sharper due to the increased presence of ZnO on the MWCNTs surface. The formation of ZnO depended on the solution concentration and calcination temperature. The availability of OH^- ions depended on the concentration of NaOH and the dissolution of $Zn(OH)_2$ during hydrothermal process.

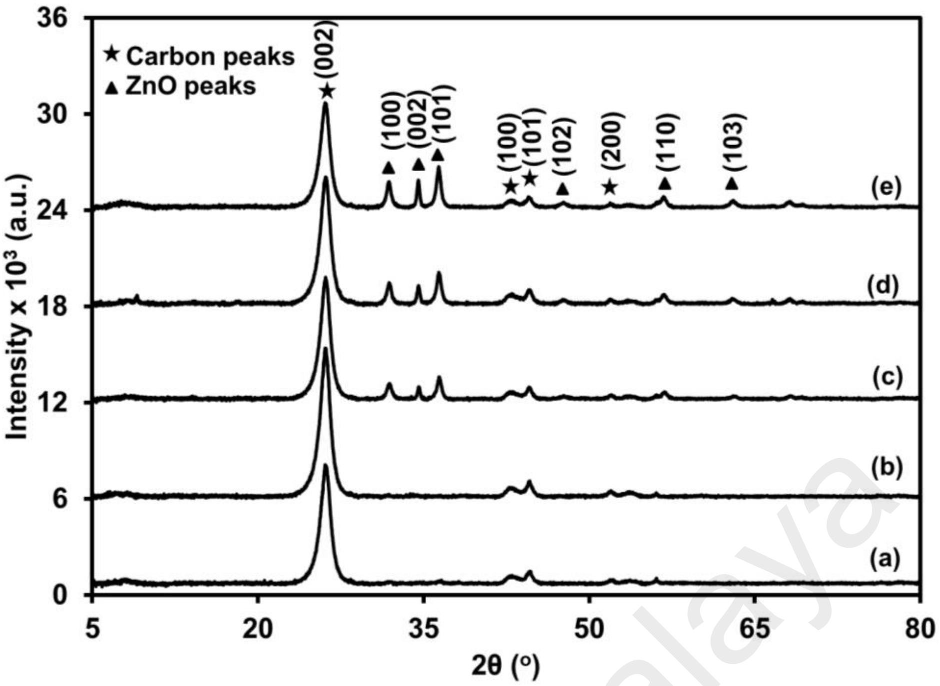

Figure 4.14: XRD spectra of different amounts of ZnO; (a) 0.002 mol %, (b) 0.006 mol %, (c) 0.007 mol %, (d) 0.032 mol % and (e) 0.036 mol % decorated MWCNTs.

4.3.4 Raman analysis

Crystallinity of CNTs can be characterized by using Raman spectroscopy. In Raman scattering, MWCNTs is like to be a combination of CNTs with different diameters ranging. Many difference characteristics which differ between Raman spectra in CNTs from that of graphite are not clearly seen in MWCNTs due to the large diameter of outer tubes for usual MWCNTs.

In the range of 1200 to 1700 cm^{-1}, all Raman spectra for all different diameters of MWCNTs samples in Figure 4.15 show four peaks located at ~1341, ~1575, ~1607 and ~2662 cm^{-1} which known as D, G, D’ and 2D bands respectively. The D band is attributed to the double-resonance band which indicated as a standard of structural disorder due to finite particle size (Hiura et al., 1993), curvature effects of graphene, defects due to pentagons or heptagons, and nanoscale or graphitic carbon particles material on the tubes (Bacsa et al., 1994; Eklund et al., 1995). The D' band is also a double-resonance Raman characteristics originally by disorder and defects (Shih & Li, 2008).

As mentioned earlier, D and D' can be explained by double resonance theory (Baranov et al., 1987). In Raman spectra of graphite the appearance of D band and other weak dispersive phonon modes was related with resonant enhancement of Raman intensity in two continuous scattering phenomena. Basically, an electron with momentum k is excited to the energy $E_i(\mathbf{k})$ by incident photon before scattered to a state $\mathbf{k} + \mathbf{q}$ $[E(\mathbf{k} + \mathbf{q})]$ and then backscattered to state k$[E_f(\mathbf{k})]$, and lastly remerged with a hole to provide the scattered photon. If $E(\mathbf{k} + \mathbf{q})$ and either $E_i(\mathbf{k})$ or $E_f(\mathbf{k})$ states correspond to real electronic states, the Raman intensity is increase by two resonant factors in the denominators appearing in the intensity formula, and this is called as the double-resonance Raman process (Grüneis et al., 2002).

The G band is from C-C stretching vibrations on the CNTs axis (Gonzalez et al., 2012). From previous research that using several excitation wavelengths have showed that G peak does not distribute in graphite itself, nanocrystalline graphite, or glassy carbon but it can be dispersed in more disordered carbon which the dispersion is proportional to the degree of disorder (Antunes et al., 2006).

The 2D band is caused by a double-resonance effect similar to the D band but caused by two inelastic phonon scattering processes (Saito et al., 2002). This band can also be observed in high quality graphitic materials since there are no defects necessary for this band (Dresselhaus et al., 2005).

The D to G band intensity ratios (I_D/I_G) for ~8, 20-30 and ~50 nm are 0.21, 0.59 and 0.76, respectively. MWCNTs with the lowest diameter exhibit the lowest ratio and thus the most highly ordered CNTs or purest species in this study. It implies that the degree of structural disorder or defects can be noticeable for different diameters of MWCNTs samples. This amount is important to be calculated as any chemical reactions with CNTs are more likely occurred at disordered regions than ordered regions.

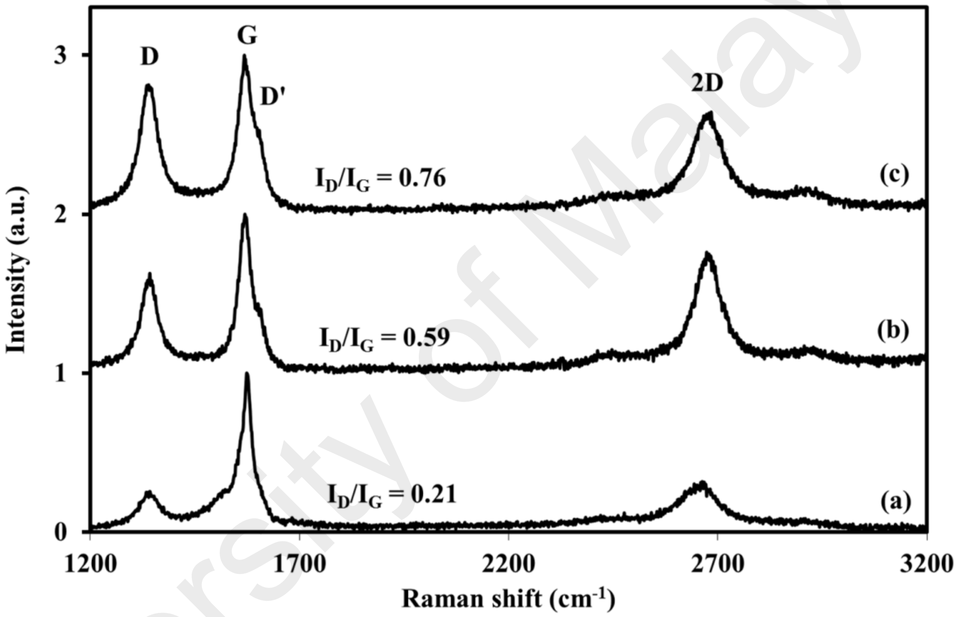

Figure 4.15: Raman spectra of MWCNTs with diameters (a) ~8 nm, (b) 20-30 nm and (c) ~50 nm.

4.3.5 HRTEM analysis

Figure 4.16 shows images of different diameters MWCNTs used as sensor in this experiment with high resolution lattice images for each diameter. Each MWCNT sample was named from the average diameter estimated by HRTEM imaging as specified by the supplier and it was found that from the HRTEM observation that the values were quite consistent. As example, the MWCNTs named as ~8 nm, 20-30 nm and 50 nm indicates an average diameter of 8.5 nm, 20.2 nm and 55.7 nm, respectively as shown in Figure 4.16(a)-(c).

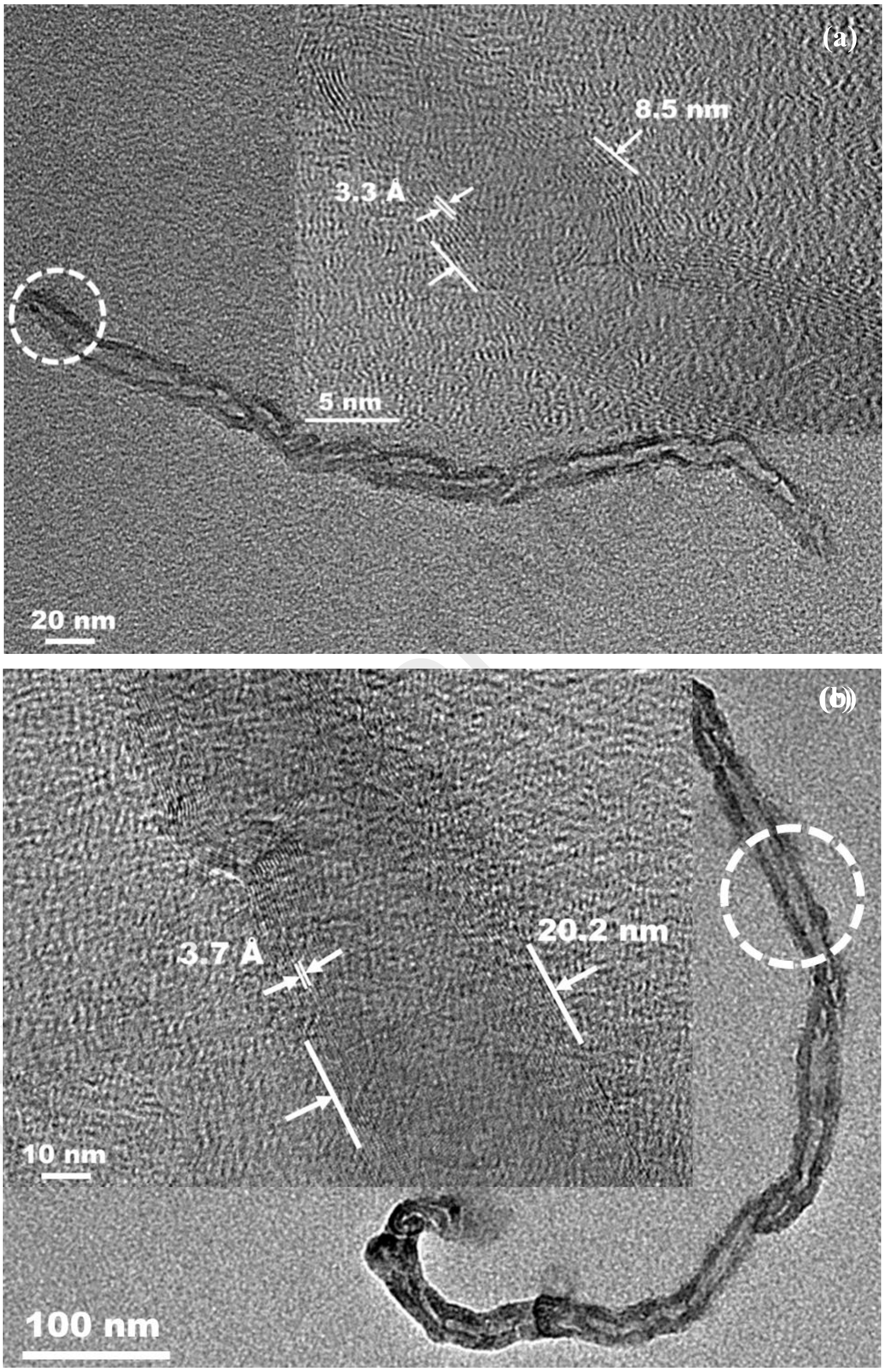

Figure 4.16: HRTEM images for different diameters MWCNTs; (a) ~8 nm, (b) 20-30 nm and (c) ~50 nm.

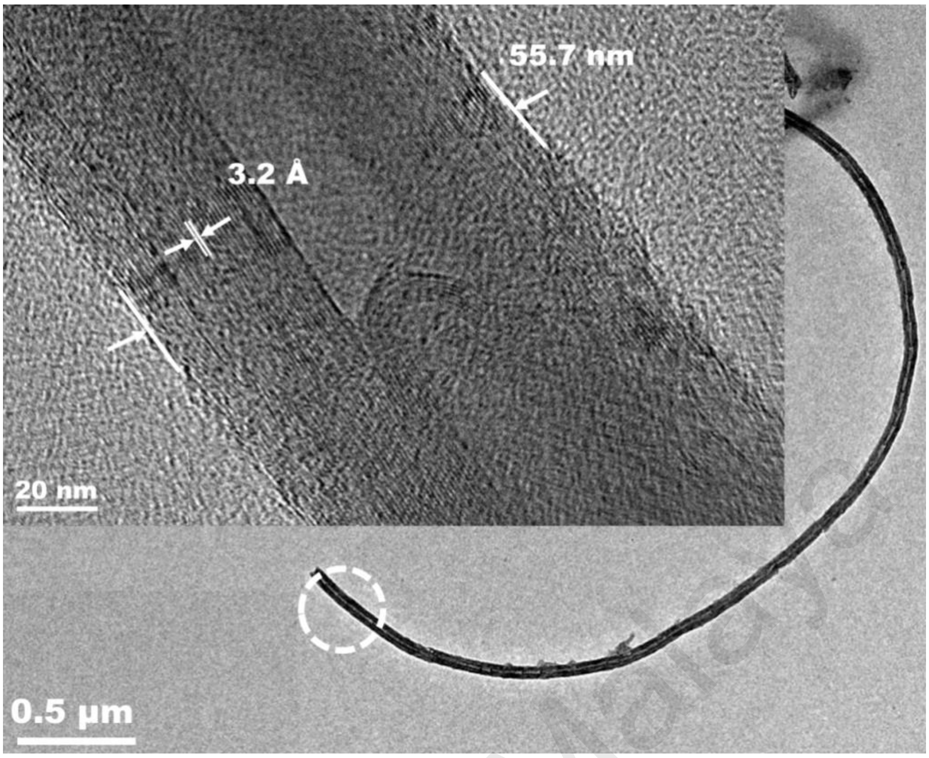

Figure 4.16, continued.

HRTEM was performed to further study the morphology and microstructure of ZnO decorated on surface of the MWCNTs. The HRTEM image of ZnO decorated MWCNTs (Figure 4.17(a)) shows bead shaped nanoparticles densely attached on the MWCNTs surface. The ZnO grow in size and pile up on each other as Zn dosage increases, resulting in a dense with MWCNTs deeply embedded. High resolution TEM confirmed that most of the bead shaped ZnO nanoparticles were single crystalline. Figure 4.17(c) is a high resolution HRTEM image showing the (100) lattice plane of a ZnO crystal with a hexagonal structure having an interplanar distance of 0.26 nm. From HRTEM images it can also showed that the adhesion of ZnO particles on the walls of MWCNTs is very strong even though the sample has been ultrasonicated for the preparation of the HRTEM sample.

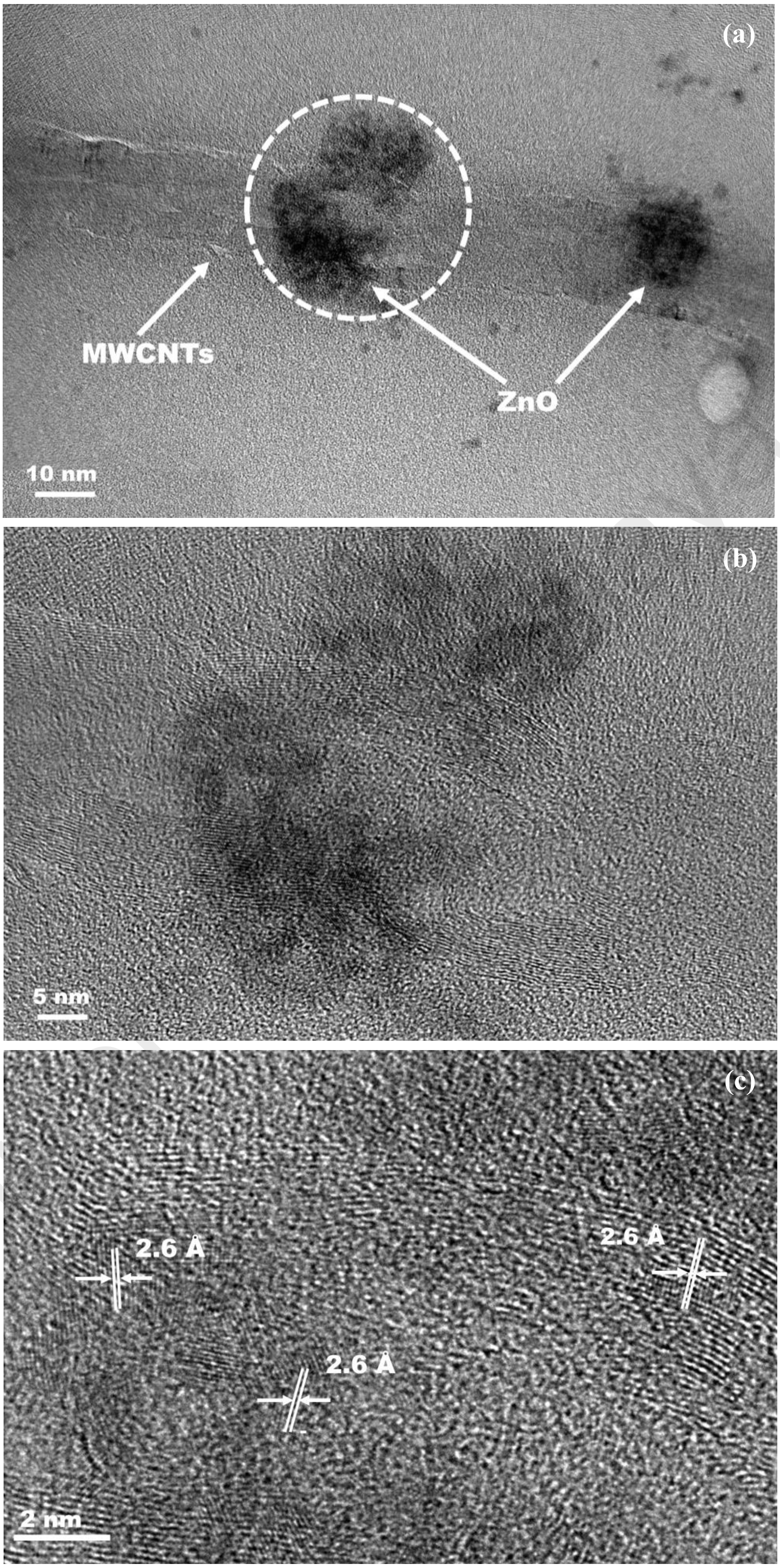

Figure 4.17: (a), (b) and (c) HRTEM images of ZnO decorated MWCNTs.

4.3.6 Effect of Different Diameters MWCNTs towards VOC

Generally, there are few kind of site for adsorption occurred on MWCNTs as shown in Figure 4.18 which are external surface of the bundle (Wang & Yeow, 2009; Young & Lin, 2016), groove formed at the contact between adjacent tubes on the outside of the bundle (Wang & Yeow, 2009; Young & Lin, 2016), interior pore of individual tubes (Wang & Yeow, 2009) and interstitial channel formed between three adjacent tubes within the bundle (Wang & Yeow, 2009; Young & Lin, 2016).

The adsorption of gas molecules is determined by site availability and binding energy of the adsorbate gas. For some gases, not all of these sites were available because of gas molecule dimension and the site diameter. Adsorption gas for inner pore can only happen when MWCNTs is uncapped or has imperfection on tube walls (Adu et al., 2001).

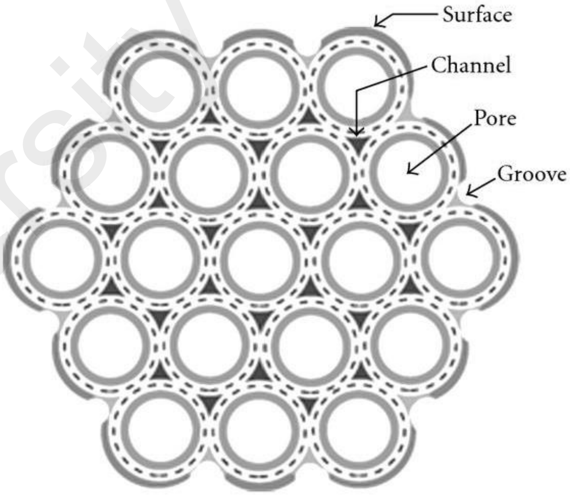

Figure 4.18: Diagram of MWCNTs in bundle represents the sites for adsorption (Wang & Yeow, 2009).

4.3.6.1 Ethanol vapor

Figure 4.19 shows the variation of resistance for sensors fabricated from different diameter MWCNTs exposed to different concentrations of ethanol vapor. All samples showed similar trend which increase in resistance upon exposure to ethanol vapor. The mechanism of resistive response of the sensors due to ethanol vapor exposure can be viewed as the closing of the conduction channel in the MWCNTs. Adsorption of ethanol molecules temporarily bound to electrons on the MWCNTs wall reduced the conductivity of the MWCNTs. Once the ethanol molecules removed from the MWCNTs wall, the conduction channel was free thus the resistivity was reduced to original position.

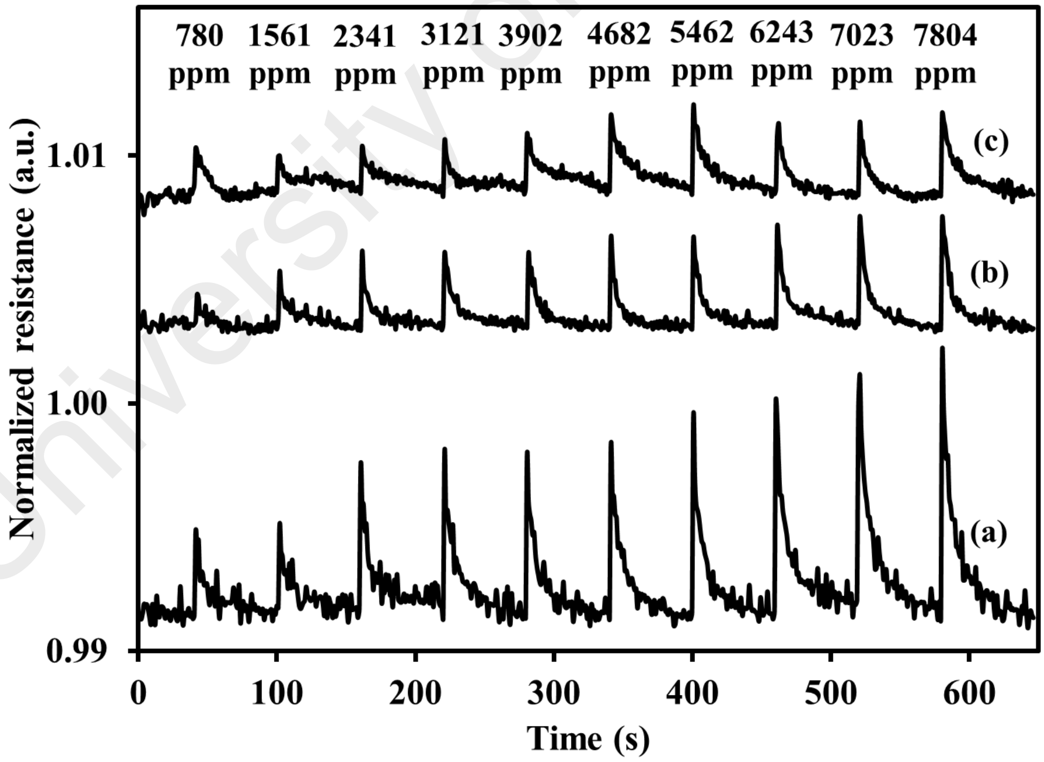

Figure 4.19: Normalized resistance for fabricated sensor in the range 780 to 7804 ppm with different MWCNTs diameters; (a) ~8 nm, (b) 20-30 nm and (c) ~50 nm.

Response time is the time taken for sensor to react to a step concentration change from zero to a certain concentration value. Recovery time is the time it needed for the sensor signal to restore to its initial value after a step concentration change from a certain value to zero. An example of how to estimate response time and recovery time was shown in Figure 4.20. From this plot, it can be estimated the response and recovery times are ~2 s and 17-28 s, respectively. It also can be seen that the characteristics of these sensors are almost reproducible as well as quick response and recovery time.

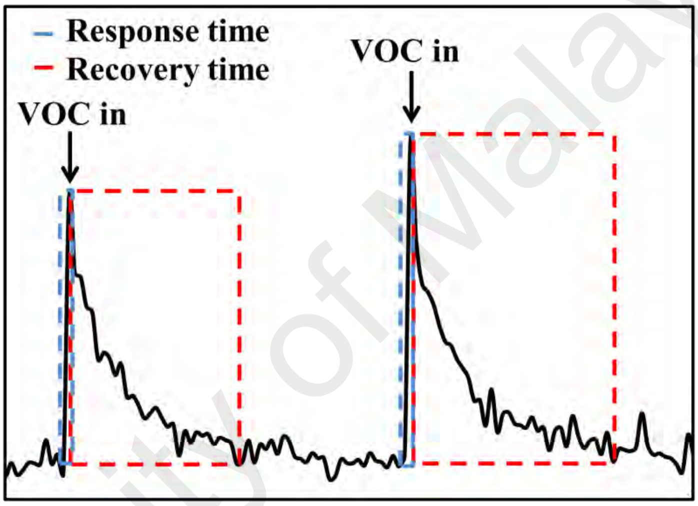

Figure 4.20: The estimation of response and recovery time for VOC sensing.

Sensor response to several concentrations of ethanol vapor towards variety diameters MWCNTs is shown in Figure 4.21. The value for each sensor response was calculated according to Equation 4.7. From the plots, it can be seen that there is linear relation between the sensor response and ethanol vapor for concentration from 780 to 7804 ppm. Compared to other diameters (20-30 nm and ~50 nm), the lowest diameter of MWCNTs (~8 nm) shown the highest response to ethanol vapor, followed by 20-30 nm and lastly ~50 nm. Our results showed that a trend of high response with smaller diameter MWCNTs was evident.

Beside sensor response, sensitivity is another property in vapor sensors that can be measured from sensor response. Sensitivity is the change of measured signal per analyte concentration unit, i.e., the slope of a calibration graph. The sensitivity of VOC used in this experiment was calculated by using equation:

$$Sensitivity = \frac{\Delta SR(\%)}{\Delta C} \tag{4.11}$$

where ΔSR is the change in sensor response over the change of VOC concentration or in other words is the gradient for sensor response versus VOC concentration graph as shown in Figure 4.21.

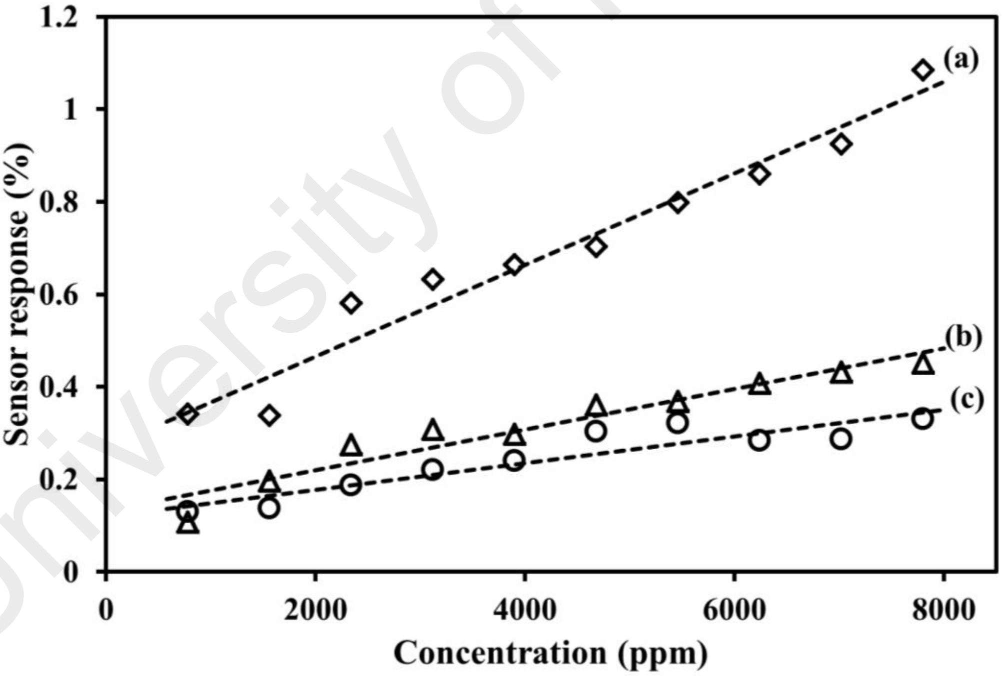

Figure 4.21: Sensor response to different concentrations of ethanol vapor in the range 780 to 7804 ppm for different MWCNTs diameters; (a) ~8 nm, (b) 20-30 nm and (c) ~50 nm.

The sensor response and sensitivity values of different diameters MWCNTs in the order of ~8 > 20-30 > ~50 nm is shown in Figure 4.21. The trend of higher sensitivity observed in MWCNTs of small diameter, i.e. ~8 nm compared to that of 20-30 and ~50 nm can be due to the effective surface area and initial conductivity (Figure 4.22). The total surface area due to MWCNTs of smaller diameters is expected to be larger than that of larger diameters. Also, marked difference in conductivity was observed based on the values of the initial resistance of 2.002, 0.472 and 0.293 kΩ for samples fabricated from MWCNTs of diameter ~8, 20-30 and ~50 nm respectively.

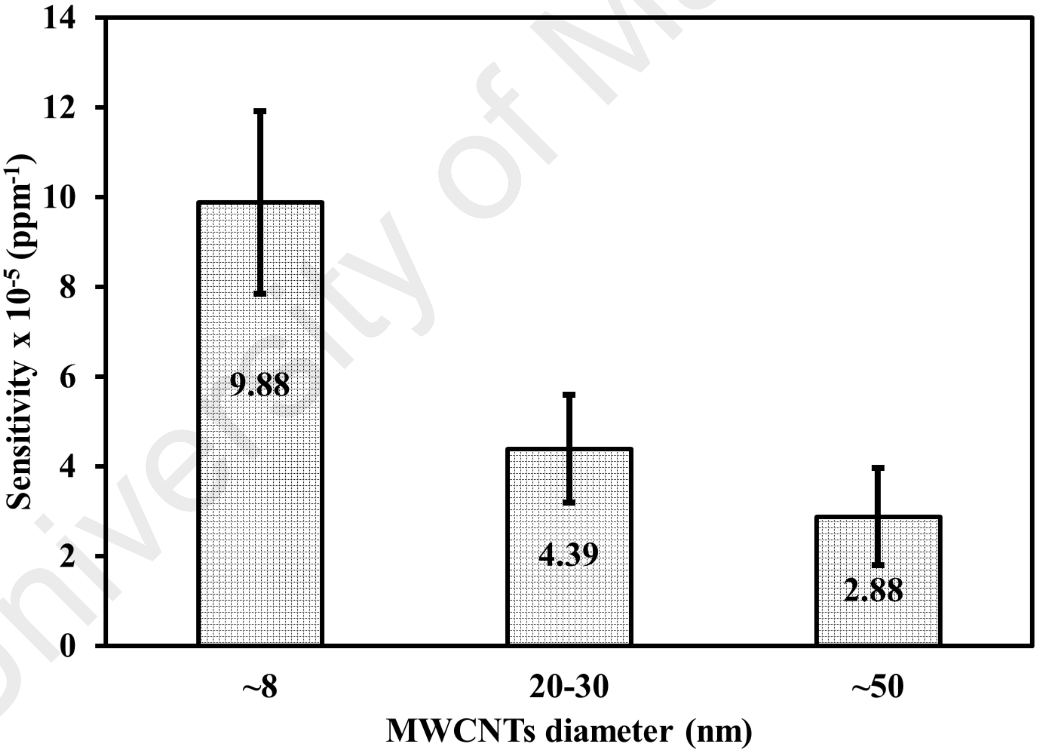

Figure 4.22: Histogram sensitivity of ethanol vapor for MWCNTs with different diameters.

4.3.6.2 Toluene vapor

Toluene detection experiments were performed for different samples with MWCNTs diameters at room temperature (Figure 4.23). The responses of tested samples were done in the range of 425 to 4253 ppm. Sensor resistance for all the samples increases in the presence of toluene vapor with response time ~2 s and the recovery time varied in the range of 11 to 40 s depending on the toluene concentrations applied.

Beside the surface area, the adsorption mechanisms of MWCNTs involved the interstitial and channel areas formed between the MWCNTs and inner pores of the tubes. Organic molecules which in this case toluene, containing π electrons (C=C double bonds or benzene rings) can form π-π bonds with MWCNTs since every carbon atom in MWCNTs has a π electron orbit perpendicular to the MWCNTs surface (Woods et al., 2007).

The resistance of sample increase upon exposure to toluene vapor and returns to its original value when expose to the air. This phenomenon can be explained by the effect of methyl groups in toluene which will function as weak charge donors and provide electrons which partially neutralized charged of the holes in MWCNTs which lead to increase the electrical resistance (Zhou et al., 2014).

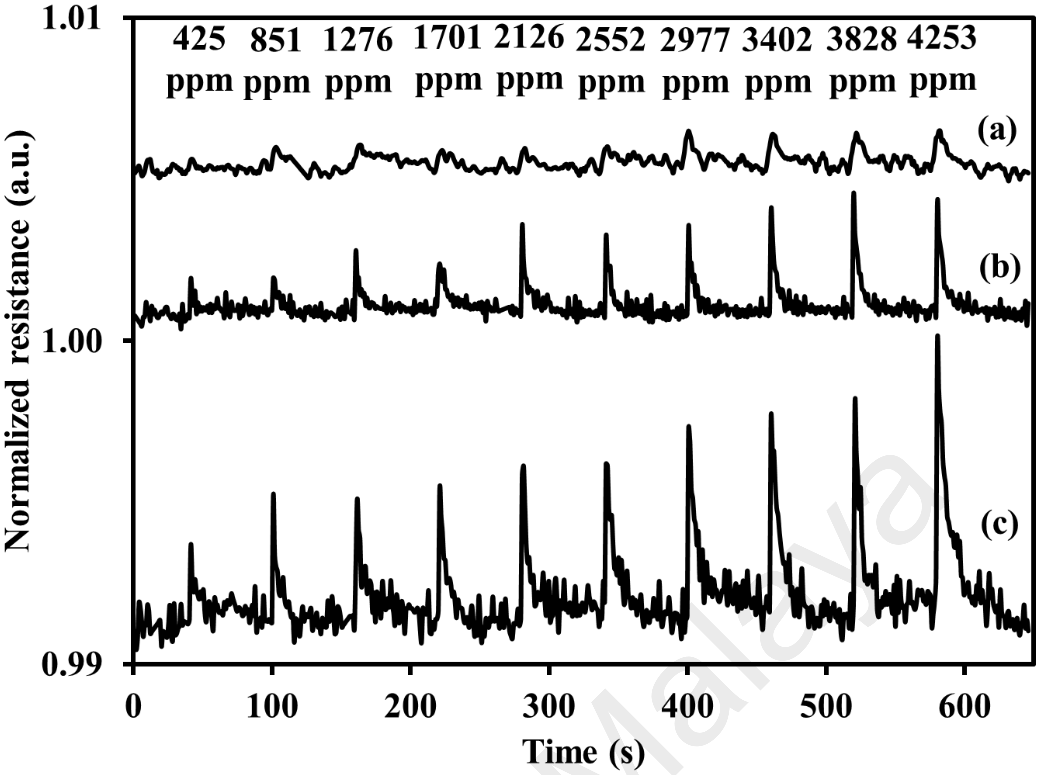

Figure 4.23: Normalized resistance in different toluene concentration with different MWCNTs diameters; (a) ~50 nm, (b) 20-30 nm and (c) ~8 nm.

Figure 4.24 shows the relations between sensor responses for different concentration of toluene calculated using Equation 4.7. The sensitivity value (Figure 4.25) and the sensor response of MWCNTs of different diameters (Figure 4.24) indicated that there was a trend of higher sensitivity according to diameter ~8 > 20-30 > ~50 nm of MWCNTs. This may be due to the initial conductivity and effective surface area of the samples.

Based on the values of the initial resistance of samples fabricated (2.06, 0.49 and 0.30 kΩ for MWCNTs with diameters ~8, 20-30 and ~50 nm respectively), there were different initial conductivities. It also known that the total surface area per gram and pore volume of smaller outside diameters MWCNTs is larger than that of larger outside diameters (Hilding et al., 2001).

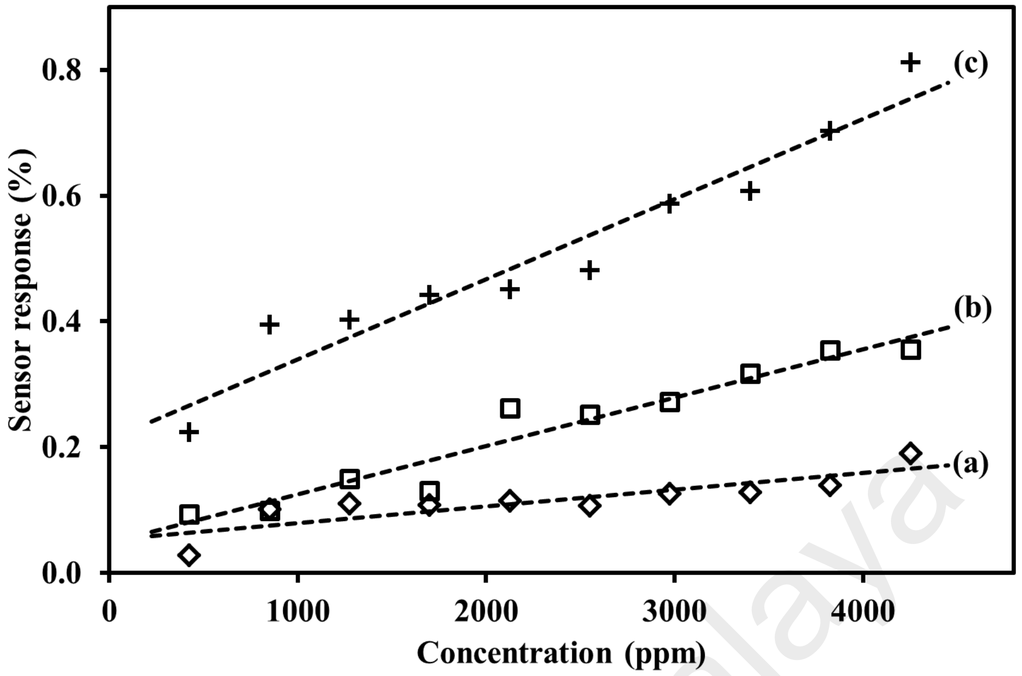

Figure 4.24: Sensor response over different concentration of toluene for MWCNTs with diameters; (a) ~50 nm, (b) 20-30 nm and (c) ~8 nm.

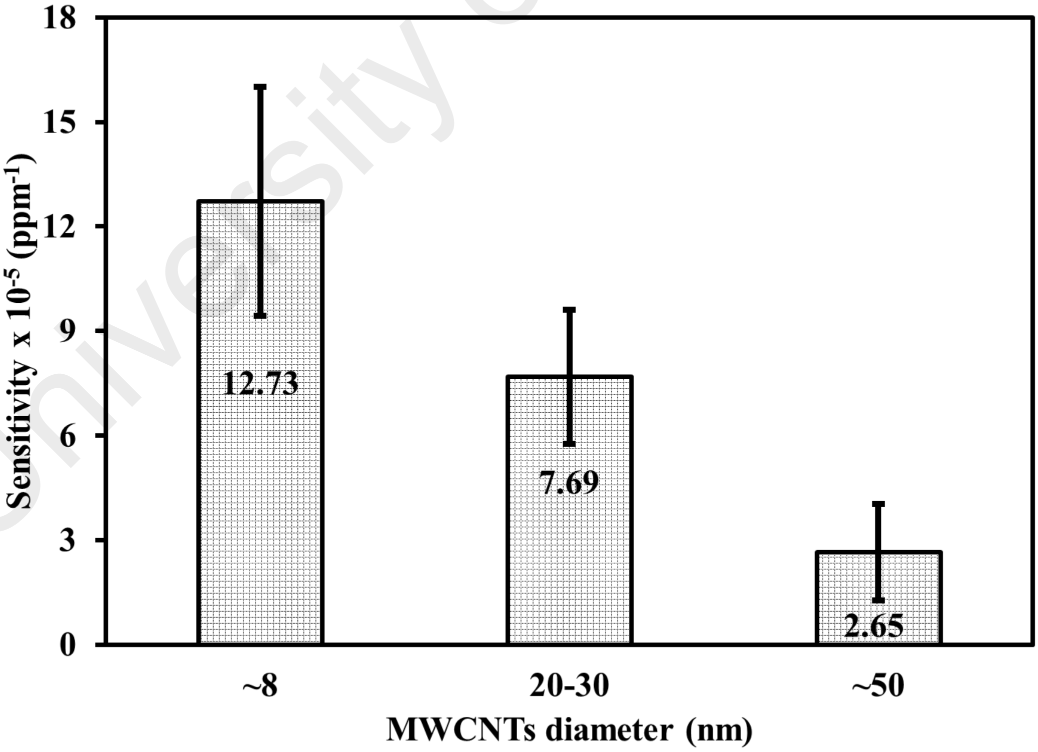

Figure 4.25: Sensitivity of toluene vapor for MWCNTs sensor with different diameters.

4.3.7 Diameter Effect of Adsorption of VOC on MWCNTs

In order to calculate the saturated response based on Langmuir adsorption isotherm, the sensor response is defined as:

$$S = \frac{\Delta R}{R_o} \tag{4.12}$$

where ΔR and R_o are ratio of resistance of the sensor after vapor exposure to that before vapor exposure. Adsorption of this vapor in this experiment can be described based on the Langmuir model as shown in Chapter 2:

$$\theta = \frac{K_L C}{1 + K_L C} \tag{4.13}$$

where θ is the fractional monolayer coverage of adsorbate molecules, C is the vapor concentration and K_L is the equilibrium constant. θ is also means (Wu et al., 2015):

$$\theta = \frac{S}{S_{max}} \tag{4.14}$$

where S_{max} is the maximum response of the sensor at saturation coverage. Place Equation 4.14 into Equation 4.13:

$$\frac{S}{S_{max}} = \frac{K_L C}{1 + K_L C} \tag{4.15}$$

The gas concentration can be expressed by:

$$C = \frac{S}{K_L(S_{max} - S)} \tag{4.16}$$

Transform Equation 4.16 into linear equation:

$$\frac{1}{S} = \frac{1}{S_{max}} + \frac{1}{S_{max} K_L C} \tag{4.17}$$

Or in other linear form:

$$\frac{C}{S}=\frac{C}{S_{max}}+\frac{1}{S_{max}K_L} \tag{4.18}$$

The saturated response was also calculated based on Freundlich model. As mentioned before, the Freundlich model is derived to model multilayer adsorption and adsorption on heterogeneous surfaces. For this experiment, the Freundlich model is described as:

$$S=K_F C^{1/n} \tag{4.19}$$

where S is sensor response ($\Delta R/R_o$), K_F is adsorption capacity, C is vapor concentration and n is the adsorption feasibility.

Another most commonly used model in the field is the Temkin model that assumed that the heat of adsorption ΔH decreases with decreasing coverage (θ), where θ is a measure of the number of occupied adsorption sites. In this case θ is proportional to S/S_{max} as shown in Equation 4.14. The Temkin model predicts a linear relationship between sensor response and the logarithm of the vapor concentration.

$$\theta = RT\ln(k_T C) \tag{4.20}$$

Replace Equation 4.14 into Equation 4.20:

$$\frac{S}{S_{max}}=RT\ln(k_T C) \tag{4.21}$$

$$S=\frac{RT}{S_{max}}\ln k_T+\frac{RT}{S_{max}}\ln C \tag{4.22}$$

$$B_T=\frac{RT}{S_{max}} \tag{4.23}$$

Substitute Equation 4.23 into Equation 4.22:

$$S=B_T\ln k_T+B_T\ln C \tag{4.24}$$

where S is sensor response, B_T is adsorption constant related with heat (J mol^{-1}), R is the universal gas constant (8.314J/mol/K), T is the temperature (300 K), k_T is the binding constant of Temkin model, S_{max} is the maximum response of the sensor at saturation coverage and C is vapor concentration (ppm).

4.3.7.1 Ethanol Vapor Sensing Behavior Based on Adsorption Models

Figure 4.26 was plotted of adsorption model based on the vapor sensing of ethanol with different diameters MWCNTs as adsorbents. It can be seen that the sensor response was initially rapid for low ethanol concentration followed by much slower response rate at high ethanol concentration. Every parameter for these models were calculated and listed in Table 4.2 based on linear plots shown in Figures B1, C1 and D1 for Langmuir, Freundlich and Temkin model, respectively.

From Langmuir model calculation, the equilibrium constant or K_L for the ~8, 20-30 and ~50 nm was estimated as 2.42×10^{-4}, 2.61×10^{-4} and 3.87×10^{-4}, respectively. It was found that, the lowest diameter MWCNTs has the highest maximum sensing response at saturation coverage (S_{max}) followed by the moderate diameter and lastly the biggest diameter.

As listed in Table 4.2, ~8 nm has higher value of adsorption capacity (K_F), followed by 20-30 nm and finally ~50 nm. Similar trend was observed for the sensor response versus concentration results shown in Figure 4.26. Based on Equation 4.19, the adsorption is considered good if value of n is in the range of 2-10 and the adsorption was moderately difficult if value of n is in the range of 1-2 (Sun et al., 2013). So, it can be concluded that the adsorption for ~8 nm and 20-30 nm were moderately difficult while the adsorption was considered as good for ~50 nm.

The Temkin model was represented by linear plot of sensor response to natural logarithm of the ethanol vapor concentration as shown in Figure D1. The constants involved (B_T and k_T) were determined from the slope and intercept of linear equation for Temkin model (Equation 4.24) and were summarized in Table 4.2. The highest value of adsorption constant related with heat, B_T for ~8 nm indicated a strong interaction between the MWCNTs and the ethanol vapor compared to other diameters MWCNTs. This might be due the lowest diameter have the strong van der Waals forces towards the walls which will coincidently attracted the ethanol vapor to temporarily bound at the surface of MWCNTs.

The Langmuir model was fitted by plotting the sensor response over concentration as a function of the concentration which shown in Figure B1 gave correlation coefficient, R^2 more than 0.872. Others fitted models which were Freundlich and Temkin gaves R^2 value > 0.920 and > 0.887, respectively. It can be concluded that the Freundlich model gave good fitting with the adsorption of ethanol by different diameters of MWCNTs compared to other fitting models.

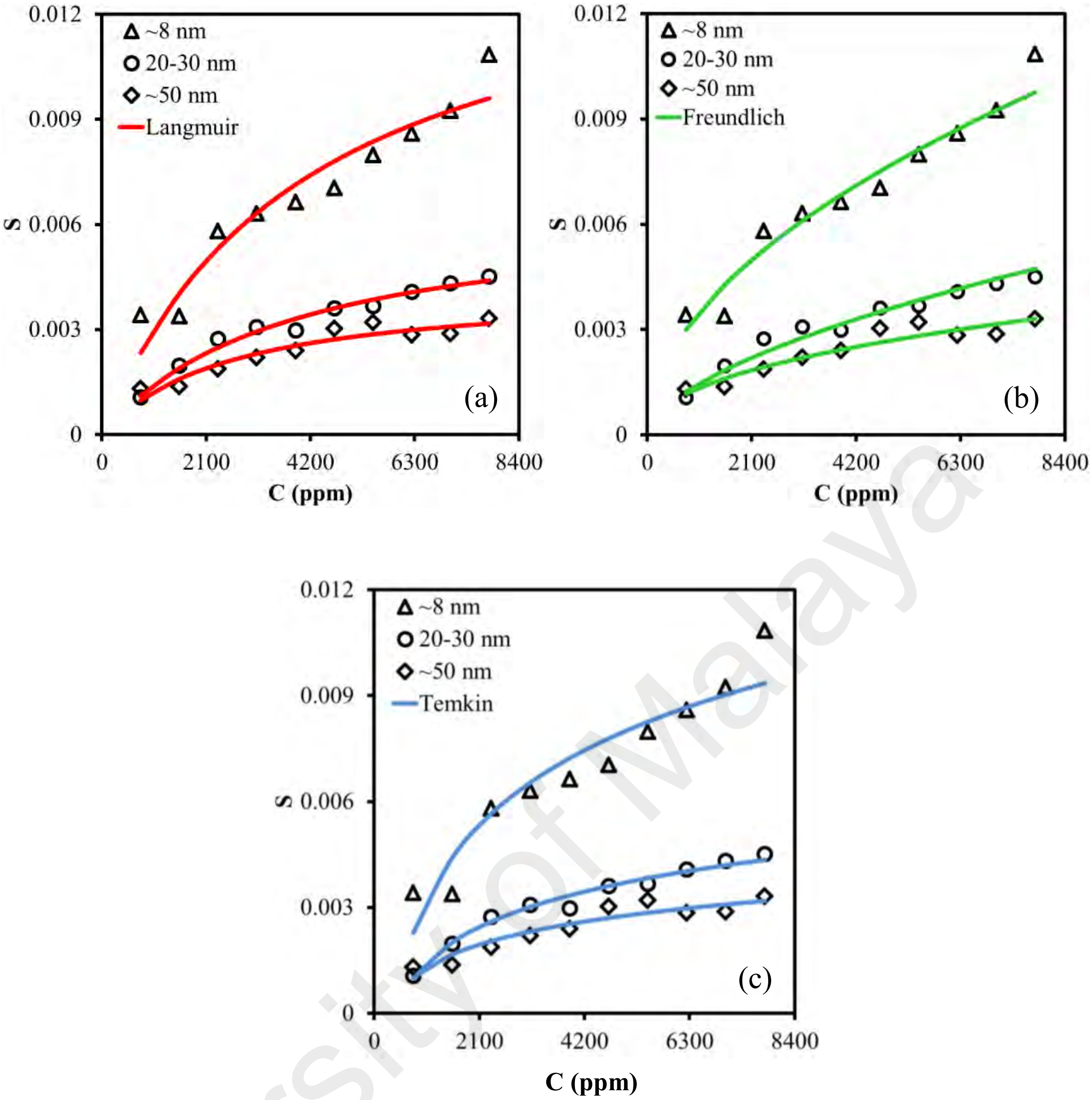

Figure 4.26: (a) Langmuir, (b) Freundlich and (c) Temkin model analyses of ethanol vapor with different diameters MWCNTs.

Table 4.2: Langmuir, Freundlich and Temkin models parameters for the vapor sensing of ethanol by different diameters MWCNTs.

Langmuir constants:	K_L (ppm^{-1})	S_{max}	R^2
~8 nm	2.42×10^{-4}	14.68×10^{-3}	0.872
20-30 nm	2.61×10^{-4}	6.56×10^{-3}	0.970
~50 nm	3.87×10^{-4}	4.22×10^{-3}	0.932
Freundlich constants:	K_F	n	R^2
~8 nm	9.89×10^{-5}	1.95	0.927
20-30 nm	6.04×10^{-5}	1.71	0.920
~50 nm	2.50×10^{-5}	2.24	0.959
Temkin constants:	B_T (J mol^{-1})	k_T	R^2
~8 nm	3.07×10^{-3}	2.70×10^{-3}	0.889
20-30 nm	1.45×10^{-3}	2.55×10^{-3}	0.978
~50 nm	0.94×10^{-3}	3.75×10^{-3}	0.887

4.3.7.2 Toluene vapor sensing based on adsorption models

Figure 4.27 presents the Langmuir and Freundlich models of toluene vapor on MWCNTs at 300 K as a relationship between the sensor response of MWCNTs ($\Delta R/R_o$) and the concentration of toluene vapor (ppm) at different diameters of MWCNTs. From the plots, the sensor response for every MWCNTs diameter increased with concentration. The linearized Langmuir plots for toluene vapor with different diameters are given in the Figure E1 while for linearized Freundlich plots are plotted in the Figure F1. Table 4.3 summarized the coefficients of the Langmuir and Freundlich models for different diameters MWCNTs.

From the slope and the intercept of the linear fitted line in Figure E1, K_L were estimated to be 5.1×10^{-4}, 1.8×10^{-4}, 4.6×10^{-4} ppm^{-1} and S_{max} were estimated to be 10.1×10^{-3}, 8×10^{-3}, 2.3×10^{-3} for MWCNTs with diameter ~8, 20-30 and ~50 nm, respectively. It can be seen that the lowest diameters (~8 nm) have the highest maximum response of the sensor at saturation coverage, S_{max} compared to other two diameters. This means that ~8 nm has the highest sensitivity compared to larger diameter. The reason that ~8 nm has high maximum response is most possibly related with the fact that it has the highest specific surface area.

For Freundlich models, the parameters as K_F and n which obtained from slope and intercept for graph plotted in Figure E1. It can be noticed that value for K_F is in the range of ~8 > 20-30 > ~50 nm which also related with specific surface area of MWCNTs. The n value was used as indicator for feasibility of the adsorption. MWCNTs with ~8 nm diameter gave n value of 2.11, which was between 2 and 10, indicating good adsorption. MWCNTs with diameter 20-30 nm and ~50 nm gave n values of 1.48 and 1.68, respectively, which was between 1 and 2, indicating moderately difficult adsorption. This means that MWCNTs with diameter ~8 nm was good adsorption compared to 20-30 nm and ~50 nm.

Based on linear plot of Temkin models in Figure G1, the Temkin adsorption curves relating toluene sensor response can be given as $S = 2.12 \times 10^{-3} \ln(5.77 \times 10^{-3} C)$, $S = 1.29 \times 10^{-3}\, ln(3.03 \times 10^{-3} C)$ and $S = 0.48 \times 10^{-3}\, ln(5.72 \times 10^{-3} C)$ for MWCNTs with diameters ~8, 20-30 and ~50 nm, respectively. The same observation was found for B_T value as ethanol vapor for toluene adsorption which it value was high for the lowest diameter MWCNTs.

The lower determination coefficients or R^2 of the Langmuir and Temkin suggested that the model data do not fit for both models. The higher determination coefficients, R^2 (> 0.757) of the Freundlich equation suggested that the Freundlich equation can be used to fit the experimental data and evaluate the adsorption capacity and adsorption feasibility of the three adsorbents. The results also indicate that the sensor response of toluene by the three different diameters MWCNTs takes place in a multilayer adsorption pattern.

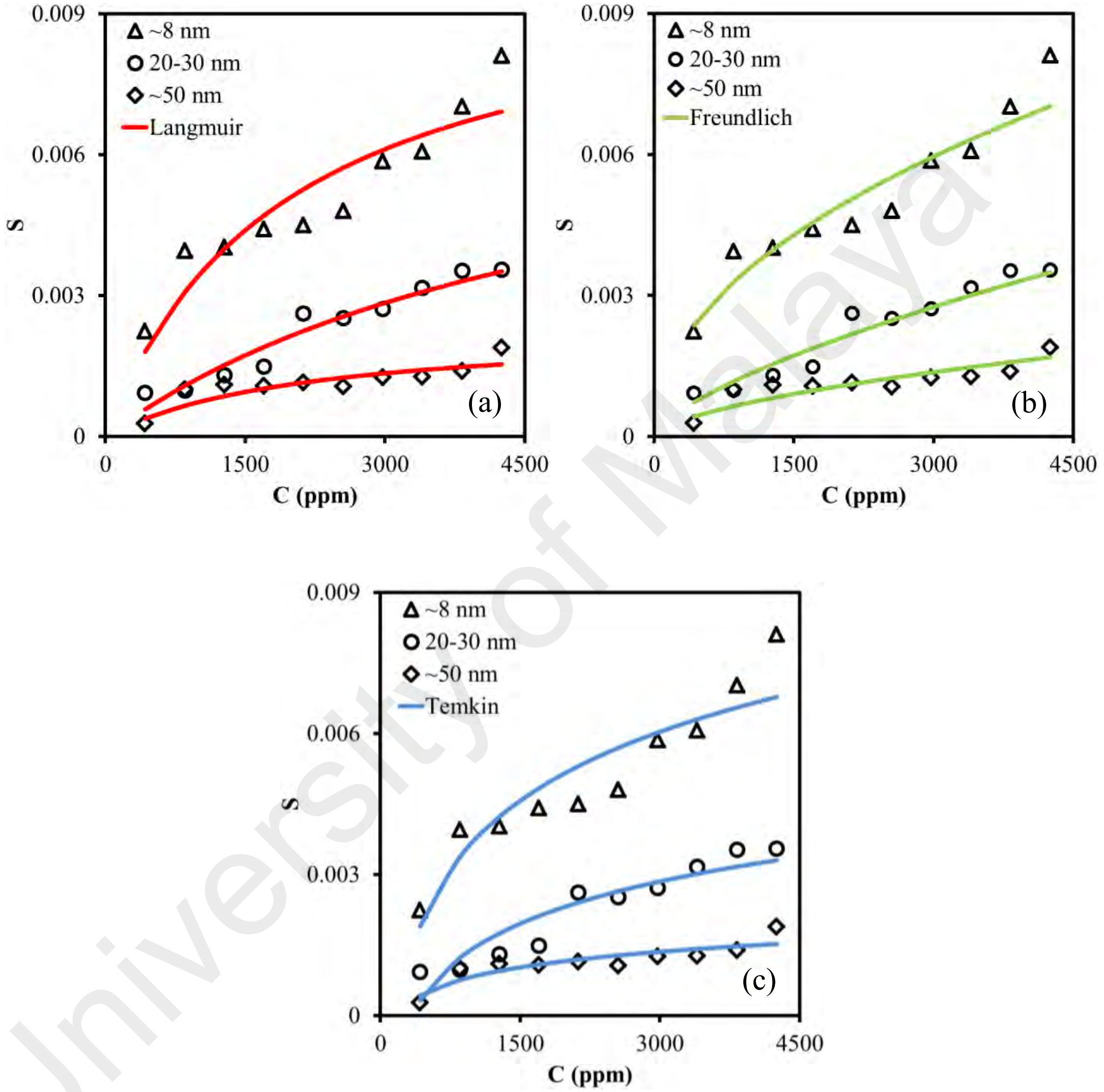

Figure 4.27: (a) Langmuir, (b) Freundlich and (c) Temkin model analyses of toluene vapor with different diameters MWCNTs.

Table 4.3: Langmuir, Freundlich and Temkin models parameters for the vapor sensing of toluene by different diameters MWCNTs.

Langmuir constants:	K_L (ppm^{-1})	S_{max}	R^2
~8 nm	5.14 x 10^{-4}	10.09 x 10^{-3}	0.837
20-30 nm	1.83 x 10^{-4}	8.03 x 10^{-3}	0.547
~50 nm	4.64 x 10^{-4}	2.32 x 10^{-3}	0.734
Freundlich constants:	K_F	n	R^2
~8 nm	13.50 x 10^{-5}	2.11	0.919
20-30 nm	1.21 x 10^{-5}	1.48	0.912
~50 nm	1.18 x 10^{-5}	1.68	0.757
Temkin constants:	B_T (J mol^{-1})	k_T	R^2
~8 nm	2.12 x 10^{-3}	5.77 x 10^{-3}	0.838
20-30 nm	1.29 x 10^{-3}	3.03 x 10^{-3}	0.861
~50 nm	0.48 x 10^{-3}	5.72 x 10^{-3}	0.771

From the ethanol and toluene sensing results, it can be concluded that the small diameter have the excellent properties compared to other diameters. This result was related with specific surface area and initial resistivity of the samples. Also, this result can be related with some parameters discussed earlier in Chapter 3. Table 4.4 shows summary of adsorption equilibrium and their parameters values obtained from Chapter 3. It can be seen from Langmuir model, value of maximum monolayer capacity, q_m of MWCNTs which indicated the theoretical limit of adsorption capacity for sometimes are in the range of ~8 > 20-30 > ~50 nm. Other fitted model which known as Freundlich showed that k_F value which represents adsorption capacity are also in the sequence of ~8 > 20-30 > ~50 nm.

Table 4.4: Summary of adsorption equilibrium and their parameters obtained from Table 3.2 and Table 3.3 in Chapter 3.

Adsorption parameters	MWCNTs diameter (nm)		
	~8	20-30	~50
Langmuir model:			
q_m (mg/g)	222.2	68.5	49.3
k_L (L/mg)	2.5	3.2	0.4
R_L	0.04	0.03	0.22
R^2	0.961	0.974	0.805
Freundlich model:			
k_F (mg/g)	146.6	54.1	19.7
n	6.7	9.0	3.4
R^2	0.854	0.663	0.536

4.3.8 Effect of ZnO Decorated MWCNTs towards VOC

In an attempt to enhance the performance of fabricated vapor sensor, method such as decorated MWCNTs with metal oxide was used. As mentioned earlier in introduction, metal oxide based sensor have good performance. In this experiment, ZnO was chosen as oxide materials to be decorated with MWCNTs.

4.3.8.1 Ethanol vapor

The normalized resistance of sensors based on pristine MWCNTs and difference weight percent of ZnO decorated MWCNTs as a sensor operating at room temperature are displayed in Figure 4.28. It can be observed, when vapor is released (VOC injected) into test chamber, response time is around 8 s while when vapour is removed, the response decrease quickly with a recovery time ranging from 27-50 s depending on concentration of vapor. The interaction of ethanol with ZnO decorated MWCNTs can be described with following equation (Yang et al., 2009):

$$CH_3CH_2OH_{(adsorbed)} + 6O_{(adsorbed)}^- \rightarrow 2CO_2 + 3H_2O + 6e^- \qquad (4.25)$$

The peak normalized resistances of sensor decorate with ZnO displays to increase as the ZnO content increased. The responses of the 0.036 mol % ZnO decorated MWCNTs is higher than that of pristine MWCNTs by around 2.8 times at ethanol 7804 ppm concentration. From the results, it can be concluded the introduction of ZnO with MWCNTs have been successfully improved the sensor response for ethanol vapor.

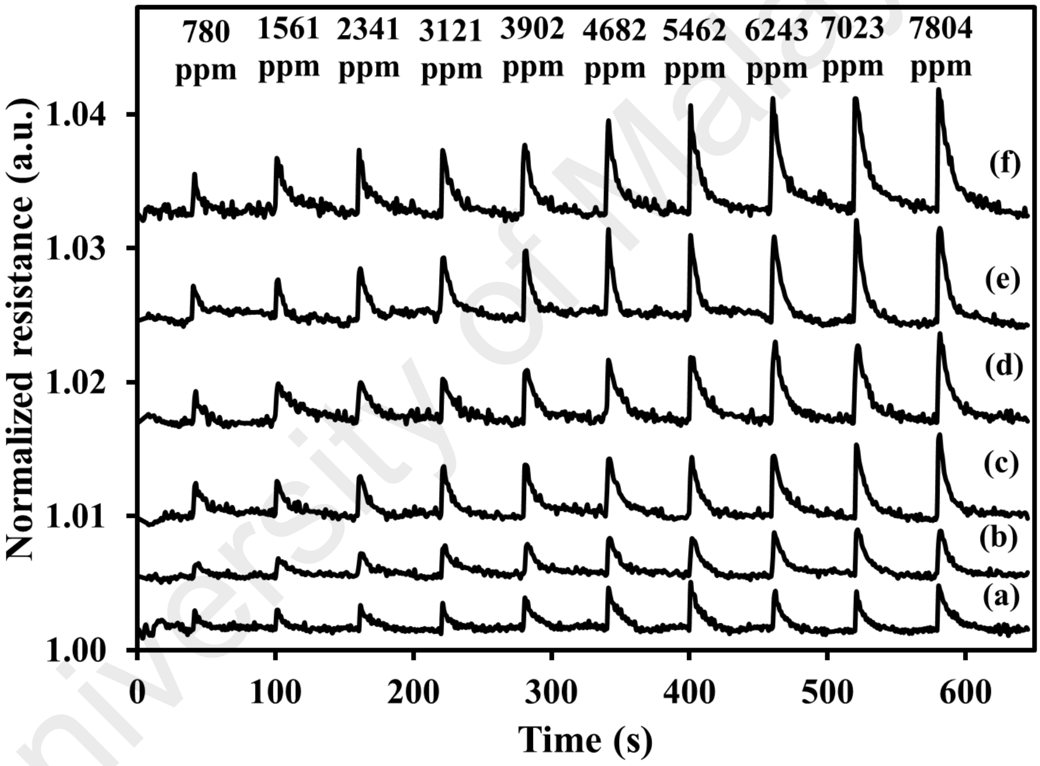

Figure 4.28: Normalized resistance for fabricated ethanol sensor in the range 780 to 7804 ppm with different concentrations of MWCNTs decorated ZnO: (a) 0 mol %, (b) 0.002 mol %, (c) 0.006 mol %, (d) 0.007 mol %, (e) 0.032 mol % and (f) 0.036 mol % samples.

The relationship between response and ethanol vapor concentration for MWCNTs and ZnO decorated MWCNTs sensor is displayed in Figure 4.29. From the graph, it can be concluded a good linear dependency between sensor response and ethanol vapor concentration. All samples exhibit no significant sign to reach saturation point indicating these samples can be used for high detection limit of ethanol vapor.

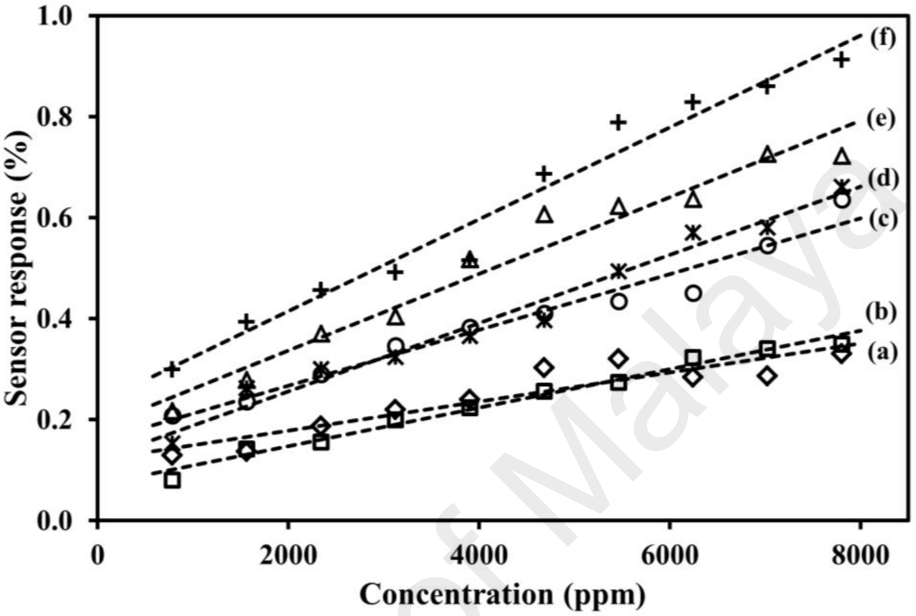

Figure 4.29: Sensor response to different concentrations of ethanol vapor for different MWCNTs decorated ZnO: (a) 0 mol %, (b) 0.002 mol %, (c) 0.006 mol %, (d) 0.007 mol %, (e) 0.032 mol % and (f) 0.036 mol % samples.

The response of the sensors increased with ethanol vapor concentration. Similar trend was observed for pristine MWCNTs, but the response of it was much weaker which indicated that it has a much lower sensitivity compared with ZnO decorated MWCNTs sensors (Figure 4.30). The sensitivity values calculated from Equation 3.3 for pristine MWCNTs and ZnO decorated MWCNTs is plotted in Figure 4.30 indicating that addition of 0.036 mol % ZnO towards MWCNTs have improved approximately 3.2 times higher than pristine MWCNTs.

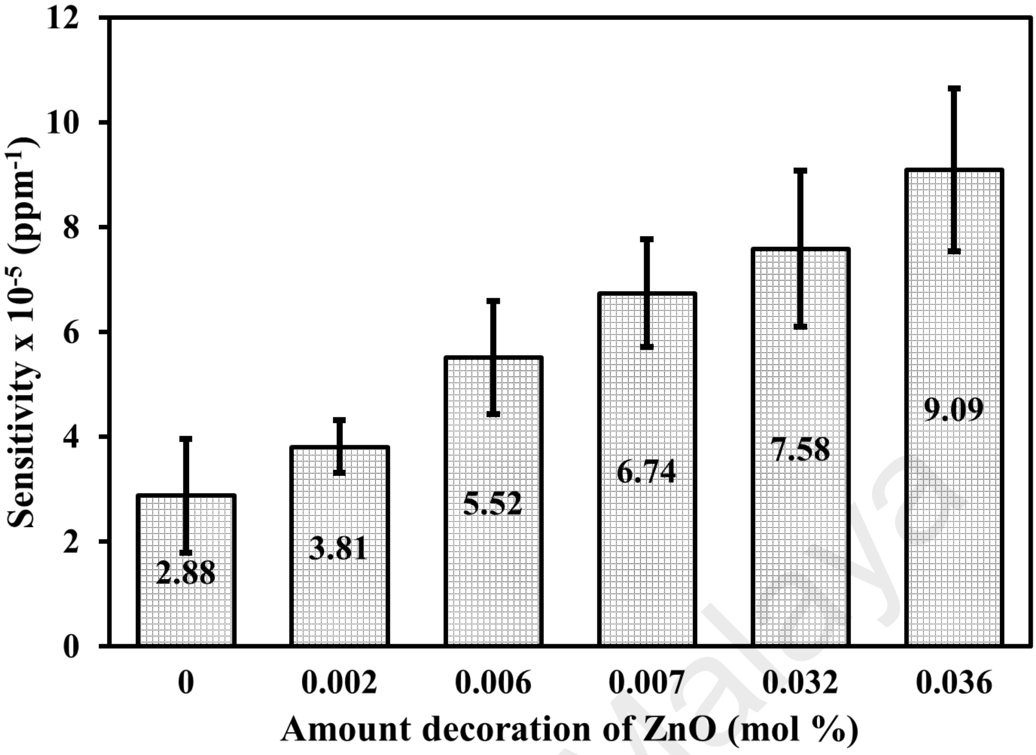

Figure 4.30: Histogram sensitivity of ethanol vapor for MWCNTs decorated with different amount of ZnO.

4.3.8.2 Toluene vapor

Figure 4.31 shows the changes in resistance at room temperature for pure MWCNTs and ZnO decorated MWCNTs were exposed to toluene vapor at various concentrations. For toluene vapor ~4253 ppm, a total change of almost 7 times in resistance of MWCNTs without and with decorated 0.032 mol % of ZnO. The sensing mechanism of MWCNTs can be demonstrated by two main features. First, is the large specific surface area of MWCNTs which give rise possibility of target vapor molecules adsorbed and reacted on the surface of MWCNTs. Secondly, it is the tubular structure of MWCNTs that can be available for transferring of oxygen molecules or target vapor from the reaction sites (Dai, 2002). Compare with pure MWCNTs, MWCNTs decorated with ZnO NPs exhibits enhanced sensitivity by doping a small amount of ZnO, which may be ascribed to main characteristics of ZnO and the deficiency of MWCNTs as a vapor sensor. The pure MWCNTs have strong sp^2 carbon-carbon bonds, which means chemically stable and hard to form strong bonding with most vapor molecule (Cui et al., 2012). Whereby the sensing mechanism of ZnO involved by the catch and remove procedure of electrons on surface of ZnO (Cheng et al., 2004; Prajapati & Sahay, 2011; Trinh et al., 2011). When ZnO is in air, its surface will be enclosed by oxygen molecules and later on electrons will be release from it and ionization to O_2^-, O^- and O^{2-} as a result to increase of resistance. This process of oxygen adsorption can be described in the following equations (Yang et al., 2009):

$$\mathrm{O}_{2(\mathrm{vapour})} \leftrightarrow \mathrm{O}_{2(\mathrm{adsorbed})} \tag{4.26}$$

$$\mathrm{O}_{2(\mathrm{adsorbed})} + \mathrm{e}^- \leftrightarrow O_2^-{}_{(\mathrm{adsorbed})} \tag{4.27}$$

$$O_2^{2-}{}_{(\mathrm{adsorbed})} + 2\mathrm{e}- \leftrightarrow 2O^{2-}{}_{(\mathrm{lattice})} \tag{4.28}$$

Thus, as the decorated of ZnO, the sensitivity of MWCNTs enhanced gradually. Interaction of toluene sensing with ZnO decorated MWCNTs is described as in following equations:

$$\mathrm{C_6H_5CH_3} + \mathrm{O_2}- \rightarrow \mathrm{C_6H_5CHO^-} + \mathrm{H_2O} + \mathrm{e}^- \tag{4.29}$$

$$\mathrm{C_6H_5CHO^-} \rightarrow \mathrm{C_6H_5CHO} + \mathrm{e} \tag{4.30}$$

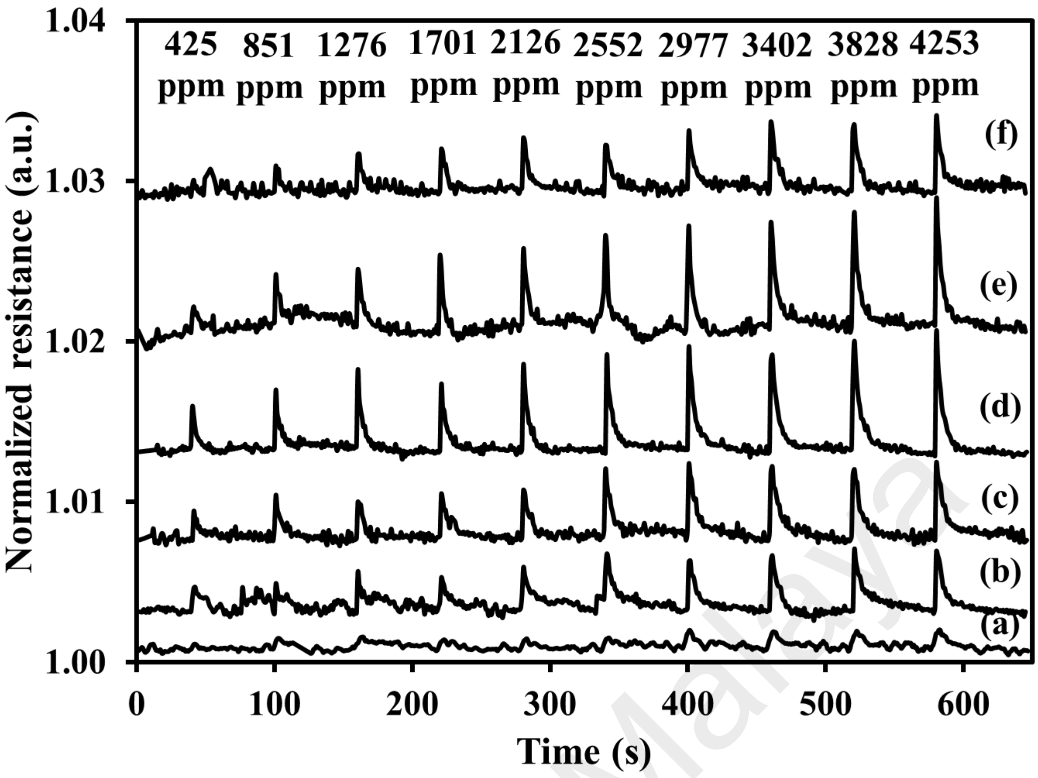

Figure 4.31: Normalized resistance for fabricated toluene sensor in the range 425 to 4253 ppm with different concentrations of ZnO; (a) 0 mol %, (b) 0.002 mol %, (c) 0.006 mol %, (d) 0.007 mol %, (e) 0.032 mol % and (f) 0.036 mol % decorated MWCNTs samples.

From Figure 4.32, the gradient of sensor response versus toluene concentration increased with increment of ZnO amount suggested the more favorable samples to detect ethanol are 0.032 mol % ZnO decorated MWCNTs. The increase in sensor responses varied linearly on vapor concentrations in the range from 425 to 4253 ppm for all samples, which further confirms the existent of MWCNTs and ZnO decorated MWCNTs structures can be used as promising materials for toluene vapor sensors.

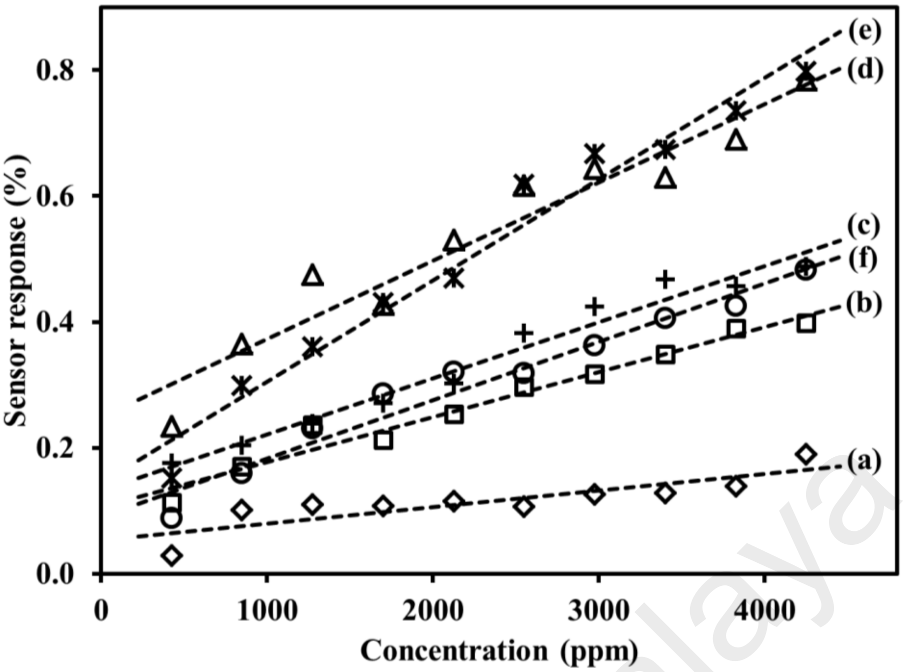

Figure 4.32: Sensor response to different concentrations of toluene vapor for different MWCNTs doped ZnO: (a) 0 mol %, (b) 0.002 mol %, (c) 0.006 mol %, (d) 0.007 mol %, (e) 0.032 mol % and (f) 0.036 mol % samples.

Figure 4.30 and Figure 4.33 show the ensitivity of MWCNTs decorated with different amount of ZnO NPs to ethanol and toluene, respectively, at room temperature. From the graphs, the sensitivity of toluene is much higher compared to ethanol indicating a good selectivity of MWCNTs decorated ZnO towards toluene vapor. This may be due to characteristics of materials. In general, the mechanism and activities of adsorbed oxygen on surface were not identical in different materials. For a certain materials, some vapor has optimum working temperatures (Qi et al., 2009). As a result, the sensitivities of different vapor are unpredictable for the same temperature which in order words represents the selectivity behavior.

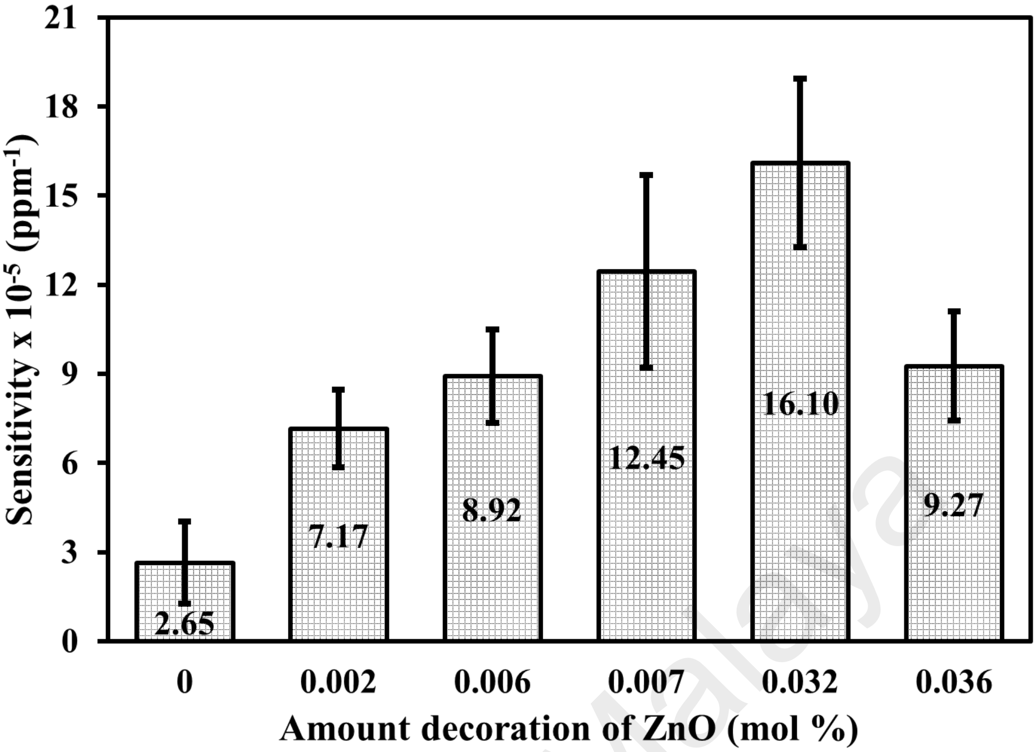

Figure 4.33: Histogram sensitivity of toluene vapor for MWCNTs decorated with different amount of ZnO.

CHAPTER 5: CONCLUSIONS AND SUGGESTIONS FOR FUTURE WORK

5.1 Conclusions

It can be concluded that the different diameters of MWCNTs did have effect on the adsorption behavior of R6G in aqueous solutions. The lowest diameter MWCNTs has the highest removal efficiency. It was found that the Langmuir model was best fitted to the experimental data obtained. The model assumed monolayer adsorption on homogeneous surface without interaction between adsorbed MWCNTs and the adsorptions of all molecules have equal activation energy. Once the monolayer coverage was achieved, the adsorption was no longer influenced by the R6G molecules transport behavior and lessen the affinity of the R6G on MWCNTs. From kinetic adsorption model, the results were not well fitted to the pseudo-first-order since the large differences between experimental ($q_{e,exp}$) and calculated ($q_{e,cal}$) values of the equilibrium adsorption capacity. In contrast, the pseudo-second-order model showed good fits to the experimental data. The values of $q_{e,cal}$ also appeared to be close to the experimentally observed values of $q_{e,exp}$. These results suggest that the adsorption kinetic for this experiment followed the pseudo-second-order model.

Vapor sensor for ethanol and toluene from different diameters MWCNTs and ZnO decorated MWCNTs have been successfully fabricated and applied at room temperature. The sensitivities towards ethanol vapor in the range 780 ppm to 7803 ppm were 9.88 x 10^{-5}, 4.39 x 10^{-5} and 2.88 x 10^{-5} ppm^{-1} for MWCNTs of diameter ~8, 20-30 and ~50 nm, respectively. The sensitivities for toluene vapor in the range 425 ppm to 4253 ppm were 12.73 x 10^{-5}, 7.69 x 10^{-5} and 2.65 x 10^{-5} ppm^{-1} for MWCNTs of diameter ~8, 20-30 and ~50 nm, respectively. The results suggested that the high sensitivity with low diameters can be due to; higher effective specific surface area afforded by the MWCNTs with smaller diameter and higher conductivity with smaller diameter. It was found that the introduction of ZnO nanoparticles into the sensor increased the sensitivities of sensor from 2.88 x 10^{-5} to 9.09 x 10^{-5} ppm^{-1} with 0.036 mol % of ZnO content and 2.65 x 10^{-5} to 16.10 x 10^{-5} ppm^{-1} with 0.032 mol % of ZnO content for ethanol and toluene vapor, respectively. The sensor response of ethanol and toluene towards MWCNTs were also investigated in terms of adsorption model. It was found that both vapors were better fitted to the Freundlich model compared to Langmuir and Temkin models.

5.2 Suggestions for future work

Adsorption of R6G solution can be continued by using adsorbent which natural materials or the wastes products of industries or synthetically prepared materials such as banana peel, orange peel, rice husk, charcoal and saw dust. These types of adsorbent were as an alternative for low cost and easy to find.

The sensor experiment should be continued by using other volatile organic compounds such as methanol, acetone and benzene which frequently found in daily activities of human being. The sensor response might be increased by functionalized MWCNTs with polymer or other metal oxide to enhance the sensor properties.

REFERENCES

Adu, C. K., Sumanasekera, G. U., Pradhan, B. K., Romero, H. E., & Eklund, P. C. (2001). Carbon nanotubes: a thermoelectric nano-nose. *Chemical Physics Letters, 337*(1), 31-35.

Aharoni, C., & Ungarish, M. (1977). Kinetics of activated chemisorption. Part 2.—Theoretical models. *Journal of the Chemical Society, Faraday Transactions 1: Physical Chemistry in Condensed Phases, 73*, 456-464.

Anbia, M., & Ghaffari, A. (2009). Adsorption of phenolic compounds from aqueous solutions using carbon nanoporous adsorbent coated with polymer. *Applied Surface Science, 255*(23), 9487-9492.

Antunes, E. F., Lobo, A. O., Corat, E. J., Trava-Airoldi, V. J., Martin, A. A., & Veríssimo, C. (2006). Comparative study of first- and second-order Raman spectra of MWCNT at visible and infrared laser excitation. *Carbon, 44*(11), 2202-2211.

Aqel, A., El-Nour, K. M. M. A., Ammar, R. A. A., & Al-Warthan, A. (2012). Carbon nanotubes, science and technology part (I) structure, synthesis and characterisation. *Arabian Journal of Chemistry, 5*(1), 1-23.

Arenales Rivera, J., Perez Lopez, V., Ramos Casado, R., & Sanchez Hervas, J. M. (2016). Thermal degradation of paper industry wastes from a recovered paper mill using TGA. Characterization and gasification test. *Waste Management, 47*(Pt B), 225-235.

Arseneau, D. F. (1971). Competitive reactions in the thermal decomposition of cellulose. *Canadian Journal of Chemistry, 49*(4), 632-638.

Ashrafi, A. B. M. A., Ueta, A., Avramescu, A., Kumano, H., Suemune, I., Ok, Y.-W., & Seong, T.-Y. (2000). Growth and characterization of hypothetical zinc-blende ZnO films on GaAs(001) substrates with ZnS buffer layers. *Applied Physics Letters, 76*(5), 550-552.

Avouris, P. (2002). Carbon nanotube electronics. *Chemical Physics, 281*(2), 429-445.

Azamian, B. R., Coleman, K. S., Davis, J. J., Hanson, N., & Green, M. L. H. (2002). Directly observed covalent coupling of quantum dots to single-wall carbon nanotubes. *Chemical Communications, 44*(4), 366-367.

Azizian, S. (2004). Kinetic models of sorption: a theoretical analysis. *Journal of Colloid and Interface Science, 276*(1), 47-52.

Bacon, R. (1960). Growth, Structure, and Properties of Graphite Whiskers. *Journal of Applied Physics, 31*(2), 283-290.

Bacsa, W. S., Ugarte, D., Châtelain, A., & de Heer, W. A. (1994). High-resolution electron microscopy and inelastic light scattering of purified multishelled carbon nanotubes. *Physical Review B, 50*(20), 15473-15476.

Baker, R., Barber, M., Harris, P., Feates, F., & Waite, R. (1972). Nucleation and growth of carbon deposits from the nickel catalyzed decomposition of acetylene. *Journal of Catalysis, 26*(1), 51-62.

Balasubramanian, K., & Burghard, M. (2006). Biosensors based on carbon nanotubes. *Analytical and Bioanalytical Chemistry, 385*(3), 452-468.

Baranov, A., Bekhterev, A., Bobovich, Y. S., & Petrov, V. (1987). Interpretation of certain characteristics in Raman spectra of graphite and glassy carbon. *Optics and Spectroscopy, 62*, 1036.

Baskaran, D., Mays, J. W., & Bratcher, M. S. (2005). Noncovalent and nonspecific molecular interactions of polymers with multiwalled carbon nanotubes. *Chemistry of Materials, 17*(13), 3389-3397.

Baughman, R. H., Zakhidov, A. A., & De Heer, W. A. (2002). Carbon nanotubes-the route toward applications. *Science, 297*(5582), 787-792.

Berber, S., Kwon, Y.-K., & Tománek, D. (2000). Unusually high thermal conductivity of carbon nanotubes. *Physical Review Letters, 84*(20), 4613.

Bethune, D., Kiang, C. H., De Vries, M., Gorman, G., Savoy, R., Vazquez, J., & Beyers, R. (1993). Cobalt-catalysed growth of carbon nanotubes with single-atomic-layer walls. *Nature, 363*(6430), 605-607.

Bhat, D. (2008). Facile synthesis of ZnO nanorods by microwave irradiation of zinc–hydrazine hydrate complex. *Nanoscale Research Letters, 3*(1), 31.

Bhuiyan, M., Murakami, K., & Ota, M. (2008). On thermal stability and chemical kinetics of waste newspaper by thermogravimetric and pyrolysis analysis. *Journal of Environment and Engineering, 3*(1), 1-12.

Bilalis, P., Katsigiannopoulos, D., Avgeropoulos, A., & Sakellariou, G. (2014). Non-covalent functionalization of carbon nanotubes with polymers. *Royal Society of Chemistry Advances, 4*(6), 2911-2934.

Bommeli, F., Degiorgi, L., Wachter, P., Bacsa, W., de Heer, W. A., & Forro, L. (1996). Evidence of anisotropic metallic behaviour in the optical properties of carbon nanotubes. *Solid State Communications, 99*(7), 513-517.

Bradley, K., Gabriel, J.-C. P., Briman, M., Star, A., & Grüner, G. (2003). Charge transfer from ammonia physisorbed on nanotubes. *Physical Review Letters, 91*(21), 218301.

Bystrzejewski, M., Huczko, A., Lange, H., Gemming, T., Büchner, B., & Rümmeli, M. (2010). Dispersion and diameter separation of multi-wall carbon nanotubes in aqueous solutions. *Journal of Colloid and Interface Science, 345*(2), 138-142.

Cantalini, C., Valentini, L., Lozzi, L., Armentano, I., Kenny, J., & Santucci, S. (2003). NO_2 gas sensitivity of carbon nanotubes obtained by plasma enhanced chemical vapor deposition. *Sensors and Actuators B: Chemical, 93*(1), 333-337.

Cao, A., Xu, C., Liang, J., Wu, D., & Wei, B. (2001). X-ray diffraction characterization on the alignment degree of carbon nanotubes. *Chemical Physics Letters, 344*(1), 13-17.

Carbon Nanotubes - Price - Chinese Academy of Sciences, Chengdu Organic Chemistry Co., Ltd. Retrieved from http://www.timesnano.com/en/article.php?prt=4,31,105

Catti, M., Noel, Y., & Dovesi, R. (2003). Full piezoelectric tensors of wurtzite and zinc blende ZnO and ZnS by first-principles calculations. *Journal of Physics and Chemistry of Solids, 64*(11), 2183-2190.

Chang, H., Lee, J. D., Lee, S. M., & Lee, Y. H. (2001). Adsorption of NH_3 and NO_2 molecules on carbon nanotubes. *Applied Physics Letters, 79*(23), 3863-3865.

Charlier, J.-C., & Issi, J.-P. (1998). Electronic structure and quantum transport in carbon nanotubes. *Applied Physics A: Materials Science & Processing, 67*(1), 79-87.

Chen, C., & Wang, X. (2006). Adsorption of Ni (II) from aqueous solution using oxidized multiwall carbon nanotubes. *Industrial & Engineering Chemistry Research, 45*(26), 9144-9149.

Chen, R. J., Franklin, N. R., Kong, J., Cao, J., Tombler, T. W., Zhang, Y., & Dai, H. (2001). Molecular photodesorption from single-walled carbon nanotubes. *Applied Physics Letters, 79*(14), 2258-2260.

Chen, Y.-C., & Lo, S.-L. (2011). Effects of operational conditions of microwave-assisted synthesis on morphology and photocatalytic capability of zinc oxide. *Chemical Engineering Journal, 170*(2), 411-418.

Chen, Y., Meng, F., Li, M., & Liu, J. (2009). Novel capacitive sensor: Fabrication from carbon nanotube arrays and sensing property characterization. *Sensors and Actuators B: Chemical, 140*(2), 396-401.

Cheng, X., Zhao, H., Huo, L., Gao, S., & Zhao, J. (2004). ZnO nanoparticulate thin film: preparation, characterization and gas-sensing property. *Sensors and Actuators B: Chemical, 102*(2), 248-252.

Chichvarina, O., Herng, T., Phuah, K., Xiao, W., Bao, N., Feng, Y., & Ding, J. (2015). Stable zinc-blende ZnO thin films: formation and physical properties. *Journal of Materials Science, 50*(1), 28-33.

Coleman, J., Curran, S., Dalton, A., Davey, A., McCarthy, B., Blau, W., & Barklie, R. (1998). Percolation-dominated conductivity in a conjugated-polymer-carbon-nanotube composite. *Physical Review B, 58*(12), R7492.

Collins, P. G., & Avouris, P. (2000). Nanotubes for electronics. *Science American, 283*(6), 62-69.

Collins, P. G., Bradley, K., Ishigami, M., & Zettl, A. (2000). Extreme oxygen sensitivity of electronic properties of carbon nanotubes. *Science, 287*(5459), 1801-1804.

Collins, P. G., Hersam, M., Arnold, M., Martel, R., & Avouris, P. (2001). Current saturation and electrical breakdown in multiwalled carbon nanotubes. *Physical Review Letters, 86*(14), 3128.

Cui, S., Pu, H., Lu, G., Wen, Z., Mattson, E. C., Hirschmugl, C., Gajdardziska-Josifovska, M., Weinert, M., & Chen, J. (2012). Fast and selective room-temperature ammonia sensors using silver nanocrystal-functionalized carbon nanotubes. *American Chemical Society Applied Materials & Interfaces, 4*(9), 4898-4904.

Dąbrowski, A. (2001). Adsorption—from theory to practice. *Advances in Colloid And Interface Science, 93*(1), 135-224.

Dai, H. (2002). Carbon nanotubes: synthesis, integration, and properties. *Accounts of Chemical Research, 35*(12), 1035-1044.

Dare-Doyen, S., Doizi, D., Guilbaud, P., Djedaini-Pilard, F., Perly, B., & Millié, P. (2003). Dimerization of xanthene dyes in water: Experimental studies and molecular dynamic simulations. *The Journal of Physical Chemistry B, 107*(50), 13803-13812.

De Heer, W. A., Bacsa, W., Chatelain, A., Gerfin, T., & Humphrey-Baker, R. (1995). Aligned carbon nanotube films: production and optical and electronic properties. *Science, 268*(5212), 845.

Di Crescenzo, A., Ettorre, V., & Fontana, A. (2014). Non-covalent and reversible functionalization of carbon nanotubes. *Beilstein Journal of Nanotechnology, 5*, 1675.

Dresselhaus, M., Dresselhaus, G., & Jorio, A. (2004). Unusual properties and structure of carbon nanotubes. *Annual Review of Materials Research, 34*, 247-278.

Dresselhaus, M. S., Dresselhaus, G., & Eklund, P. C. (1996). *Science of fullerenes and carbon nanotubes: their properties and applications*: Academic press.

Dresselhaus, M. S., Dresselhaus, G., Saito, R., & Jorio, A. (2005). Raman spectroscopy of carbon nanotubes. *Physics reports, 409*(2), 47-99.

Du, Y., Hao, C., & Wang, G. (2008). Preparation of floral-patterned ZnO/MWCNT heterogeneity structure using microwave irradiation heating method. *Materials Letters, 62*(1), 30-32.

Dujardin, E., Ebbesen, T. W., Krishnan, A., & Treacy, M. M. (1998). Purification of single-shell nanotubes. *Advanced Materials, 10*(8), 611-613.

Dükkancı, M., Gündüz, G., Yılmaz, S., & Prihod'ko, R. (2010). Heterogeneous Fenton-like degradation of Rhodamine 6G in water using CuFeZSM-5 zeolite catalyst prepared by hydrothermal synthesis. *Journal of Hazardous Materials, 181*(1), 343-350.

Dyke, C. A., & Tour, J. M. (2003). Solvent-free functionalization of carbon nanotubes. *Journal of The American Chemical Society, 125*(5), 1156-1157.

Eklund, P., Holden, J., & Jishi, R. (1995). Vibrational modes of carbon nanotubes; spectroscopy and theory. *Carbon, 33*(7), 959-972.

Elking, M. D., He, G., & Xu, Z. (1996). Molecular orientation of submonolayer rhodamine-6G on quartz substrates: A comparative study using reflection and transmission UV-Vis spectroscopy. *The Journal of Chemical Physics, 105*(15), 6565-6573.

Falvo, M. R., Clary, G., Taylor Ii, R., & Chi, V. (1997). Bending and buckling of carbon nanotubes under large strain. *Nature, 389*(6651), 582.

Fang, B., Zhang, C., Zhang, W., & Wang, G. (2009). A novel hydrazine electrochemical sensor based on a carbon nanotube-wired ZnO nanoflower-modified electrode. *Electrochimica Acta, 55*(1), 178-182.

Fischer, J. E. (2006). Carbon nanotubes: structure and properties. *Nanotubes and Nanofibers, 1*, 1.

Freundlich, H. (1906). Over the adsorption in solution. *The Journal of Physical Chemistry, 57*(385471), 1100-1107.

Fujigaya, T., & Nakashima, N. (2015). Non-covalent polymer wrapping of carbon nanotubes and the role of wrapped polymers as functional dispersants. *Science and Technology of Advanced Materials, 16*(2), 024802.

Gao, P. X., & Wang, Z. L. (2005). High-yield synthesis of single-crystal nanosprings of ZnO. *Small, 1*(10), 945-949.

Ghaedi, M., Haghdoust, S., Kokhdan, S. N., Mihandoost, A., Sahraie, R., & Daneshfar, A. (2012). Comparison of activated carbon, multiwalled carbon nanotubes, and cadmium hydroxide nanowire loaded on activated carbon as adsorbents for kinetic and equilibrium study of removal of Safranine O. *Spectroscopy Letters, 45*(7), 500-510.

Gonzalez, G., Albano, C., Herman, V., Boyer, I., Monsalve, A., & Brito, J. (2012). Nanocomposite building blocks of TiO_2–$MWCNT_f$ and ZrO_2–$MWCNT_f$. *Materials Characterization, 64*, 96-106.

Grüneis, A., Saito, R., Kimura, T., Cançado, L., Pimenta, M., Jorio, A., Souza Filho, A., Dresselhaus, G., & Dresselhaus, M. (2002). Determination of two-dimensional phonon dispersion relation of graphite by Raman spectroscopy. *Physical Review B, 65*(15), 155405.

Guldi, D. M., & Martín, N. (2010). *Carbon nanotubes and related structures: synthesis, characterization, functionalization, and applications*: John Wiley & Sons.

Gupta, V. K., Kumar, R., Nayak, A., Saleh, T. A., & Barakat, M. (2013). Adsorptive removal of dyes from aqueous solution onto carbon nanotubes: a review. *Advances in Colloid and Interface Science, 193*, 24-34.

Habouti, S., Mátéfi-Tempfli, M., Solterbeck, C.-H., Es-Souni, M., Mátéfi-Tempfli, S., & Es-Souni, M. (2011). Self-standing corrugated Ag and Au-nanorods for plasmonic applications. *Journal of Materials Chemistry, 21*(17), 6269-6273.

Hall, K. R., Eagleton, L. C., Acrivos, A., & Vermeulen, T. (1966). Pore-and solid-diffusion kinetics in fixed-bed adsorption under constant-pattern conditions. *Industrial & Engineering Chemistry Fundamentals, 5*(2), 212-223.

Haremza, J. M., Hahn, M. A., Krauss, T. D., Chen, S., & Calcines, J. (2002). Attachment of single CdSe nanocrystals to individual single-walled carbon nanotubes. *Nano Letters, 2*(11), 1253-1258.

Hildebrandt, P., & Stockburger, M. (1984). Surface-enhanced resonance Raman spectroscopy of Rhodamine 6G adsorbed on colloidal silver. *The Journal of Physical Chemistry, 88*(24), 5935-5944.

Hilding, J., Grulke, E. A., Sinnott, S. B., Qian, D., Andrews, R., & Jagtoyen, M. (2001). Sorption of butane on carbon multiwall nanotubes at room temperature. *Langmuir, 17*(24), 7540-7544.

Hiura, H., Ebbesen, T., Tanigaki, K., & Takahashi, H. (1993). Raman studies of carbon nanotubes. *Chemical Physics Letters, 202*(6), 509-512.

Hiura, H., Ebbesen, T. W., & Tanigaki, K. (1995). Opening and purification of carbon nanotubes in high yields. *Advanced materials, 7*(3), 275-276.

Holzinger, M., Abraham, J., Whelan, P., Graupner, R., Ley, L., Hennrich, F., Kappes, M., & Hirsch, A. (2003). Functionalization of single-walled carbon nanotubes with (R-) oxycarbonyl nitrenes. *Journal of the American Chemical Society, 125*(28), 8566-8580.

Holzinger, M., Vostrowsky, O., Hirsch, A., Hennrich, F., Kappes, M., Weiss, R., & Jellen, F. (2001). Sidewall functionalization of carbon nanotubes. *Angewandte Chemie International Edition, 40*(21), 4002-4005.

Hone, J., Llaguno, M., Biercuk, M., Johnson, A., Batlogg, B., Benes, Z., & Fischer, J. (2002). Thermal properties of carbon nanotubes and nanotube-based materials. *Applied Physics A: Materials Science & Processing, 74*(3), 339-343.

Hong, S., & Myung, S. (2007). Nanotube Electronics: A flexible approach to mobility. *Nature Nanotechnology, 2*(4), 207-208.

Hu, C., & Hu, S. (2009). Carbon nanotube-based electrochemical sensors: principles and applications in biomedical systems. *Journal of Sensors, 2009*.

Huang, J., Chen, S., Wang, Z., Kempa, K., Wang, Y., Jo, S., Chen, G., Dresselhaus, M., & Ren, Z. (2006). Superplastic carbon nanotubes. *Nature, 439*(7074), 281-281.

Huang, M. H., Mao, S., Feick, H., Yan, H., Wu, Y., Kind, H., Weber, E., Russo, R., & Yang, P. (2001). Room-temperature ultraviolet nanowire nanolasers. *Science, 292*(5523), 1897-1899.

Huaxiang, F., Ling, Y., & Xide, X. (1994). Optical properties for graphene microtubules of different geometries. *Solid State Communications, 91*(3), 191-194.

Iijima, S. (1991). Helical microtubules of graphitic carbon. *Nature, 354*(6348), 56.

Iijima, S., & Ichihashi, T. (1993). Single-shell carbon nanotubes of 1-nm diameter. *Nature, 363*(6430), 603-605.

Islam, M., Rojas, E., Bergey, D., Johnson, A., & Yodh, A. (2003). High weight fraction surfactant solubilization of single-wall carbon nanotubes in water. *Nano Letters, 3*(2), 269-273.

Izadi, N., Rashidi, A. M., Golzardi, S., Talaei, Z., Mahjoub, A. R., & Aghili, M. H. (2012). Hydrogen sulfide sensing properties of multi walled carbon nanotubes. *Ceramics International, 38*(1), 65-75.

Jensen, K., Mickelson, W., Kis, A., & Zettl, A. (2007). Buckling and kinking force measurements on individual multiwalled carbon nanotubes. *Physical Review B, 76*(19), 195436.

Jensen, L., & Schatz, G. C. (2006). Resonance Raman scattering of rhodamine 6G as calculated using time-dependent density functional theory. *The Journal of Physical Chemistry A, 110*(18), 5973-5977.

Jiang, L., & Gao, L. (2005). Fabrication and characterization of ZnO-coated multi-walled carbon nanotubes with enhanced photocatalytic activity. *Materials Chemistry and Physics, 91*(2), 313-316.

Jimenez-Cadena, G., Riu, J., & Rius, F. X. (2007). Gas sensors based on nanostructured materials. *The Analyst, 132*(11), 1083-1099.

Ju, S., Facchetti, A., Xuan, Y., Liu, J., Ishikawa, F., Ye, P., Zhou, C., Marks, T. J., & Janes, D. B. (2007). Fabrication of fully transparent nanowire transistors for transparent and flexible electronics. *Nature Nanotechnology, 2*(6), 378-384.

Kang, Y., & Taton, T. A. (2003). Micelle-encapsulated carbon nanotubes: a route to nanotube composites. *Journal of the American Chemical Society, 125*(19), 5650-5651.

Kannan, N., & Sundaram, M. M. (2001). Kinetics and mechanism of removal of methylene blue by adsorption on various carbons—a comparative study. *Dyes and pigments, 51*(1), 25-40.

Kathalingam, A., Park, H.-C., Kim, S.-D., Kim, H.-S., Velumani, S., & Mahalingam, T. (2015). Synthesis of ZnO nanorods using different precursor solutions and their two terminal device characterization. *Journal of Materials Science: Materials in Electronics, 26*(8), 5724-5734.

Kim, D. S., Lee, T., & Geckeler, K. E. (2006a). Hole-Doped Single-Walled Carbon Nanotubes: Ornamenting with Gold Nanoparticles in Water. *Angewandte Chemie, 118*(1), 110-113.

Kim, D. S., Lee, T., & Geckeler, K. E. (2006b). Hole-Doped Single-Walled Carbon Nanotubes: Ornamenting with Gold Nanoparticles in Water. *Angewandte Chemie International Edition, 45*(1), 104-107.

Kim, S. (2006). CNT sensors for detecting gases with low adsorption energy by ionization. *Sensors, 6*(5), 503-513.

Kind, H., Yan, H., Messer, B., Law, M., & Yang, P. (2002). Nanowire ultraviolet photodetectors and optical switches. *Advanced Materials, 14*(2), 158.

Kohl, D. (2001). Function and applications of gas sensors. *Journal of Physics D: Applied Physics, 34*(19), R125.

Kong, J., Franklin, N. R., Zhou, C., Chapline, M. G., Peng, S., Cho, K., & Dai, H. (2000). Nanotube Molecular Wires as Chemical Sensors. *Science, 287*(5453), 622-625.

Kong, X. Y., Ding, Y., Yang, R., & Wang, Z. L. (2004). Single-crystal nanorings formed by epitaxial self-coiling of polar nanobelts. *Science, 303*(5662), 1348-1351.

Kou, H., Jia, L., & Wang, C. (2012). Electrochemical deposition of flower-like ZnO nanoparticles on a silver-modified carbon nanotube/polyimide membrane to improve its photoelectric activity and photocatalytic performance. *Carbon, 50*(10), 3522-3529.

Kroto, H. W., Heath, J. R., O'Brien, S. C., Curl, R. F., & Smalley, R. E. (1985). C60: Buckminsterfullerene. *Nature, 318*(6042), 162-163.

Kumar, P. S., & Kirthika, K. (2009). Equilibrium and kinetic study of adsorption of nickel from aqueous solution onto bael tree leaf powder. *Journal of Engineering Science and Technology, 4*(4), 351-363.

Kuo, C.-Y., Wu, C.-H., & Wu, J.-Y. (2008). Adsorption of direct dyes from aqueous solutions by carbon nanotubes: Determination of equilibrium, kinetics and thermodynamics parameters. *Journal of Colloid and Interface Science, 327*(2), 308-315.

Kuzuo, R., Terauchi, M., & Tanaka, M. (1992). Electron energy-loss spectra of carbon nanotubes. *Japanese Journal of Applied Physics, 31*(10B), L1484.

Langmuir, I. (1918). The adsorption of gases on plane surfaces of glass, mica and platinum. *Journal of The American Chemical Society, 40*(9), 1361-1403.

Law, J., & Thong, J. (2006). Simple fabrication of a ZnO nanowire photodetector with a fast photoresponse time. *Applied Physics Letters, 88*(13), 133114.

Leubner, S., Katsukis, G., & Guldi, D. M. (2012). Decorating polyelectrolyte wrapped SWNTs with CdTe quantum dots for solar energy conversion. *Faraday Discussions, 155*, 253-265.

Li, J., Lu, Y., Ye, Q., Cinke, M., Han, J., & Meyyappan, M. (2003). Carbon nanotube sensors for gas and organic vapor detection. *Nano Letters, 3*(7), 929-933.

Li, J., & Zhang, Y. (2005). A simple purification for single-walled carbon nanotubes. *Physica E, 28*(3), 309-312.

Li, Y.-H., Wang, S., Cao, A., Zhao, D., Zhang, X., Xu, C., Luan, Z., Ruan, D., Liang, J., & Wu, D. (2001). Adsorption of fluoride from water by amorphous alumina supported on carbon nanotubes. *Chemical Physics Letters, 350*(5), 412-416.

Li, Y.-H., Wang, S., Wei, J., Zhang, X., Xu, C., Luan, Z., Wu, D., & Wei, B. (2002). Lead adsorption on carbon nanotubes. *Chemical Physics Letters, 357*(3), 263-266.

Liu, Y., Zhu, G., Ge, B., Zhou, H., Yuan, A., & Shen, X. (2012). Concave Co 3 O 4 octahedral mesocrystal: polymer-mediated synthesis and sensing properties. *CrystEngComm, 14*(19), 6264-6270.

Lu, C., Chung, Y.-L., & Chang, K.-F. (2005). Adsorption of trihalomethanes from water with carbon nanotubes. *Water Research, 39*(6), 1183-1189.

Machado, F. M., Bergmann, C. P., Fernandes, T. H., Lima, E. C., Royer, B., Calvete, T., & Fagan, S. B. (2011). Adsorption of Reactive Red M-2BE dye from water solutions by multi-walled carbon nanotubes and activated carbon. *Journal of Hazardous Materials, 192*(3), 1122-1131.

Machado, F. M., Bergmann, C. P., Lima, E. C., Royer, B., de Souza, F. E., Jauris, I. M., Calvete, T., & Fagan, S. B. (2012). Adsorption of Reactive Blue 4 dye from water solutions by carbon nanotubes: experiment and theory. *Physical Chemistry Chemical Physics, 14*(31), 11139-11153.

Mall, I. D., Srivastava, V. C., & Agarwal, N. K. (2006). Removal of Orange-G and Methyl Violet dyes by adsorption onto bagasse fly ash—kinetic study and equilibrium isotherm analyses. *Dyes and Pigments, 69*(3), 210-223.

Marinković, S. N. (2008). Carbon nanotubes. *Journal of the Serbian Chemical Society, 73*(8-9), 891-913.

Maschio, G., Koufopanos, C., & Lucchesi, A. (1992). Pyrolysis, a promising route for biomass utilization. *Bioresource Technology, 42*(3), 219-231.

Mickelson, E., Huffman, C., Rinzler, A., Smalley, R., Hauge, R., & Margrave, J. (1998). Fluorination of single-wall carbon nanotubes. *Chemical Physics Letters, 296*(1), 188-194.

Mirzaei, A., Janghorban, K., Hashemi, B., Bonavita, A., Bonyani, M., Leonardi, G. S., & Neri, G. (2015). Synthesis, Characterization and Gas Sensing Properties of Ag@α-Fe2O3 Core–Shell Nanocomposites. *Nanomaterials, 5*(2).

Mishra, A. K., Arockiadoss, T., & Ramaprabhu, S. (2010). Study of removal of azo dye by functionalized multi walled carbon nanotubes. *Chemical Engineering Journal, 162*(3), 1026-1034.

Modi, A., Koratkar, N., Lass, E., Wei, B., & Ajayan, P. M. (2003). Miniaturized gas ionization sensors using carbon nanotubes. *Nature, 424*(6945), 171.

Moghaddam, H. K., & Pakizeh, M. (2015). Experimental study on mercury ions removal from aqueous solution by MnO_2/CNTs nanocomposite adsorbent. *Journal of Industrial and Engineering Chemistry, 21*, 221-229.

Monthioux, M., & Kuznetsov, V. L. (2006). Who should be given the credit for the discovery of carbon nanotubes? *Carbon, 44*(9), 1621-1623.

Morkoç, H., & Özgür, Ü. (2009). General Properties of ZnO *Zinc Oxide* (pp. 1-76): Wiley-VCH Verlag GmbH & Co. KGaA.

Murakami, Y., Einarsson, E., Edamura, T., & Maruyama, S. (2005). Polarization dependent optical absorption properties of single-walled carbon nanotubes and methodology for the evaluation of their morphology. *Carbon, 43*(13), 2664-2676.

Osman, M. A., & Srivastava, D. (2001). Temperature dependence of the thermal conductivity of single-wall carbon nanotubes. *Nanotechnology, 12*(1), 21.

Özcan, A., & Özcan, A. S. (2005). Adsorption of Acid Red 57 from aqueous solutions onto surfactant-modified sepiolite. *Journal of Hazardous Materials, 125*(1), 252-259.

Özgür, Ü., Alivov, Y. I., Liu, C., Teke, A., Reshchikov, M., Doğan, S., Avrutin, V., Cho, S.-J., & Morkoc, H. (2005). A comprehensive review of ZnO materials and devices. *Journal of Applied Physics, 98*(4), 11.

Pan, Z. W., Mahurin, S. M., Dai, S., & Lowndes, D. H. (2005). Nanowire array gratings with ZnO combs. *Nano Letters, 5*(4), 723-727.

Panday, K., Prasad, G., & Singh, V. (1986). Mixed adsorbents for Cu (II) removal from aqueous solutions. *Environmental Technology, 7*(1-12), 547-554.

Patiha, Heraldy, E., Hidayat, Y., & Firdaus, M. (2016). The langmuir isotherm adsorption equation: The monolayer approach. *IOP Conference Series: Materials Science and Engineering, 107*(1), 012067.

Peng, H., Reverdy, P., Khabashesku, V. N., & Margrave, J. L. (2003). Sidewall functionalization of single-walled carbon nanotubes with organic peroxides. *Chemical Communications,* (3), 362-363.

Peng, L.-M., Zhang, Z., & Wang, S. (2014). Carbon nanotube electronics: recent advances. *Materials Today, 17*(9), 433-442.

Peng, X., Luan, Z., Ding, J., Di, Z., Li, Y., & Tian, B. (2005). Ceria nanoparticles supported on carbon nanotubes for the removal of arsenate from water. *Materials Letters, 59*(4), 399-403.

Pop, E., Mann, D., Wang, Q., Goodson, K., & Dai, H. (2006). Thermal conductance of an individual single-wall carbon nanotube above room temperature. *Nano Letters, 6*(1), 96-100.

Popov, M., Kyotani, M., Nemanich, R., & Koga, Y. (2002). Superhard phase composed of single-wall carbon nanotubes. *Physical Review B, 65*(3), 033408.

Prajapati, C., & Sahay, P. (2011). Alcohol-sensing characteristics of spray deposited ZnO nano-particle thin films. *Sensors and Actuators B: Chemical, 160*(1), 1043-1049.

Qi, P., Vermesh, O., Grecu, M., Javey, A., Wang, Q., Dai, H., Peng, S., & Cho, K. (2003). Toward large arrays of multiplex functionalized carbon nanotube sensors for highly sensitive and selective molecular detection. *Nano Letters, 3*(3), 347-351.

Qi, Q., Zhang, T., Liu, L., Zheng, X., & Lu, G. (2009). Improved NH_3, C_2H_5OH, and CH_3COCH_3 sensing properties of SnO_2 nanofibers by adding block copolymer P123. *Sensors and Actuators B: Chemical, 141*(1), 174-178.

Rajaputra, S., Mangu, R., Clore, P., Qian, D., Andrews, R., & Singh, V. P. (2008). Multi-walled carbon nanotube arrays for gas sensing applications. *Nanotechnology, 19*(34), 345502.

Rao, A., Jorio, A., Pimenta, M., Dantas, M., Saito, R., Dresselhaus, G., & Dresselhaus, M. (2000). Polarized Raman study of aligned multiwalled carbon nanotubes. *Physical Review Letters, 84*(8), 1820.

Rengaraj, S., Kim, Y., Joo, C. K., & Yi, J. (2004). Removal of copper from aqueous solution by aminated and protonated mesoporous aluminas: kinetics and equilibrium. *Journal of Colloid and Interface Science, 273*(1), 14-21.

Rochefort, A., Avouris, P., Lesage, F., & Salahub, D. R. (1999). Electrical and mechanical properties of distorted carbon nanotubes. *Physical Review B, 60*(19), 13824.

Rodriguez, A., Ovejero, G., Sotelo, J., Mestanza, M., & Garcia, J. (2010). Adsorption of dyes on carbon nanomaterials from aqueous solutions. *Journal of Environmental Science and Health Part A, 45*(12), 1642-1653.

Rosa, G., Reynel-Avila, H. E., Bonilla-Petriciolet, A., Cano-Rodriguez, I., Velasco-Santos, C., & Martínez-Hernández, A. (2008). Recycling poultry feathers for Pb removal from wastewater: kinetic and equilibrium studies. *International Journal of Chemical and Biomolecular Engineering, 1*(4), 185-193.

Ryabenko, A., Dorofeeva, T., & Zvereva, G. (2004). UV–VIS–NIR spectroscopy study of sensitivity of single-wall carbon nanotubes to chemical processing and Van-der-Waals SWNT/SWNT interaction. Verification of the SWNT content measurements by absorption spectroscopy. *Carbon, 42*(8), 1523-1535.

Saito, R., Dresselhaus, G., & Dresselhaus, M. S. (1998). *Physical properties of carbon nanotubes*: World scientific.

Saito, R., Jorio, A., Souza Filho, A. G., Dresselhaus, G., Dresselhaus, M. S., & Pimenta, M. A. (2002). Probing phonon dispersion relations of graphite by double resonance Raman scattering. *Physical Review Letters, 88*(2), 027401.

Sayago, I., Santos, H., Horrillo, M., Aleixandre, M., Fernandez, M., Terrado, E., Tacchini, I., Aroz, R., Maser, W., & Benito, A. (2008). Carbon nanotube networks as gas sensors for NO 2 detection. *Talanta, 77*(2), 758-764.

Selwyn, J. E., & Steinfeld, J. I. (1972). Aggregation of equilibriums of xanthene dyes. *The Journal of Physical Chemistry, 76*(5), 762-774.

Sen, D., Lakhotiya, H., Das, A., Bahadur, J., Mazumder, S., & Basak, C. (2015). Organic–inorganic composite micro-granules by evaporation induced assembly: role of trapped water in structural evolution. *Royal Society of Chemistry Advances, 5*(29), 22884-22891.

Shamsudin, M., Suriani, A., Abdullah, S., Yahya, S., & Rusop, M. (2012). Impact of thermal annealing under nitrogen ambient on structural, micro-Raman, and thermogravimetric analyses of camphoric-CNT. *Journal of Spectroscopy, 2013*.

Shamsudin, M. S., Suriani, A. B., Abdullah, S., Yahya, S. Y. S., & Rusop, M. (2013). Impact of Thermal Annealing under Nitrogen Ambient on Structural, Micro-Raman, and Thermogravimetric Analyses of Camphoric-CNT. *Journal of Spectroscopy, 2013*, 1-6.

Shao, D., Hu, J., Wang, X., & Nagatsu, M. (2011). Plasma induced grafting multiwall carbon nanotubes with chitosan for 4, 4′-dichlorobiphenyl removal from aqueous solution. *Chemical Engineering Journal, 170*(2), 498-504.

Shi, R., Yang, P., Dong, X., Ma, Q., & Zhang, A. (2013). Growth of flower-like ZnO on ZnO nanorod arrays created on zinc substrate through low-temperature hydrothermal synthesis. *Applied Surface Science, 264*, 162-170.

Shigeta, M., Komatsu, M., & Nakashima, N. (2006). Individual solubilization of single-walled carbon nanotubes using totally aromatic polyimide. *Chemical Physics Letters, 418*(1), 115-118.

Shih, Y.-h., & Li, M.-s. (2008). Adsorption of selected volatile organic vapors on multiwall carbon nanotubes. *Journal of Hazardous Materials, 154*(1), 21-28.

Shirmardi, M., Mesdaghinia, A., Mahvi, A. H., Nasseri, S., & Nabizadeh, R. (2012). Kinetics and equilibrium studies on adsorption of acid red 18 (Azo-Dye) using multiwall carbon nanotubes (MWCNTs) from aqueous solution. *Journal of Chemistry, 9*(4), 2371-2383.

Singh, R. C., Kohli, N., Singh, M. P., & Singh, O. (2010). Ethanol and LPG sensing characteristics of SnO2 activated Cr2O3 thick film sensor. *Bulletin of Materials Science, 33*(5), 575-579.

Subannajui, K., Güder, F., Danhof, J., Menzel, A., Yang, Y., Kirste, L., Wang, C., Cimalla, V., Schwarz, U., & Zacharias, M. (2012). An advanced fabrication method of highly ordered ZnO nanowire arrays on silicon substrates by atomic layer deposition. *Nanotechnology, 23*(23), 235607.

Suehiro, J., Zhou, G., & Hara, M. (2003). Fabrication of a carbon nanotube-based gas sensor using dielectrophoresis and its application for ammonia detection by impedance spectroscopy. *Journal of Physics D: Applied Physics, 36*(21), L109.

Sui, M., Zhang, L., Sheng, L., Huang, S., & She, L. (2013). Synthesis of ZnO coated multi-walled carbon nanotubes and their antibacterial activities. *Science of the Total Environment, 452*, 148-154.

Sun, C.-J., Sun, L.-Z., & Sun, X.-X. (2013). Graphical evaluation of the favorability of adsorption processes by using conditional langmuir constant. *Industrial & Engineering Chemistry Research, 52*(39), 14251-14260.

Sun, Y., Wang, L., Yu, X., & Chen, K. (2012). Facile synthesis of flower-like 3D ZnO superstructures via solution route. *CrystEngComm, 14*(9), 3199-3204.

Sun, Z., Zhang, X., Na, N., Liu, Z., Han, B., & An, G. (2006). Synthesis of ZrO2−Carbon Nanotube Composites and Their Application as Chemiluminescent Sensor Material for Ethanol. *The Journal of Physical Chemistry B, 110*(27), 13410-13414.

Švrček, V., Pham-Huu, C., Ledoux, M.-J., Le Normand, F., Ersen, O., & Joulie, S. (2006). Filling of single silicon nanocrystals within multiwalled carbon nanotubes. *Applied Physics Letters, 88*(3), 033112.

Tasaltin, C., & Basarir, F. (2014). Preparation of flexible VOC sensor based on carbon nanotubes and gold nanoparticles. *Sensors and Actuators B: Chemical, 194*, 173-179.

Temkin, M., & Pyzhev, V. (1940). Recent modifications to Langmuir isotherms.

Terranova, M., Lucci, M., Orlanducci, S., Tamburri, E., Sessa, V., Reale, A., & Di Carlo, A. (2007). Carbon nanotubes for gas detection: materials preparation and device assembly. *Journal of Physics: Condensed Matter, 19*(22), 225004.

Terrones, M., Jorio, A., Endo, M., Rao, A., Kim, Y., Hayashi, T., Terrones, H., Charlier, J.-C., Dresselhaus, G., & Dresselhaus, M. (2004). New direction in nanotube science. *Materials today, 7*(10), 30-45.

Thostenson, E. T., Li, C., & Chou, T.-W. (2005). Nanocomposites in context. *Composites Science and Technology, 65*(3), 491-516.

Trinh, T. T., Tu, N. H., Le, H. H., Ryu, K. Y., Le, K. B., Pillai, K., & Yi, J. (2011). Improving the ethanol sensing of ZnO nano-particle thin films—the correlation between the grain size and the sensing mechanism. *Sensors and Actuators B: Chemical, 152*(1), 73-81.

Tsang, S., Chen, Y., Harris, P., & Green, M. (1994). A simple chemical method of opening and filling carbon nanotubes. *Nature, 372*(6502), 159-162.

Ueda, T., Bhuiyan, M., Norimatsu, H., Katsuki, S., Ikegami, T., & Mitsugi, F. (2008). Development of carbon nanotube-based gas sensors for NOx gas detection working at low temperature. *Physica E: Low-dimensional Systems and Nanostructures, 40*(7), 2272-2277.

Vaisman, L., Wagner, H. D., & Marom, G. (2006). The role of surfactants in dispersion of carbon nanotubes. *Advances in colloid and interface science, 128*, 37-46.

Valentini, L., Armentano, I., Lozzi, L., Santucci, S., & Kenny, J. (2004). Interaction of methane with carbon nanotube thin films: role of defects and oxygen adsorption. *Materials Science and Engineering: C, 24*(4), 527-533.

Wang, F., Cao, L., Pan, A., Liu, R., Wang, X., Zhu, X., Wang, S., & Zou, B. (2007). Synthesis of tower-like ZnO structures and visible photoluminescence origins of varied-shaped ZnO nanostructures. *The Journal of Physical Chemistry C, 111*(21), 7655-7660.

Wang, H., Zhou, W., Ho, D. L., Winey, K. I., Fischer, J. E., Glinka, C. J., & Hobbie, E. K. (2004a). Dispersing single-walled carbon nanotubes with surfactants: a small angle neutron scattering study. *Nano Letters, 4*(9), 1789-1793.

Wang, S., Ng, C. W., Wang, W., Li, Q., & Hao, Z. (2012). Synergistic and competitive adsorption of organic dyes on multiwalled carbon nanotubes. *Chemical Engineering Journal, 197*, 34-40.

Wang, S., Zhang, Q., Yang, D., Sellin, P., & Zhong, G. (2004b). Multi-walled carbon nanotube-based gas sensors for NH_3 detection. *Diamond and Related Materials, 13*(4), 1327-1332.

Wang, X., Xia, B., Zhu, X., Chen, J., Qiu, S., & Li, J. (2008). Controlled modification of multiwalled carbon nanotubes with Zno nanostructures. *Journal of Solid State Chemistry, 181*(4), 822-827.

Wang, Y., & Yeow, J. T. (2009). A review of carbon nanotubes-based gas sensors. *Journal of Sensors, 2009*.

Wang, Z. L., Kong, X. Y., Ding, Y., Gao, P., Hughes, W. L., Yang, R., & Zhang, Y. (2004c). Semiconducting and piezoelectric oxide nanostructures induced by polar surfaces. *Advanced Functional Materials, 14*(10), 943-956.

Wayu, M. B., Spidle, R. T., Devkota, T., Deb, A. K., Delong, R. K., Ghosh, K. C., Wanekaya, A. K., & Chusuei, C. C. (2013). Morphology of hydrothermally synthesized ZnO nanoparticles tethered to carbon nanotubes affects electrocatalytic activity for H_2O_2 detection. *Electrochimica Acta, 97*, 99-104.

Weber, W. J., & Morris, J. C. (1963). Kinetics of adsorption on carbon from solution. *Journal of the Sanitary Engineering Division, 89*(2), 31-60.

Whitsitt, E. A., & Barron, A. R. (2003). Silica coated single walled carbon nanotubes. *Nano Letters, 3*(6), 775-778.

Woods, L., Bădescu, Ş., & Reinecke, T. (2007). Adsorption of simple benzene derivatives on carbon nanotubes. *Physical Review B, 75*(15), 155415.

Wu, C.-H. (2007). Adsorption of reactive dye onto carbon nanotubes: equilibrium, kinetics and thermodynamics. *Journal of Hazardous Materials, 144*(1), 93-100.

Wu, C., Qiao, X., Chen, J., Wang, H., Tan, F., & Li, S. (2006). A novel chemical route to prepare ZnO nanoparticles. *Materials Letters, 60*(15), 1828-1832.

Wu, F.-C., Tseng, R.-L., & Juang, R.-S. (2000). Comparative adsorption of metal and dye on flake-and bead-types of chitosans prepared from fishery wastes. *Journal of Hazardous Materials, 73*(1), 63-75.

Wu, J., Tao, K., Miao, J., & Norford, L. K. (2015). Improved selectivity and sensitivity of gas sensing using a 3D reduced graphene oxide hydrogel with an integrated microheater. *ACS Applied Materials & Interfaces, 7*(49), 27502-27510.

Wu, P., Sun, J., Huang, Y., Gu, G., & Tong, D. (2012). Solution plasma synthesized nickel oxide nanoflowers: an effective NO_2 sensor. *Materials Letters, 82*, 191-194.

Xing, G., Fang, X., Zhang, Z., Wang, D., Huang, X., Guo, J., Liao, L., Zheng, Z., Xu, H., & Yu, T. (2010). Ultrathin single-crystal ZnO nanobelts: Ag-catalyzed growth and field emission property. *Nanotechnology, 21*(25), 255701.

Yakobson, B. (1998). Mechanical relaxation and "intramolecular plasticity" in carbon nanotubes. *Applied Physics Letters, 72*(8), 918-920.

Yan, H., Gong, A., He, H., Zhou, J., Wei, Y., & Lv, L. (2006). Adsorption of microcystins by carbon nanotubes. *Chemosphere, 62*(1), 142-148.

Yan, X.-b., Han, Z.-j., Yang, Y., & Tay, B.-k. (2007). Fabrication of carbon nanotube−polyaniline composites via electrostatic adsorption in aqueous colloids. *The Journal of Physical Chemistry C, 111*(11), 4125-4131.

Yáñez-Sedeño, P., Pingarrón, J. M., Riu, J., & Rius, F. X. (2010). Electrochemical sensing based on carbon nanotubes. *Trends in Analytical Chemistry, 29*(9), 939-953.

Yang, C., Su, X., Xiao, F., Jian, J., & Wang, J. (2011). Gas sensing properties of CuO nanorods synthesized by a microwave-assisted hydrothermal method. *Sensors and Actuators B: Chemical, 158*(1), 299-303.

Yang, D. J., Zhang, Q., Chen, G., Yoon, S. F., Ahn, J., Wang, S. G., Zhou, Q., Wang, Q., & Li, J. Q. (2002). Thermal conductivity of multiwalled carbon nanotubes. *Physical Review B, 66*(16).

Yang, N., Chen, X., Ren, T., Zhang, P., & Yang, D. (2015). Carbon nanotube based biosensors. *Sensors and Actuators B: Chemical, 207*, 690-715.

Yang, Z.-P., Ci, L., Bur, J. A., Lin, S.-Y., & Ajayan, P. M. (2008). Experimental observation of an extremely dark material made by a low-density nanotube array. *Nano Letters, 8*(2), 446-451.

Yang, Z., Huang, Y., Chen, G., Guo, Z., Cheng, S., & Huang, S. (2009). Ethanol gas sensor based on Al-doped ZnO nanomaterial with many gas diffusing channels. *Sensors and Actuators B: Chemical, 140*(2), 549-556.

Yao, Y., Xu, F., Chen, M., Xu, Z., & Zhu, Z. (2010). Adsorption behavior of methylene blue on carbon nanotubes. *Bioresource Technology, 101*(9), 3040-3046.

Young, S., & Lin, Z. (2016). Ethanol gas sensors based on multi-wall carbon nanotubes on oxidized Si substrate. *Microsystem Technologies*, 1-4.

Yu, J.-G., Zhao, X.-H., Yang, H., Chen, X.-H., Yang, Q., Yu, L.-Y., Jiang, J.-H., & Chen, X.-Q. (2014). Aqueous adsorption and removal of organic contaminants by carbon nanotubes. *Science of The Total Environment, 482*, 241-251.

Yu, J., Grossiord, N., Koning, C. E., & Loos, J. (2007). Controlling the dispersion of multi-wall carbon nanotubes in aqueous surfactant solution. *Carbon, 45*(3), 618-623.

Zare, K., Gupta, V. K., Moradi, O., Makhlouf, A. S. H., Sillanpää, M., Nadagouda, M. N., Sadegh, H., Shahryari-ghoshekandi, R., Pal, A., & Wang, Z.-j. (2015). A comparative study on the basis of adsorption capacity between CNTs and activated carbon as adsorbents for removal of noxious synthetic dyes: a review. *Journal of Nanostructure in Chemistry, 5*(2), 227-236.

Zhang, X., Liu, T., Sreekumar, T., Kumar, S., Moore, V. C., Hauge, R. H., & Smalley, R. E. (2003). Poly (vinyl alcohol)/SWNT composite film. *Nano Letters, 3*(9), 1285-1288.

Zhang, Y., Sun, X., Pan, L., Li, H., Sun, Z., Sun, C., & Tay, B. K. (2009). Carbon nanotube–zinc oxide electrode and gel polymer electrolyte for electrochemical supercapacitors. *Journal of Alloys and Compounds, 480*(2), L17-L19.

Zhao, J., Buldum, A., Han, J., & Lu, J. P. (2002). Gas molecule adsorption in carbon nanotubes and nanotube bundles. *Nanotechnology, 13*(2), 195.

Zhou, Y., Jiang, Y., Xie, G., Du, X., & Tai, H. (2014). Gas sensors based on multiple-walled carbon nanotubes-polyethylene oxide films for toluene vapor detection. *Sensors and Actuators B: Chemical, 191*, 24-30.

Zohre, S., Ataallah, S. G., & Mehdi, A. (2010). Experimental study of methylene blue adsorption from aqueous solutions onto carbon nano tubes. *International Journal of Water Resources and Environmental Engineering, 2*(2), 016-028.

LIST OF PUBLICATIONS AND PAPERS PRESENTED

Ahmad, F., Harun, S., Nor, R., **Zulkepely, N.**, Ahmad, H., & Shum, P. (2013). A passively mode-locked erbium-doped fiber laser based on a single-wall carbon nanotube polymer. *Chinese Physics Letters, 30*(5), 054210.

Tan, S., Harun, S., Ahmad, F., Nor, R., **Zulkepely, N.**, & Ahmad, H. (2013). A Q-switched multi-wavelength Brillouin erbium fiber laser with a single-walled carbon nanotube saturable absorber. *Laser Physics, 23*(5), 055101.

Haris, H., Anyi, C., Ali, N., Arof, H., Ahmad, F., Nor, R., **Zulkepely, N.**, & Harun, S. (2014). Passively Q-switched erbium-doped fiber laser at L-band region by employing multi-walled carbon nanotubes as saturable absorber. *Journal Optoelectronics and Advanced Materials-Rapid Communications*, *8*(11-12), 1025-1028.

Ahmad, F., Haris, H., Nor, R., **Zulkepely, N.**, Ahmad, H., & Harun, S. (2014). Passively Q-switched EDFL using a multi-walled carbon nanotube polymer composite based on a saturable absorber. *Chinese Physics Letters, 31*(3), 034204.

Ahmad, F., Harun, S., Nor, R., **Zulkepely, N.**, Muhammad, F., Arof, H., & Ahmad, H. (2014). Mode-locked soliton erbium-doped fiber laser using a single-walled carbon nanotubes embedded in polyethylene oxide thin film saturable absorber. *Journal of Modern Optics, 61*(6), 541-545.

Haris, H., Anyi, C., Muhammad, A., Ahmad, F., Nor, R., **Zulkepely, N.**, Ali, N., Harun, S., & Arof, H. (2015). Performance of passively Q-switched ring erbium-doped fiber laser using a multiwalled carbon nanotubes polyethylene oxide (PEO) polymer composite-based saturable absorber. *Microwave and Optical Technology Letters, 57*(8), 1897-1901.

Nurul Rozullyah Zulkepely and Roslan Md Nor, 'MWCNTs Deposited on Printing Paper as Toluene Sensor at Room Temperature', Oral presentation at the 2nd Advanced Materials Conference (AMC 2014), Langkawi, Malaysia.

Nurul Rozullyah Zulkepely and Roslan Md Nor, 'MWCNTs Deposited on Printing Paper as Ethanol Sensor at Room Temperature', Oral presentation at the National Physics Conference (PERFIK2016), Kuala Lumpur, Malaysia.